2005

A Study on the Nature of Anomalous Current Conduction in Gallium Nitride

Joshua K. Spradlin
Virginia Commonwealth University

A Study of Anomalous Current Conduction in Gallium Nitride Devices

A thesis submitted in partial fulfillment of the requirements for the degree of Master's of Electrical Engineering at Virginia Commonwealth University.

Submitted by:
Joshua K. Spradlin
B.S. Electrical Engineering & Physics, Virginia Commonwealth University, 2001

Director:
Hadis Morkoç
Founders Professor of Electrical Engineering and Physics
Electrical Engineering
Virginia Commonwealth University
Richmond, Virginia
May 2005

Acknowledgements

I would like to thank all of my teachers for their efforts in my education. I commend the Virginia Commonwealth University Engineering School, and courageous faculty, for demonstrating a successful, engaging, and empowering learning environment. I am especially grateful towards Dr. Baski and Dr. Morkoç for providing me with an opportunity to pursue my graduate studies, for their encouragement, and their support. With your efforts as mentors, you have enabled me with the greatest gift any teacher can give. The numerous individuals that contributed to my studies at Virginia Commonwealth University, fellow researchers, faculty, support staff, etc. My work has become quite consuming over the last few years and I thank all of my friends and family for their understanding, love, and patience. The guidance and love of my parents warrants gratitude beyond mention. I must express my overwhelming gratitude to Setagon Inc., specifically: Whye-Kei Lye, Kareen Looi, and Dr. Micheal Reed, your generosity and guidance are unquestionably appreciated beyond elaborated measures. To my loving special someone, Laura, I will eternally appreciate giving me your support, patience, and love through my trials. Specifically, this work is dedicated to GG, thank you for always being there.

Table of Contents

List of Tables

List of Figures

List of Equations

Abstract

A STUDY ON THE NATURE OF ANOMALOUS CURRENT CONDUCTION IN GALLIUM NITRIDE

Joshua Spradlin, B.S. Electrical Engineering and Physics, Virginia Commonwealth University 2001

A thesis submitted in partial fulfillment of the requirements for the degree of Master's of Electrical Engineering at Virginia Commonwealth University.

Virginia Commonwealth University 2005

Hadis Morkoç, Founders Professor of Electrical Engineering and Physics, Electrical Engineering

Current leakage in GaN thin films limits reliable device fabrication. A variety of Ga and N rich MBE GaN thin films grown by Rf, NH_3, and Rf + NH_3, are examined with electrical measurements on Ni/Au Schottky diodes and CAFM. Current-voltage (IV) mechanisms will identify conduction mechanisms on diodes, and CAFM measurements

will investigate the microstructure of conduction in GaN thin films. With CAFM, enhanced conduction has been shown to decorate some extended defects and surface features, while CAFM spectroscopy on a MODFET structure indicates a correlation between extended defects and field conduction behavior at room temperature. A remedy for poor conduction characteristics is presented in molten KOH etching, as evidenced by CAFM measurements, Schottky diodes, and MODFET's. The aim of this study is to identify anomalous conduction mechanisms, the likely cause of anomalous conduction, and a method for improving the conduction characteristics.

Keywords: III-Nitride, III-V, Gallium Nitride, GaN, Electrical Properties, Conduction, Conductivity, Mobility, Hall Measurements, Resistivity, Schottky Diode, Modulation Doped Field Effect Transistor (MODFET), Conductive Atomic Force Microscopy (AFM), Defects, Molten Potassium Hydroxide (KOH) etching, Silvaco, Atlas, and Illumination.

1 Introduction and Background

Providing devices with extended operating conditions, and advances in performance in magnetic, optical, and electrical properties, wide band gap semiconductors have been gaining popularity in recent years. Light emitting diodes (LED's), lasing diodes (LD's), ultra violet (UV) optical detectors / switches, high frequency / power field effect transistors, and other novel devices have already been demonstrated using III-Nitrides.[1] Gallium Nitride is currently one of the most widely studied of the III-Nitrides, gaining initial interest from commercial demonstration of the first blue light emitting diode (LED). A major technical barrier that hinders III-Nitride compounds is large concentrations of native defects that significantly distort the optical and electronic properties, rendering devices mostly inoperable. The III-Nitride semiconductors are difficult to grow, and fabricate devices on, due to chemical inertness and lack of ideal substrates.[1]

When native substrates are not available, the substrate can be several materials for any given semiconductor but it is a large factor in major crystal defects. Growth quality is best achieved when the substrate and deposited film have closely matched thermal

expansion and lattice constants. Poor substrates, growth conditions, or device fabrication can compromise the electrical characteristics of any device. While investigating novel characteristics of the materials, commercial demand has fueled an exhaustive search into the III-Nitride and other wide band gap semiconductors to find better methods for producing materials that meet demands in power, optical, and Rf electronics. A hurdle to bipolar devices has been overcome in successful fabrication of p-type Gallium Nitride. Another class of exotic devices includes heterojunction bipolar devices, which utilize p-type Silicon Carbide as substrates with an n-type GaN overgrowth. Complex device structures incorporating heterojunctions demand demonstration of excellent interface control.

Some labs have overcome the difficulties associated with high background n-type carrier concentrations from native defects in III-N growth. While literature to date lacks a sure recipe for high quality n-type and p-type GaN, the general boundaries for high quality Ga-polar n-type GaN is achieved in ammonia MBE reactors near Ga-rich conditions with a substrate temperature just below the Ga desorption point (~900 °C). In nitrogen plasma MBE grown GaN, the film quality is a strong function of balancing the nitrogen plasma flux and substrate temperature. Ultimately avoiding the incorporation of point defects, while minimizing the density of macroscopic structural defects, will ensure good device quality material. Good Schottky device reports for GaN grown by MBE[2] and MOCVD[3] were published as early as 1998. A rather recent publication presents Au Schottky contacts on n-type GaN grown by a new deposition technique coined reactive hot wall vapor deposition.[4]

Another front of research has concentrated on understanding the properties of confinement, i.e. surface area to bulk volume ratio, in small-scale structures coined nanofeatures (exhibiting some structural aspect less than a micron in width, generally less than 100's of nm). The best representative sample of this class of solid materials would be a porous matrix of a given semiconductor, or metal. In a porous material the surface area increases as the bulk volume connecting the material decreases in a cross sectional diameter. As seen with colloids and clusters, novel properties emerge, most notably optical and electrical, as the density of nanofeatures is increased and / or the confined dimension of the nanofeatures is changed. A large emphasis has been placed on decreasing the size of devices to achieve increased performance and device density. Single electron devices and molecular transistors are alternative computing technologies, however these devices will unlikely meet the power capabilities and switching abilities of bulk solid-state devices. The transport of charged carriers in thin films with high defect densities mediates the devices that will be able to be fabricated.

1.1 Semiconductor Materials

Semiconductors are a class of materials that to a first extent fall between metals insulators, though as understanding of material properties, production, and fabrication increases materials once thought to be insulators are becoming candidates for semiconductor electronic devices. Metals have an excess of free charge, semiconductors have a slight deficiency in free carriers, and insulators have no free carriers. All materials have an electronic structure that is determined by the chemical constituents and

bonding characteristics, locally and globally. In a crystalline semiconductor the energetic separation of occupied valence states and the conduction states of excited electrons, endows novel conduction properties that are utilized in electronic device design.

In order to describe complex crystal structures like the wurzitic and zincblende configurations a convention had to be established for the crystal orientation. This problem was solved with the assignment of Brillouin zones, which are specific for a given crystal structure.[5] The Brillouin zone for a wurzite crystal is the right hexagonal prism, provided as Figure 1 - Brillouin Zone Figure courtesy of ref. 1.

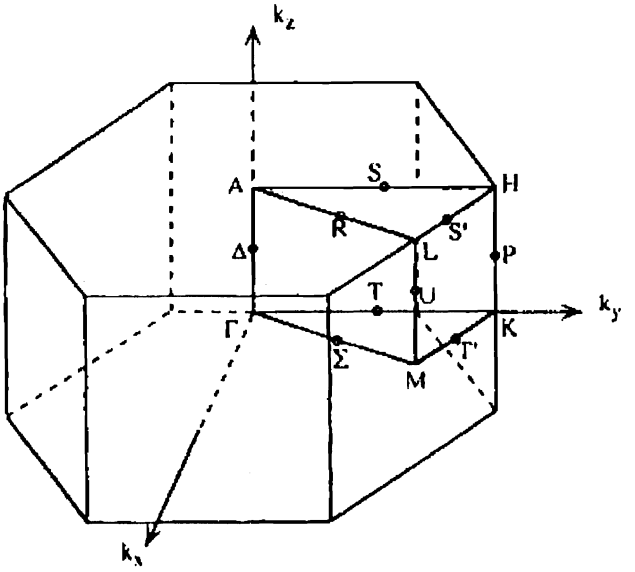

Figure 1 - Brillouin Zone Figure

Figure from ref. 1 without permission.

A wurzitic crystal is commonly viewed from the Γ point, which corresponds to the [0001] direction, or z-axis of the unit cell. With a defined crystal orientation, a diagram can be constructed that defines the necessary energy a carrier needs to transition from the valance bands to the conduction bands as a function of 3-D rotation about the unit cell. The energy band diagram represents the three-dimensional energy structure of the crystal in terms of momentum states and corresponding energies, more information can be found in "Survey of Semiconductor Physics"[6], or preferably in ref. 1. In the simplest model, the E-k diagram represents the conduction and valance bands as a parabola at the gamma point.[7] Gallium Nitride's conduction bands can be approximated by parabola due to the low non-parabolicity of the gamma transition point.[5] The curvature of energy bands are proportional to carriers' effective mass occupying that band. The number of bands in the E-k diagram depends on the crystal type, every band shown represents both spin states, see B.R. Nag for more details.

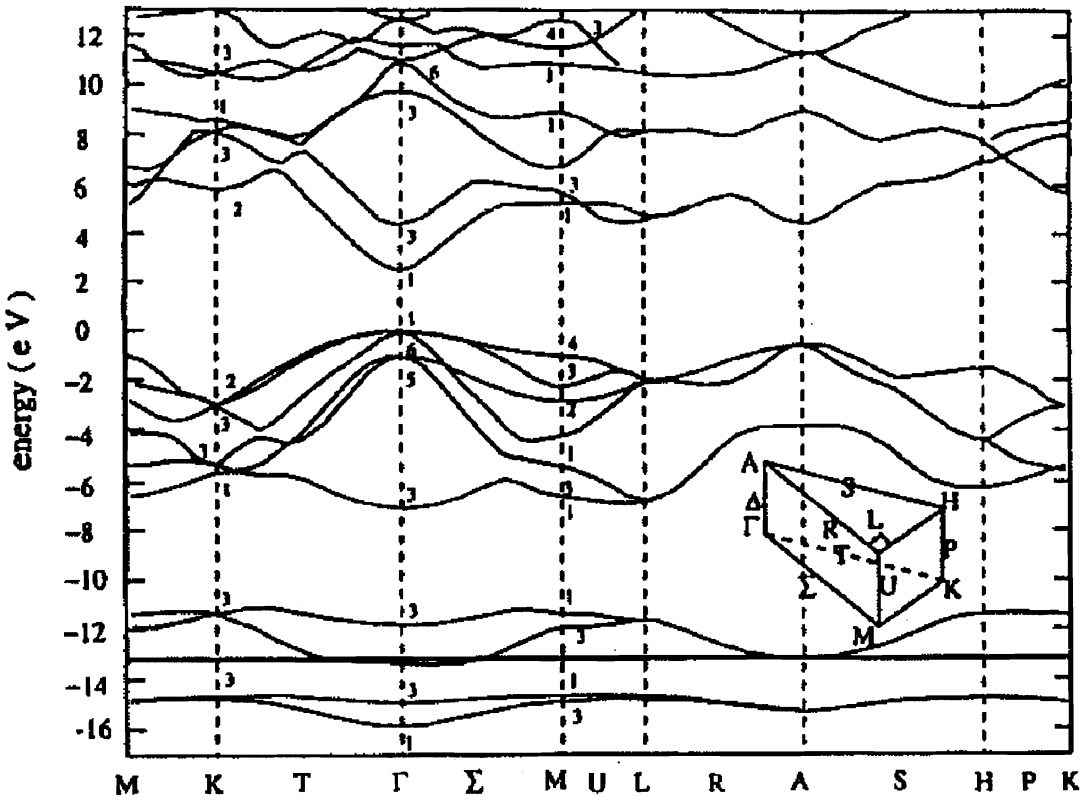

Figure 2 - E-k Diagram

Figure from ref. 1 without permission.

The absence of an electron from the valence shell of an atom is defined as a hole in that atom's local electronic structure. In the presence of an applied bias, holes will move in the opposite direction of electrons and contribute to the observed forward current flow. Holes represent a larger absence of energy as they occupy lower valence bands, while electrons are at lower energies in lower conduction bands.

Intrinsic semiconductor materials are devoid of impurities and highly resistive, therefore doping is necessary to fabricate electronic devices. A dopant can be any element that will donate (donor) or accept (acceptor) an electron when substituted into the semiconductor lattice for one of the constituent elements. As long as phase precipitations are negligible, selecting an element with a difference in valance charge can yield a suitable dopant. Native defects can also act as unintentional dopants by periodically perturbing the crystalline structure. Dopants are usually added in concentrations less than 10^{17} cm^{-3}. Ultimately the device structure dictates the doping requirements. Utilizing dopants and extremely precise growth techniques for thin films, a wide range of substrates for devices can be produced, but contacts are still needed.

For an electron to move inside a pure ideal semiconductor they must interact with free energy and respond to applied biases while residing in the conduction band of the semiconductor. At zero degrees Kelvin there are no electrons in the conduction band, regardless of doping, since the conduction bands are some energy greater than the equilibrium energy of the valance bands, or the bonding energies of the donor / defects states. As the temperature increases above zero degrees Kelvin thermal excitation of carriers follows a Gausian distribution defined by the Fermi function. The occupancy of states in the conduction band by electrons, or conversely the absence of electrons (holes) in the valence band, is given by the Fermi function,

Equation 1 - Conduction Band Fermi Function

$$F(E) = \frac{1}{1 + \exp\left(\frac{E - E_F}{kT}\right)}$$

In the above expression, F(E) is the Fermi occupancy as a function of energy, E is a respective energy, E_F is the Fermi Energy, k is the Boltzmann constant, and T is the temperature. The Fermi energy describes the availability of carriers based on the thermal equilibrium potential of the material's energy structure. The free electron concentration can be determined by integrating the product of the Fermi function and the density of states for the conduction band, see any introductory text on semiconductors. Performing the above yields an expression for the free electron concentration, n, as follows:[8]

Equation 2 - Free Electron Concentration

$$n = N_C \exp\left(\frac{E - E_C}{kT}\right)$$

The parameter N_C is the conduction band density of states, for more information see section 2.2.3 Capacitance-Voltage Measurements. When there is a significant density of surface states, or point defects in the near surface region, the Fermi level is no longer solely a function of the donor concentration, temperature, and bandgap, but also of fixed and mobile charge in the semiconductor film, and at the interfaces.

An electron's motion is intimately coupled to the free energy in the lattice. The electrons are described as plane wave Bloch functions, which are defined by the constraints of the periodic interactions with the semiconductor lattice. In any material the bonds and free electrons will move with random thermal motion, however, if the material

has an applied electric field then, as in free space, the electrons are forced to move through a semiconductor's crystal lattice in the direction of an applied electric field. The rate at which the carriers move is mediated by the possibilities that any given electron will encounter the effects of another carrier, the lattice, or a lattice perturbation, creating a form of dampening or friction not present in free space. The interactive forces between the carrier and the lattice prevent the electron from achieving the free space velocity. The reduced velocity in a solid is called the drift velocity, given by the following expression,

Equation 3 - Drift Velocity - Applied Field Relationship

$$\upsilon_{Drift} = \mu E$$

where v_{Drift} is the drift velocity, μ is the mobility, and E is the applied field. The mobility relates the electric field vector to the velocity vector, which in a non-cubic lattice causes the mobility to be inherently directional.[9] The semiconductor's transport properties are the primary part of the system defined by an electronic device, with contacts and external components secondary considerations.

1.2 GaN Growth

Growth of gallium nitride through non-equilibrium methods has posed problems from the outset. Early investigations enumerated film properties by various growth methods, establishing high quality film benchmarks for devices demonstrating heterostructure designs. Strain is a limiting factor in any thin film deposition technique and complicates production of strain-enhanced devices. During deposition, strain results from thermal expansion, thermal capacity, thermal conductivity, and lattice spacing

mismatches between the deposited film and substrate. Strain introduces threading dislocations, and other defects, with unique spatial and energetic distributions depending on the localized phenomena during the growth. Matching lattice structural and thermal properties can minimize the deposition related strain, resultantly improving the electrical properties. Novel growth techniques can also reduce the strain, see section 1.2.2 Substrates, and density of extended defects, see section 1.4 Defects. The aspects of III-Nitride growth will be cursorily reviewed, with an emphasis on reports enumerating techniques for device quality properties. The facilities at MMDL are capable of both ammonia and nitrogen plasma source MBE, MOCVD, and HVPE.

1.2.1 Growth Techniques

Metal Organic Chemical Vapor Deposition (MOCVD), Hydride Vapor Phase Epitaxy (HVPE), and Molecular Beam Epitaxy (MBE) are the primary growth techniques for III-Nitride, and other wide band gap semiconductors. In MOCVD and HVPE growth, high temperatures are used to condense reactive gases onto a substrate, while MBE uses reactive plasma and thermally excited metallic species to deposited thin films. The high deposition rate deposition techniques are MOCVD, typically in the range of micrometers per hour, and HVPE, 10's of μm per hour. MOCVD produces higher quality films than HVPE of comparable thickness, but HVPE can achieve higher quality films through sheer thickness. MBE is limited to hundreds of nanometers per hour, with film quality dictating the deposition rate. A complex relationship exists between the

substrate temperature, deposition rates, and associated deposition parameters. The growth technique employed is generally determined by the film's structure.

1.2.1.1 Hydride Vapor Phase Epitaxy (HVPE)

HVPE films of GaN are characterized by smooth surfaces with low density of dislocations, predominantly of the screw type. HVPE reactors produce superior electrical characteristics over MOCVD or MBE films, mainly as a result of thicker films. Dislocation densities of HVPE films are generally in the range of 10^8 cm^{-2}. HVPE has two distinct advantages, high growth rates and uniformity over a large substrate area. The particular dynamics of HVPE deposition cannot produce heterostructures. Despite the shortcomings, HVPE films provide a high quality standard and make excellent templates for the growth of heterostructure films by other techniques.

1.2.1.2 Metalorganic Chemical Vapor Deposition (MOCVD)

Metal organic chemical vapor deposition relies on reactive gases at variable pressures to force a gas condensation reaction that deposits material onto a substrate. Process pressures can range from sub atmosphere to positive pressures depending on the vessel and application. The background carrier concentration can be minimized in MOCVD depositions, just as HVPE, yielding carrier concentrations as low as ~ 2×10^{16} cm^{-3}.[10] Larger substrates can also be accommodated in MOCVD reactors with high uniformity and quality.[11] Substrate temperatures range around 1050 °C for GaN, but is highly dependent on the application. Special care must be taken with MOCVD systems,

as many of the process gases, such as trimethylgallium (TMGa), trimethylaluminum (TMAl), and ammonia (NH_3), are caustic or unstable in atmosphere.

1.2.1.3 Molecular Beam Epitaxy (MBE)

Out of the growth techniques the most selective is MBE, coined a 2-D growth technique. In MBE deposition, solid sources are supplied to the process chamber via effusion cells. Nitrogen is supplied to the chamber as either gaseous ammonia or activated nitrogen from a plasma source. Chamber background pressures during deposition are ideally less than 10^{-6} Torr, but more commonly are ~ 10^{-4} Torr. The lowest chamber base pressure is desirable, as it will minimize the impurity incorporation in the III-Nitride film from the background partial pressures of gaseous species. Substrate temperatures vary but must be maintained below the thermal desorption point of the III-Nitride. One can roughly approximate the growth stoichiometry by calculating the ion fluxes, examining RHEED patterns, or though ex-situ surface microscopy. Heterostructure device structures would be increasingly difficult to deposit without the use of MBE.

1.2.2 Substrates

The most critical factor in growth of III-Nitrides is the substrate type and preparation. In selecting a substrate, the lattice spacing and thermal expansion coefficients need to be matched as closely as possible. The III-Nitride family has a match with a number of other materials, providing for a large variety of candidates for heteroepitaxy. Sapphire (Al_2O_3) is the most popular choice for heteroepitaxy in III-

Nitride growth, though other candidates are zinc oxide (ZnO), silicon carbide (SiC), spinel, gallium arsnide, and silicon, see reference 1 for in-depth treatment of various wide band gap materials' growth related issues.

In the ideal case of homoepitaxy, threading dislocations and native point defects mediate the electrical quality of the deposited GaN. Heteroepitaxial overgrowths are more susceptible to substrate preparation and the resulting overgrown film quality is generally poorer than in the case of homoepitaxy. On sapphire AlN buffers are utilized to improve the GaN film quality. Incorporation of super lattices in the overgrowth has been shown to be effective in improving the electrical properties of the bulk material by reducing the propagation of threading dislocations, see section 3.1.2 SVT 750.

Substrate selection may be complicated by polarization charges exhibited by the III-Nitride family. A study of two dimensional electron gas (2-DEG) heterostructures composed of 25 nm thick barriers of $Al_{0.25}Ga_{0.75}N$ on GaN determined the 2-DEG properties were a strong function of substrate and preparation.[12] The heterostructures were deposited on Zn compensated HVPE films with a room temperature resistivity of 10^8 Ω-cm or greater. The results found that the 2-DEG characteristics are compromised by the presence of a volume of charge at the MBE / HVPE interface (~ 2×10^{18} cm^{-3}). Obtaining a higher purity source for the HVPE processes alleviated the extraneous interface charge and yielded state of the art transistor characteristics reiterating the stringent requirements of the III-nitride materials.

Many of the films at MMDL were MBE GaN heteroepitaxial overgrowths on sapphire. The sapphire substrates were degreased three times for 5 minutes in

trichloroethane at 300 °C, followed by a 3 minute deionized water rinse. Degreasing was followed by a 300 °C 3:1 H_2SO_4:H_3PO_4 etch to remove surface damage from the substrate. Then the sapphire substrate was annealed outside and inside the vacuum chamber before deposition. Annealing in the vacuum chamber was performed around 950 °C and was followed by conditioning with Rf nitrogen or NH_3 flux, termed substrate nitridation. The nitridation reconstructed the sapphire substrate's surface into a thin AlN layer, verified by reflective high-energy electron diffraction (RHEED). The use of AlN buffers is essential in achieving high quality films of heteroepitxial MBE GaN on sapphire. The prohibitive cost of substrates and the intricacies of substrate preparation have lead many to investigate alternatives to traditional substrates.

1.2.2.1 Nanoporous and Nanotemplate Substrates

Progressive alternative techniques incorporated lateral epitaxial overgrowth with nanoporous or nanotemplate substrates. Lateral epitaxial overgrowth (LEO) utilizes orientation dependent growth rates and conditions to cause the growth of the film to proceed out-of-plane until a critical thickness is reached, then in-plane growth is initiated. Dislocation densities in the low 10^{-6} cm^{-2} can be achieved in the highest quality region of a LEO overgrowth. Through optimizing surface geometries, density, and island size of the nanotemplates, maximum relief of strain and highest film quality can be achieved. Surface tension, growth kinetics, and crystal symmetry define the islands' characteristics. Similarly, templates and nanoporous materials can also drastically reduce the number of dislocations in overgrown thin-films. Nanoporous titanium nitride (TiN), SiC, or GaN offer a novel mechanism for relaxing the strain of the initiating growth by selectively

nucleating on the exposed reduced area surface. Patterning materials, such as AlN, in stripes, columns, rings, and islands offers other possibilities of reducing epitaxial strain.

A novel method investigated at MMDL during these studies for homoepitaxial GaN nanotemplate growth involved etching a GaN thin film in molten potassium hydroxide to reveal its defect structure, while simultaneously defining a growth template. The substrate's defect structure becomes the template for initiating the subsequent thin film's growth, ideally decreasing the strain induced in the film and consequently the threading dislocations, see section 3.1.4 SVT 1026 and SVT 1460.

Analysis of anistropic etches and nanotemplate regrowth studies will provide critical information on achieving lower dislocation densities in GaN growth. Dislocation densities in the low 10^8 cm^{-2} range for MBE III-Nitride films on sapphire are a realistic goal, as compared to dislocation densities in the mid $10^9 - 10^{11}$ commonly achieved utilizing AlN buffers on sapphire. Nanopatterning and nanotemplating offer a low cost alternative that will advance state of the art devices for all materials.

1.3 Material Properties

Pure elements and elemental compounds have parameters that describe their bulk properties. When examining various samples of a particular compound there will be a distribution in material properties due to the microscopic variations in the samples. The following subsections categorize material properties into five basic categories: mechanical, alloy, electrical, optical, and chemical properties. In a separate class of materials, polycrystalline and porous substances have significantly different properties

than a pure crystalline specimen. Contributions of grain interactions and surface versus volume effects distort the pure elemental properties in a given specimen of a material. Accompanying, are brief comments through the various sections on the novel properties of poly- and nanomaterials.

1.3.1 Mechanical Properties

A crystal's symmetry and periodicity not only defines the energy structure for electron energy transitions; it also defines the energy spectrum for the mechanical coupling of neighboring atoms in the bulk of the material. Gallium nitride has an in-plane lattice spacing, a, of 0.3188 nm and an out of plane lattice spacing, c, of 0.5185 nm.[13] Bulk mechanical properties are defined as hardness, thermal conductivity, Raman spectra, and elastic constants. The hardness of GaN is reported by two techniques, nanoindentation and the Knoop method, as 15.5 ± 9 and 10.8 GPa, respectfully.[13] From a microscopic point of view the unit cell type, and corresponding bonding angles and energies, define the macroscopic mechanical properties. Defects and strain will serve to reduce the values of most of the macroscopic parameters, as a result the cumulative effects of the unique microscopic configurations.

A material's response to deformation is characterized by the elastic constants for the given material. There are 36 numbers required from theory to describe mechanical deformation, though the actual number of elastic constants that are necessary to describe a given material's bulk properties are determined by symmetry.[14] In a wurzitic crystal, there are five elastic constants, while in a cubic crystal there are only three. Equation 4 -

Cubic Crystal Elastic Constants, describes the symmetry relationships for the three elastic constants for a cubic crystal as follows:

Equation 4 - Cubic Crystal Elastic Constants

$$c_{11} = c_{xxxx} = c_{yyyy} = c_{zzzz};$$
$$c_{12} = c_{xxyy} = c_{yyzz} = c_{zzxx};$$
$$c_{44} = c_{xyxy} = c_{yzyz} = c_{zxzx};$$

The elastic modulii result from the relationship of the strain tensor to the conservation of potential energy in a harmonic crystal system. [14] The modulus of elasticity for GaN was reported as 210 ± 23 GPa.[13] The elastic modulii are used in a number of higher-level calculations, such as scattering mechanisms and strain induced polarization charge to account for the effects of strain on the lattice and carriers.

Defects play an important role in the mechanical properties, there are a number of physically imposed perturbations in mechanical properties due to defects, just as there are in electrical properties. The interplay of macroscopic properties and microscopic defects is evidenced in decreased sheer strength as a direct result of numerous threading dislocations, stacking faults, or nanopipes. Local perturbations have unique bonding angles, energies, and can have unique symmetry groups depending on the chemical species involved. The environmental history of the material is a critical factor in determining defects' effects on mechanical properties, as well as on the optical, electrical, and chemical properties.

Perturbations to the lattice structure will manifest a peak in X-ray and Raman spectroscopy if the density of defects is comparable to the bulk signal. The new phonon

modes could be equally damaging to the electrical characteristics, as the acoustic phonons could assist in forms of defect conduction, possibly Hopping Conductivity. A result of non-ideal growth conditions, stacking faults, grain boundaries, high residual film stress, and / or a high density of threading dislocations compromise the shear strength, heat capacitance and conductance, structural properties, and elastic modulus of a semiconductor film.

1.3.2 Alloys' Properties

Increasingly, devices and materials are comprised of alloys. Alloys present a challenge in that there is an enormous amount of sample parameter space that must be explored to establish fundamental relationships with elemental composition. In the simple case, alloys' properties could be assumed to be a linear interpolation between the two binary compounds' properties. However, if one of the constituent elements has a dominating effect, a bowing parameter more correctly describes the transition of a material's property with alloy content, such is the case in the III-Nitrides. An additional effect when dealing with alloys that must be considered is some non-uniform distribution of the alloy constituents, or phase precipitations. If the alloy concentration fluctuates due to dislocation mitigated stress, or some other phenomena, the above expressions would only be a wild guess at the real nature of the polarization effects about the heterointerface. Many of the properties in the material will be a function of the alloy concentration and the following list presents the immediate parameters of concern. The dielectric constant, which measures the polarizability of the material, assumes the following form

Equation 5 - Alloy Dielectric Constant

$$\varepsilon_{AlGaN}(x) = 0.03x + 10.28$$
$$\varepsilon_{InGaN}(x) = 4.33x + 10.28$$
$$\varepsilon_{AlInN}(x) = -4.3x + 14.61$$

where x is the alloy concentration of the first cation. The bandgap of the alloy material, Equation 6 - Alloy Bandgap Relationship,[15]

Equation 6 - Alloy Bandgap Relationship

$$E_{AlGaN}{}^{g}(x) = 6.13x + 3.42(1-x) - 1.0x(1-x) \quad \{eV\}$$
$$E_{InGaN}{}^{g}(x) = 1.95x + 3.42(1-x) - 2.5x(1-x) \quad \{eV\}$$
$$E_{AlInN}{}^{g}(x) = 6.13x + 1.95(1-x) - 5.4x(1-x) \quad \{eV\}$$

and band offsets, Equation 7 - Alloy Band Offset Relationship, will vary as

Equation 7 - Alloy Band Offset Relationship

$$\Delta E^{C}_{ABN}(x) = 0.63\left(E^{g}_{ABN}(x) - E^{g}_{ABN}(0)\right)$$

where again x is the mole fraction of the first cation in the III-Nitride alloy. The last concern with alloy composition and material parameters involves the Schottky barrier at the surface of the alloy in the case of a III-Nitride MODFET. The following expression, Equation 8 - Alloy Schottky Barrier Height Relationship, relates the mole fraction, x, to the Schottky barrier height, ϕ.

Equation 8 - Alloy Schottky Barrier Height Relationship

$$e\phi_{AlGaN}(x) = 1.3x + 0.84 \quad \{eV\}$$
$$e\phi_{InGaN}(x) = -0.36x + 0.84 \quad \{eV\}$$
$$e\phi_{AlInN}(x) = 1.66x + 0.48 \quad \{eV\}$$

The variance in material parameters with alloy composition is a crucial engineering aspect for the III-Nitride MODFET's. Through utilization of the alloy composition and thickness, devices can be tailored to specific applications.

Polarization charge, resulting from the ionic nature of the III-Nitride semiconductors, is an additional effect that must be considered at interfaces. Polarization manifest in two forms, spontaneous and piezoelectric. Spontaneous polarization is a fixed charge that results from the ionic displacement along the c-axis in the unit cell. Piezoelectric charge on the other hand is determined from the degree of strain in the film. In MODFET's this charge can be utilized to increase the 2-DEG concentration at the heterointerface. The total polarization in a film is given by the following expressions, Equation 9 - Alloy Interface Polarization Charge Relationship, for a heterostructure and surface, where it is assumed that the film is on a GaN buffer.

Equation 9 - Alloy Interface Polarization Charge Relationship

Heterostructure $$P_{ABN} = P_{ABN} = P_{ABN}^{SP} + P_{ABN}^{pz}$$

Surface $$P_{ABN/GaN} = P_{GaN} - P_{ABN}$$
$$= \left(P_{GaN}^{SP} + P_{GaN}^{pz}\right) - \left(P_{ABN}^{SP} + P_{ABN}^{pz}\right)$$

The variables P_{ABN}^{SP} and P_{ABN}^{pz} are the total spontaneous and piezoelectric contributions to the polarization charge and P_{GaN}^{SP} and P_{GaN}^{pz} represent the spontaneous and piezoelectric of the GaN buffer. A MODFET's peak current capacity and switching times can be improved by tailoring a heterostructure design to balance the density of strain induced polarization charge and the mobility of the carriers confined at the interface.

1.3.2.1 Spontaneous Polarization

Spontaneous polarization can be characterized by a linear interpolation, though Ambacher *et al.* propose a quadratic term for more accurate description of the spontaneous polarization charge magnitude in the III-Nitrides.[15] The general form of Vegard's Law and the expressions for spontaneous polarization in AlGaN, InGaN, and AlInN are as follows in Equation 10 - Alloy Spontaneous Polarization, noting the bowing parameter b=0 would be the equivalent of a linear interpolation.

Equation 10 - Alloy Spontaneous Polarization

$$P_{ABN}^{SP}(x) = P_{AN}^{SP}x + P_{BN}^{SP}(1-x) + bx(1-x)$$
$$P_{AlGaN}^{SP}(x) = -0.09x - 0.034(1-x) + 0.021x(1-x)$$
$$P_{InGaN}^{SP}(x) = -0.042x - 0.034(1-x) + 0.037x(1-x)$$
$$P_{AlInN}^{SP}(x) = -0.09x + 0.042(1-x) + 0.07x(1-x)$$

The coefficients P_{AN}^{SP} and P_{BN}^{SP} are determined from characteristics of the unit cell, values for the III-Nitrides can be found in reference 15, or from Equation 10 - Alloy Spontaneous Polarization. It is important to remember that in the III-Nitrides the total polarization charge is a function of the spontaneous and piezoelectric polarization.

1.3.2.2 Piezoelectric Polarization

Polarization charge not only results from the affective charge displacement of the unit cells, but also originates in the form of piezoelectric polarization from strain on the unit cells due to lattice or thermal mismatches between materials. An overview, and a brief derivation, of the parameters involved in calculating piezoelectric polarization charge effects follows, for a more in-depth treatment please refer to reference 15.

A gauge of in-plane to out-of-plane stress is represented by Poisson's ratio, given by the following expression for hexagonal symmetry.

Equation 11 - Poisson's Ratio

$$\nu(0001) = 2\frac{C_{13}}{C_{33}}$$

In the above expression, ν is the out of plane strain and C_{XX} is the elastic constant for the respective directions. The stress in a given direction can be related to internal or external forces using Hooke's law as defined by

Equation 12 - Hooke's Law

$$\sigma_{ij} = \sum C_{ijkl}\varepsilon_{kl}$$

where ε_{kl} is the crystal deformation and C_{ijkl} represents the elastic constants, defined following.

Equation 13 - Elastic Constant Definition

$$C_{ij} = \begin{pmatrix} C_{11} & C_{12} & C_{13} & 0 & 0 & 0 \\ C_{12} & C_{11} & C_{13} & 0 & 0 & 0 \\ C_{13} & C_{13} & C_{33} & 0 & 0 & 0 \\ 0 & 0 & 0 & C_{44} & 0 & 0 \\ 0 & 0 & 0 & 0 & C_{44} & 0 \\ 0 & 0 & 0 & 0 & 0 & \frac{1}{2}(C_{11} - C_{12}) \end{pmatrix}$$

Knowing the stress, or strain, in the film is the critical aspect to calculation of the piezoelectric polarization, in the simplified form of the strain, ε, in the out-of-plane direction is defined as

Equation 14 - Simplified Out-of-Plane Strain

$$\varepsilon_1 = \frac{a_{buffer} - a(x)}{a(x)}$$

where *a* respectfully represents the lattice parameters of the materials under investigation. The following expression relates the film stress, σ, and piezoelastic modulii, d_{ij}, to the piezoelectric polarization, P_i^{pz}.

Equation 15 - Piezoelectric Polarization

$$P_i^{pz} = \sum_i d_{il}\sigma_l \quad i = 1,2,3 \quad l = 1,\ldots,6$$

In this most general form, symmetry for the wurzitic crystal structure has not been accounted for; therefore, simplifications can be made using the following symmetry relations:

Equation 16 - Piezoelastic Modulii Relationships for Hexagonal Symmetry

$$d_{31} = d_{32},$$

$$d_{33} = 0,$$

$$d_{15} = d_{24}, \text{ and}$$

$$\text{all other } d_{il} = 0.$$

The piezoelectric polarization charge then reduces to,

Equation 17 - Piezoelectric Polarization with Symmetry Imposed

$$P_1^{pz} = \frac{1}{2} d_{15} \sigma_5$$

$$P_2^{pz} = \frac{1}{2} d_{15} \sigma_4$$

$$P_3^{pz} = d_{31}(\sigma_1 + \sigma_2) + d_{33} \sigma_3$$

where the symmetry must be considered for the directionality of stress in the film. In the case of interest, biaxial stress is isotropic, equal in the x and y directions, yielding $\sigma_1 = \sigma_2$, while the out of plane stress, σ_3, and the sheer stresses, σ_4 and σ_5, are zero. Making these assumptions allows for further simplification of the piezoelectric polarization in the film, resulting only in an in-growth plane piezoelectric polarization charge given by,

Equation 18 - Simplified Out-of-Plane Piezoelectric Polarization

$$P_3^{pz} = 2 d_{31} \sigma_1 = 2 d_{31} \varepsilon_1 \left(C_{11} + C_{12} - 2 \frac{C_{13}^2}{C_{33}} \right)$$

utilizing the following simplified expression for the stress.

Equation 19 - Simplified Stress Relationship

$$\sigma_1 = \varepsilon_1 \left(C_{11} + C_{12} - 2 \frac{C_{13}^{\ 2}}{C_{33}} \right)$$

The final simplified form of the piezoelectric stress follows as:

Equation 20 - Piezoelectric Polarization

$$\begin{aligned} P_3^{pz} &= \varepsilon_1 e_{31} + \varepsilon_2 e_{32} + \varepsilon_3 e_{33} \\ &= 2 \varepsilon_1 e_{31} + \varepsilon_3 e_{33} \\ &= 2 \varepsilon_1 \left(e_{31} - e_{33} \frac{C_{13}}{C_{33}} \right) \end{aligned}$$

Given the above expression a set of expressions representing the piezoelectric polarization for some of the III-Nitride alloys is presented from ref. 15.

Equation 21 - Alloy Piezoelectric Expressions

$$P^{pz}_{InGaN/InN}(x) = [-0.113(1-x) - 0.0276x(1-x)] \quad Cm^{-2}$$
$$P^{pz}_{InGaN/GaN}(x) = [0.148x + 0.0424x(1-x)] \quad Cm^{-2}$$
$$P^{pz}_{InGaN/AlN}(x) = [0.182x + 0.0.026(1-x) + 0.0456x(1-x)] \quad Cm^{-2}$$

$$P^{pz}_{AlInN/InN}(x) = [-0.28x + 0.104x(1-x)] \quad Cm^{-2}$$
$$P^{pz}_{AlInN/GaN}(x) = [-0.0525x + 0.148(1-x) + 0.0938x(1-x)] \quad Cm^{-2}$$
$$P^{pz}_{AlInN/AlN}(x) = [0.182(1-x) + 0.092x(1-x)] \quad Cm^{-2}$$

$$P^{pz}_{AlGaN/InN}(x) = [-0.28x - 0.113(1-x) + 0.042x(1-x)] \quad Cm^{-2}$$
$$P^{pz}_{AlGaN/GaN}(x) = [-0.0525x + 0.0282x(1-x)] \quad Cm^{-2}$$
$$P^{pz}_{AlGaN/AlN}(x) = [0.026(1-x) + 0.0248x(1-x)] \quad Cm^{-2}$$

Piezoelectric polarization is characterized in units of current density and all of the above expressions have taken into account the non-linear bowing parameter encompassing Vegard's Law.

1.3.3 Electronic Properties

The crystal purity, both structurally and compositional, doping, and the system created by contacts to the semiconductor determine the conduction due to an applied potential. Topics of interest in electrical device applications are the semiconductor's quality defined by doping profile, mobility characteristics, conductivity / resistivity, and dielectric quality. Neglecting defects until section 1.4 Defects and contacts until section

2.2 Electrical Measurements; the current density in a doped semiconductor due to an applied electric field is given by the following relationship,

Equation 22 - Current Density – Conductivity – Electric Field Relationship

$$J_{Drift} = \sigma \mathrm{E}$$

where J_{Drift} is the drift current density, units A / cm^2, σ is the conductivity, and E is the applied electric field. The conductivity and resistivity expressions form a macroscopic basis for understanding the behavior of carriers in the presence of an applied field. In an ideal doped semiconductor, the material has a finite number of thermally excitable states near the conduction band edge, providing a doping dependent conductivity, σ, and resistivity, ρ, given by the following equation:

Equation 23 - Conductivity – Resistivity Doping Relationship

$$\sigma = \frac{1}{\rho} = q\left(\mu_n n + \mu_p p\right)$$

In the above equation, q represents the fundamental charge constant, μ_n and μ_p are the electron and hole mobilitites, and n and p are the electron and hole concentrations. The take away is: a semiconductor's conductivity is related to the mobility and density of carriers. Inaccurately assuming a static carrier concentration, carrier mobility limits the conduction. If ionization of dopants is 100% then doping concentration, N_D, is equal to the free electron concentration, n, noting n is a function of temperature. If only a percentage of the dopant states are thermally activated at room temperature then, carrier concentration models become more complex. For instance, during operation as a device

experiences self-heating the conductivity will change because of increased carriers and decreased mobility.

The mobility is a macroscopic characteristic of a material that is composed from a collection of expressions based in quantum mechanics: scattering mechanisms. Conduction should ideally be limited by a specific scattering mechanism, or corresponding mobility, in a given device structure. The microscopic formulation of scattering mechanisms is developed from the Boltzmann Transport Equation and collision integrals, in which a one-electron picture of a scattering mechanism is applied to the large number of electrons in a solid state device. The relaxation time approximation assigns a time constant to given scattering event, which characterizes the average time it takes a carrier to return to random motion. In reality, a proportion of the electrons will be in a given state as a result of the various scattering mechanisms acting in parallel, with a dominant effect limiting the mobility. The measured mobility will be dominated by the lowest mobility, or longest relaxation time, as shown by the following expression, referred to as Matheson's rule.[1]

Equation 24 - Matheson's Rule

$$\frac{1}{\mu_{Matheson}} = \frac{1}{\mu_a} + \frac{1}{\mu_b} \cdots + \frac{1}{\mu_z}$$

Where $\mu_{Matheson}$, is the measured mobility, and μ_a, μ_b, and μ_z represent the various mobilities associated with a given scattering mechanism.

Any semiconductor's electronic structure and conduction can be described on a first order with the above expressions and relationships. In practice, only semiconductor

resistors can be understood with the proceeding framework. Other devices, such as p-n junctions, LED's, and field effect transistors (FET's), need further development of conduction concepts involving contacts. Additionally, in highly defective material the above relations will not hold, as the appropriate expression is a function of the type of defect, and may become spatially and / or temporally dependent. In all devices, the leakage microstructure is of immediate importance. Consequences of alternate conduction paths are effective shorting of the device, a reduction in the current density, or perturbations in the dynamics of carriers. As a result, it is essential to correlate GaN material properties with the factors involved in producing reliable quality contacts for electronic devices.

In switching, or optoelectronic devices, the charge separation characteristics of the material are of interest. The dielectric of the semiconductor determines electrical properties, such as the capacitance. In MODFET's the gate capacitance, a function of the space charge depletion region created by the gate Schottky contact, determines transient characteristics. Maxwell's equations relate the electric flux density, D, to the electric field intensity, E, through the relative permativity, ε, or dielectric constant.

Equation 25 - Electric Flux-Density Correlation

$$D = \varepsilon E$$

The permativity of a material, ε_s, is defined as:

Equation 26 - Material Specific Dielectric

$$\varepsilon_S = \varepsilon_r \varepsilon_0$$

where ε_r is the permativity constant of a material and ε_0 is the relative permativity constant, 8.85×10^{-14} F/cm^{-2}. The permativity of a material is a tensor in certain cases of symmetry, and is a function of applied field intensity close to break down fields. The Clausis-Mossotti relation describes the relationship between the permativity and the atomic polarizability of the material. There are two sources of polarizability: atomic and displacement. Atomic polarizability is a function of charge localization around the individual elemental species of a material, while displacement is a function of the interactions of neighboring elemental species in a material. The index of refraction is related to the square root of the relative permativity.

1.3.4 Optical Properties

The bandgaps of AlN, GaN, and InN are 6.2, 3.4, and 0.9 eV. Using the above expressions, a bandgap from 0.8 to 6.2 eV could be possible by varying the mole fraction of the alloys.[11] Native defects limit the quality of optical devices by all growth techniques. Novel dopants have produced unique optical spectra and electrical characteristics. For example, Erbium doping of GaN can effect the optical properties, green electroluminescence peaks at 537 nm dominant over 300 K and 558 nm dominant under 240 K.[16] Additionally, Erbium doping introduces peaks in the IR spectrum centered around 1550 nm and is cited as causing a defect related Frenkel-Poole conduction mechanism. ITO contacts have propelled UV-detectors into new benchmark regions, providing transparent contacts with increased efficiencies and superb contact properties.[17] In the case of optical / electromagnetic detectors or emitters the semiconductor's bandgap will determine the electromagnetic coupling. Heterostructures can also be used to tailor

optical properties, taking advantage of quantum well states. However, poor quality material cannot adequately confine carriers in heterostructures, rendering the optical properties distorted at best.

1.3.5 Chemical and Thermal Properties

Operating conditions for high quality GaN, devices have higher operating temperatures and improved resistance to corrosion over current microelectronic counterparts. The thermal conductivity of GaN is 2.1 W/cm K, and the heat capacity is 35.3 J/mol K. The melting point of GaN is reported as 2573 GPa at 60 Kbar.[13] GaN is virtually unaffected in concentrated room temperature acids, bases, and alkali.[1] Elevated temperatures of these chemicals can successfully attack defective regions, as can electrochemical etching. Chemical etches are described more in the fabrication section 2.5 Sample Preparation. Thermo-chemical stability of the III-Nitrides provides the possibilities of other novel applications, such as: gas,[18] pH,[19] and pressure sensors.[20]

1.4 Defects

Semiconductors are reliant not only on their physical structure, but more importantly on their energy structure when concerned with electronic device characteristics. Uniformly perturbing the energy structure allows engineers to create an array of devices from a base material. Defects alter the intentional perturbations, distorting distributions and properties of the electronic devices. For GaN, native defects act as shallow donor defects, and other unintentional defects limit the conduction due to scattering, trapping, or nonlinear field responses. In reality, the surface, grain boundaries,

stacking faults, interstitial impurities, substitutional impurities, vacancies, and any other physical non-idealities in sufficient quantity, or confinement, will introduce a perturbation in the periodic crystalline structure. Defects with states inside the bandgap of the material, that create scattering centers, or that form a lower parallel resistance are of immediate concern for electron devices. Corrections must be made to the processes involved in producing the device or material. Groups have employed numerous tactics to passivate GaN films and minimize the consequences of poor material. Approaches for passivation will be covered in section 2.5 Sample Preparation.

1.4.1 Point Defects

Point defects are the nemesis of electrical devices, they consume power, introduce time-delay effects, memory, anomalous conduction, and irreproducible results. Due to the difficulties in growing GaN, point defect concentrations can be considerable. Vacancies, substitutions, or interstitial point defects introduced into the lattice structure cause bond lengths to be elongated or compressed, in addition to possibly causing a distortion of the bonding angles. Theoretical studies use molecular dynamics to model the structural and energetic shifts associated with point / extended defects. Theoretical explications for native defects are an essential basis that must be established to interpret results for spectroscopy of deep levels. The fine structure of point defects can be resolved with an electrical technique known as deep level transient spectroscopy (DLTS). Results from various groups on the point defect structure of n and p-type GaN resolved using DLTS are presented in section 2.2.4 Deep Level Transient Spectroscopy (DLTS). Point defects, the primary affecter of electrical activity in semiconductors, can be single or multiple

charge traps, with a neutral charge in the filled or empty states. Donor type native point defects are the nitrogen vacancy and the triply charged Ga interstitial state.

The states of the N vacancy are a direct result of high-energy Ga dangling bonds, causing a Coulomb potential about the vacancy that creates a binding effective mass state.[21] The N-vacancy, with formation energy of 3.2 eV, is identified as having an energy 0.8 eV, and a splitting level at 0.5 eV, above the conduction band. Conversely, the Ga vacancy has an associated formation energy of 8.1 eV and defect energy level 0.3 eV, band splitting level at 0.1 eV, above the valence band. Dangling N-bonds populate the Ga vacancy with three electrons in a neutral state.

The Ga antisite elongates the bond lengths by 11.3% and 15%, introducing strain and defect levels at 1.4 and 2.1 eV above valance band edge. The neutral state of the Ga-antisite traps four electrons. The N antisite contracts the type-1 neighbor bond length by 29% and elongates the type-2 neighbor bond length by 11%. Two energy levels are introduced, 0.4 eV above the valance band and 0.2 eV below conduction band by the shift introduced by the nearest neighbor shift. The conduction band state cannot be populated due to electron-electron interactions, a repulsion energy ~ 0.95 eV.

Interstitial Ga has two possible manifestations. The first interstitial, labeled T type, causes a neutral complex in which two Ga^{2+} ions exchange charge leaving one in a 3+ state and the other in a 1+ state. The Ga T-type interstitial has an associated defect level of 1.8 eV below and resonance at 1 eV above the conduction band edge. The conduction band resonance state for the (+/3+) state cannot be occupied, while the midgap state is doubly occupied. The N vacancy is isomorphic for both the T or O type

interstitial. A triply occupied state is formed 1 eV above the valance band, with 0.1 eV band splitting.

Other elemental impurities can manifest as interstitials or substitutions in the lattice. In the worst case there is a precipitate or phase segregation due to the impurity incorporation, which could have detrimental effects on the electronic, optical, thermo-chemical, and mechanical properties. Films also have the ability to absorb certain gases, such as H_2, which may significantly change the electrical characteristics of the film and defect structure. Impurities, and more generally defects, can significantly alter the stress and strain in a film on local and global scales. Just as electronic bands shift in the presence of stress or strain, point defect energies will also shift.

1.4.2 Extended

Reverse leakage current has been ascribed to extended defects, such as screw[22] and others.[23] Groups have refined the structural, chemical, and energetic aspects of extended defects and relevant theoretical explications of excess current leakage. [24, 25] Threading edge dislocations, Burger's vector (b = (a/3)[1-210]), and open core screw dislocations are reported by local density orbital (LDO) calculations to relax by forming a [10-10] similar surface normal to the c-plane at the core of the respective dislocations. In the [10-10] surface the atoms arrange in a three fold symmetry, while a [10-10] similar surface shows the same type of sp^2 (p^3) hybridization with less regular arrangement. Edge dislocations demonstrate a three fold symmetry rearrangement in the core, reducing the energetics of the dislocation, permitting only shallow states, and leading to compressive (~ 9%) and tensile strain (~13%) in the surrounding areas. The full core

screw dislocation has strong distortions in bond lengths, ~ 0.4 Å, along the core, leading to high line energies and midgap states ranging in energy from E_v + 0.9 eV to E_v + 1.6 eV. Open core simulations show the maximum diameter of open core screw dislocations to be ~ 7.2 Å, with a 0.2 Å elongation of the bond length and states outside of the bandgap. Edge dislocation line energies are reported to be 2.19 eV $Å^{-1}$, with less than 15% Ga vacancies, while full and open core screw dislocation line energies are 4.88 eV $Å^{-1}$. Although the line energies of the threading edge and open core screw dislocations are large, they cannot account alone for the leakage current measured in some films. The V/III ratio has been reported to be the primary affecter for screw dislocation electrical activity in MBE GaN thin films.[22]

Near surface Ga vacancies, and oxygen related point defects, are considered likely candidates for current leakage and yellow luminescence band in n-type material, though their relationship with structural threading dislocations has not been experimentally established. Another possibility is point defect concentrations are influenced by the presence of extended defects, providing a large distribution of midgap energies necessary to account for leakage current and yellow luminescence. The strain introduced by the crystallographic perturbation of the extended defect during growth causes a source or attractor for point defects. Dislocations, point defects, or inversion domains may decorate the interface between stacking faults and grain boundaries drastically complicating the defect conduction structure.

1.4.3 Inversion Domains

GaN films also suffer from high concentrations of Inversion Domain Boundaries (IDB's), ~10^{7-11} cm^{-2}, depending on the growth conditions. Inversion domain boundaries are electrically inactive in most cases, though theoretical calculations detail Holt-type IDB's as potentially electrically active.[26] Dimitrakopulos *et al.* provide experimental evidence with HREM and XTEM, detailing the Holt transformation occurrence when stacking faults interact with normal inversion domains. When stacking faults associated with a step along the [10-10] direction of the inversion domain boundary are not conserved, the inversion domain boundary compensates by altering the stacking sequence, denoting a transition to a Holtz-type inversion domain boundary. If there are stacking faults adjacent to both sides of the inversion domain boundary, the inversion domain boundary will not undergo a transition to the Holtz-type as the stacking faults are conserved and do not create a domain separation. Inversion domain boundaries are also reported to have the ability to undergo successive transitions from Holtz-type to inversion domain boundaries, and vice versa.[26]

1.4.4 Nanopipes

Nanopipes have also been accredited with electrical activity.[23] Shiojimia *et al.* used an AFM with a conductive tip to determine the I-V and C-V characteristics of submicron Schottky diodes. After electrical characterization using IV and CV measurements, the contacts were removed with aqua regia. Subsequent AFM imaging determined where dislocations and nanopipes were located under the Schottky contacts.

The results of this study determined that edge and mixed dislocations did not contribute to current conduction fallacies, though nanopipes were a source of leakage and non-ideal transport. It would be reasonable to conclude that the core of nanopipes assumes a sp^2 (p^3) hybridization, in the same way open core screw dislocations relax, and the cores of the nanopipes may be more susceptible to gas adsorption.

2 Material and Device Characterization

Semiconductor characterization encompasses many techniques. The thrusts of material characterization focus on structural, chemical, mechanical, optical, magnetic, thermal, or electrical properties. To understand the complex nature of materials many techniques are used in conjunction to determine correlations between properties. If too few material, or process, parameters are, examined then erroneous conclusions may be reached. Three main types of characterization are determined to sufficiently describe semiconductor materials for device fabrication: structural, chemical, and electrical. Structural characterization is inevitably capable of limited characterization of the chemical composition. For bulk material, chemical analysis is generally a means of failure analysis because the composition can be inferred from other measurements (such as X-ray measurements). Studying charged carrier behavior could reveal a wealth of information about the bulk semiconductor material and metal-semiconductor interfaces. Advances in microscopy have lead to the development of numerous techniques that combine another form of analysis with surface imaging. Following, the techniques for which data is presented in this study, and other relevant techniques, will be reviewed with an emphasis on electrical measurements.

2.1 Structural and Chemical Measurements

The primary means of gauging the structural and chemical properties of the samples at MMDL relied on X-ray diffraction and photoluminescence measurements. Occasionally, direct measurements of the elemental composition are necessary, and include, but are not limited to, selective ion mass spectroscopy (SIM's), X-ray photoemission spectroscopy (XPS), and Auger spectroscopy. None of these measurements were taken on the samples in this study, though Phillips X–ray diffractometer and photoluminescence results are provided where available, courtesy Dr. Feng Yun and Dr. Michael Reshishikov respectfully. Transmission electron microscopy (TEM) reveals structural information on the most detailed level, provided where available.

2.1.1 X-ray Diffractometery

X-ray diffraction is used to characterize the lattice spacing in highly order materials. An X-ray apparatus is set up with an X-ray source incidence with the thin film's surface at a fixed angle. By scanning an X-ray detector across the path of reflected X-ray trajectories, the peaks in x-ray intensity can identify substances based on the relationship to lattice parameters. The spacing between chemical species, lattice parameters, and coordination of their bonds is determined by minimization of the Columbic potential of the unit cell during the deposition of the material and any post environmental aging or processing. Numerous structural defects that affect the orientation of the crystal can be identified with X-ray diffraction techniques, such as

grain boundaries or extended defects. X-ray diffraction is also capable of identifying the strain in a film, as bonding distances are compressed or elongated. Peak positions will be presented for the extended defect associated [0001] and [11-12] peaks, where available. In a vacuum system, electrons can also be used for diffraction techniques to investigate the surface, in-situ (RHEED) or in post deposition characterization (LHEED). Applicability of diffraction techniques to deposition processes is highly dependent on the physics of the process and chamber.

2.1.2 Photoluminescence (PL)

The most direct measurement of the quality of a material is photoluminescence measurements. The unique coupling between the semiconductor's electronic structure and electromagnetic radiation is directly probed with PL measurements by using high-energy ultra-violet light to excite an electron – hole pair. An ensemble of physical processes, each having a characteristic PL signature, occurs during the instance of illumination with above bandgap energy. The electron – hole pair last for some time depending on microscopic conditions, eventually recombining to create a photon. Depending on film thickness, surface roughness, and index of refraction, the collection of photons is emitted at some angle and intensity. This optical flux is measured in a spectrometer and transferred to a computer software package. Due to the large density of defects in GaN, there is a broad yellow peak in the spectra. The source of this band is believed to be a native defect, though the exact source is in debate. The bandgap of GaN is identified in a PL spectra as the sharp peak at 3.4~3.5 eV. If the film is under

compressive or tensile strain, there will be a red or blue shift in the bandgap peak, verifying the coupling of strain to effective mass states.

2.2 Electrical Measurements

Contact metallizations are specific to the material system and device structure under investigation. There are two main aspects of a device, the substrate and the contacts. The substrate determines in most cases the device quality, while contacts manipulate potentials and current flow through the device. If a material yields current responses of a non-ideal nature, then additional effort is needed to refine the semiconductor thin film production and device fabrication processes involved.

All devices, whether p-n junctions, heterostructure field effect devices, or optoelectronics require Ohmic and / or Schottky contacts. The work function of the metal determines its rectifying ability for a given semiconductor. Ohmic contacts provide a linear response of current with an applied potential following Ohm's law. Assuming the semiconductor's resistivity is limiting the conduction, the expressions presented in section 1.3.3 Electronic Properties can be used to quantify the conductivity. Only Ohmic contacts are necessary when the bulk material is mediating the current responses, as in the case of a p-n junction or in a heterostructure detector. Schottky contacts are necessary for field effect devices, and are utilized as diodes due to the unique rectifying behavior. The Schottky contact is rectifying, conducts exponentially with positive applied biases and does not conduct under applied negative biases. Schottky contacts ideally demonstrate a single current response, however, defective material

produces a range of current responses. A further study of contacts and electrical measurements will follow.

Many sources of error can arise in techniques measuring conduction. Most notably is induced charge from either power supply fluctuations or electromagnetic interference as outside sources of error. Improving the quality of energy to the power source can control power supply fluctuations. In the worst cases, the power supply is the source of the noise. Testing with an oscilloscope in a low noise resistive network can help trouble shoot this problem, noting a oscilloscope should never be directly connected to any form of a power source unless care has been taken in determining input and output impedances and the power rating of the oscilloscope's input. External electromagnetic interference can be eliminated in several ways depending on the source of the extraneous radiation. Cabling can act as an antenna if improperly shielded or it is worn. Although coax cables have low LRC characteristics, at distances greater than two feet coupling becomes a problem. If the source of electromagnetic radiation is pervasive enough to generate current in the device under test, then more aggressive measures involving electromagnetic shielding needs to be considered. Effective EM shielding is composed of three layers of material with differing permeabilities. If possible, the source of the radiation should be eliminated through shielding; otherwise shielding the test apparatus is necessary.

Systematic errors, such as ground loop noise or integration errors are easier to correct than intrinsic noise sources, though identifying these sources can be problematic. Ground loop noise is generated when two independent structures that do not share an

electrical ground are coupled electrically. Much as sympathetic vibrations cause phonon coupling in musical instruments, oscillations in the ground connection of a test instrument can cause a reflection in a test apparatus. To eliminate ground loop noise, with a low impedance cable connect the ground on the measurement apparatus to the ground of the test apparatus. To illustrate the effects of ground loop noise Figure 3 - Ground Loop Noise shows the same device, SVT 750, measured with and with out the ground loop connection to the Kiethley 4200 SCS.

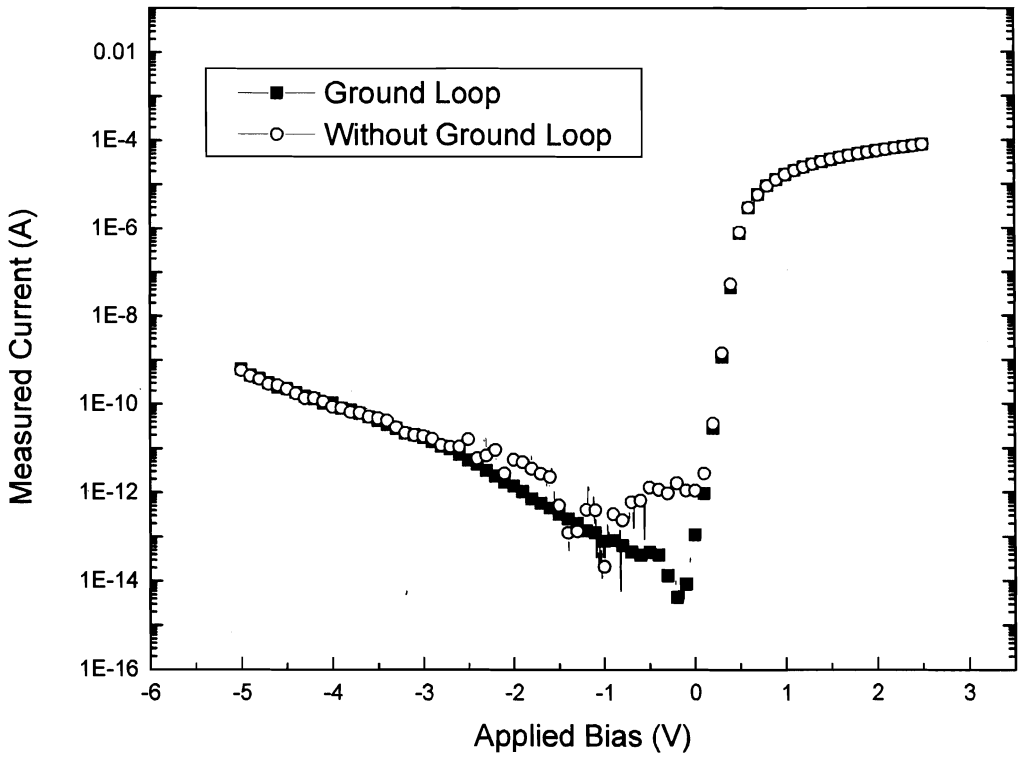

Figure 3 - Ground Loop Noise

Varying pressures of the electrical probes because of acoustic noise can also cause extraneous current measurements. Isolating the test apparatus from any hard surface will eliminate acoustic noise. Most measurement apparatus have some form of integration built into the system to improve measurement reliability. Integration error will occur if charging or device contact is a problem. In measuring the current response of defective material sweeping can cause discharging of defects from a previous measurement increasing the measured current for the current voltage point though it is actually conduction from a previously applied potential. The only solution is to wait longer periods before taking the next voltage measurement. Each electrical measurement setup is unique and must be verified.

Hall and four point probe measurements provide information about the resistivity of the material. Mobility characteristics are also determined from variable temperature Hall measurements. Hall measurements were performed on a Lake Shore system, capable of measurements down to 10 K. Various members of the lab contributed to the collection of Hall data, though Dr. Yun must be commended for his diligence in maintaining the system's operation.

Current voltage measurements analyze carrier transport in a semiconductor structure called a Schottky contact. Schottky contacts are a semiconductor interface with a metal having a work function energy greater than the sum of the semiconductor's Fermi energy and work function. A metal with a lower energy would create an Ohmic contact, as there is no impedance of electrons from occupied conduction band states of the semiconductor to unfilled states in the metal. Facilities exist to carry out IVT and CVT

measurements from 10 K to 400K, providing a first order analysis of defects and non-idealities in films at large, and DLTS measurements which reveal the deep level defect structure in high quality films. The IVT and CVT data presented was collected and analyzed by the author on the Kiethley 4200 SCS. There was no DLTS data collected for the samples in this study as either the devices had too small of a contact area or the semiconductor was too defective. Facilities are also present for high frequency and a variety of other electrical measurements, though their utilization had yet to be realized.

2.2.1 Hall Measurements

Hall Effect measurements are critical to semiconductor investigation, allowing quantification of carrier concentrations, dominant carrier type, and carrier mobility. Though the mobility can be measured from several experiments, the preferable method is the Hall experiment due to the ability to probe the temperature dependency of the mobility and carrier concentration. Analytical expressions exist that characterize the mobility as a function of temperature, with certain scattering mechanisms dominating the mobility at characteristic temperature regimes. Using theoretical expressions for scattering mechanisms, modeling the mobility can provide insight into the film's bulk properties.

A Hall sample has four evenly spaced Ohmic contacts, where the distance between the contacts is much greater than the thickness of the sample, and the contacts are in a lateral geometry. The sample is placed in a magnetic field, B, perpendicular to the sample normal, a voltage is applied to two opposing contacts, C_1 & C_3, while the Hall voltage is measured across the remaining opposing contacts, C_2 & C_4. Then magnetic

field direction is reversed, -B, and the process is repeated, followed by rotating the contact points, i.e. apply voltage between C_2 & C_4 while measuring the Hall voltage across C_1 & C_3.

Applying a voltage generates carrier flow between the two contacts in a randomized motion with a majority component in the direction of the applied bias according to expressions presented in section 1.3.3 Electronic Properties, J=qnv. The applied magnetic field drives the carriers in cycloidal paths causing a crowding to one side of the sample, courtesy of the Lorentz force. In uncompensated samples, negligible minority carrier concentration,[27] the Hall voltage's polarity indicates carrier type, while the carrier concentration and mobility can be calculated from the magnitude. The spatial steady-state distribution of charge builds the measured Hall voltage as a function of the carriers' deflection due to magnetic field induced cycloidal paths. Expressions for the resistivity tensor can be derived using a force balance about the center of mass of the carriers, defined by the following expression:[28]

Equation 27 - Hall Effect Carrier Equation of Motion

$$qE + q(v_C \times B) - m^* \frac{v}{\tau} = 0$$

In the proceeding expression E is the electric field experienced by the carrier, v_C is the carrier's cyclotron velocity, B is the applied magnetic field, m* is the carrier effective mass, v is the carrier's velocity, and τ is the relaxation time. The relaxation time describes momentum conservation for a scattering mechanism affecting the carrier. Scattering mechanisms characterize the interactions between the lattice and the carriers

that contribute to a reduced drift velocity. The carrier's velocity is determined by the electric field, the magnetic field, and localized scattering in the semiconductor. The velocity tensor's are derived as follows,[28]

Equation 28 - Hall Effect Carrier Velocity Tensors

$$v_x = \frac{q\tau}{m^*}\left[1+\{\omega_c\tau\}^2\right]^{-1}\left(E_x + \{\omega_c\tau\}E_y\right)$$
$$v_y = \frac{q\tau}{m^*}\left[1+\{\omega_c\tau\}^2\right]^{-1}\left(E_y - \{\omega_c\tau\}E_x\right)$$

E_x and E_y are the x and y components of the electric field, ω_C is the cyclotron resonance, q the charge of the carrier (for electrons: q=-e, where e is fundamental charge), τ the relaxation time, and m* is the effective mass. From the velocity expressions' tensor, forms of the resistivity and conductivity tensors can be derived as follows:

Equation 29 - Hall Effect Resistivity Tensors

$$\rho_{xx} = \rho_{yy} = \frac{\sigma_{xx}}{\sigma_{xx}^{\ 2} + \sigma_{yy}^{\ 2}} = \left(\frac{-h}{q^2 i}\right)\left(\omega_C\tau\right)$$
$$\rho_{xy} = -\rho_{yx} = \left(-\omega_C\tau\right)\rho_{xx} = \frac{-\sigma_{xy}}{\sigma_{xx}\rho_{xx}} = \frac{h}{q^2 i}$$

where conductivity tensor, σ, is defined as,[28]

Equation 30 - Hall Effect Conductivity Tensors

$$\sigma_{xx} = \sigma_{yy} = \left(\frac{nq}{B}\right)\left[\frac{\left(\omega_C\tau\right)}{1+\left(\omega_C\tau\right)^2}\right]$$
$$\sigma_{xy} = -\sigma_{yx} = \left(\omega_C\tau\right)\sigma_{xx} = \frac{-\sigma_{xy}}{\sigma_{xx}\rho_{xx}} = \left(\frac{nq}{B}\right) - \frac{\sigma_{xx}}{\left(\omega_C\tau\right)}$$

In the σ_{xy} and ρ_{xy} expressions, the relationship with σ_{xx} and ρ_{xx} through the ($\omega_C\tau$) product holds only for velocity dependent mobilities and electron states that are dominated by the magnetic field. In cases where scattering mechanisms are significantly distorting the quantum states of the carriers, then the center of mass force conservation expression needs to be corrected. From an experimental point of view, the following equation relates the carrier concentration to the measured hall voltage:

Equation 31 - Sheet Carrier Concentration in Hall Setup

$$n_S = \frac{IB}{q|V_H|}$$

where n_s is the carrier concentration, I is the current measured between the applied potential contacts, B is the magnetic field, q is the carrier charge, and V_H is the measured Hall voltage.[8] The mobility, μ, is related to the hall voltage by the hall resistance R_S, seen in the following expression:

Equation 32 - Mobility – Hall Voltage – Sheet Resistance Relationship

$$\mu = \frac{|V_H|}{R_S IB} = \frac{1}{qn_S R_S}$$

The software provided with the Lakeshore cryogenic setup rotates the contact points and mismatches contact configurations to measure the average transport properties of the films in the Van der Pauw scheme. The Hall software calculated the carrier concentration and mobility values as a function of temperature down to 10K. Agreeing with Fermi theory, the carrier concentration decreases as temperature decreases, indicating temperature-induced deactivation of thermally excited carriers, freeze-out. At

lower temperatures, the mobility increases as electron – electron and electron – lattice collisions become less predominate due to lower carrier populations, though ionic interactions have a longer affective range due to lowered screening.[1] Figure 4 - Carrier Concentration vs. Temperature shows a representative sample's carrier concentration response to temperature, while Figure 5 - Mobility vs. Temperature demonstrates the mobilities response to temperature.

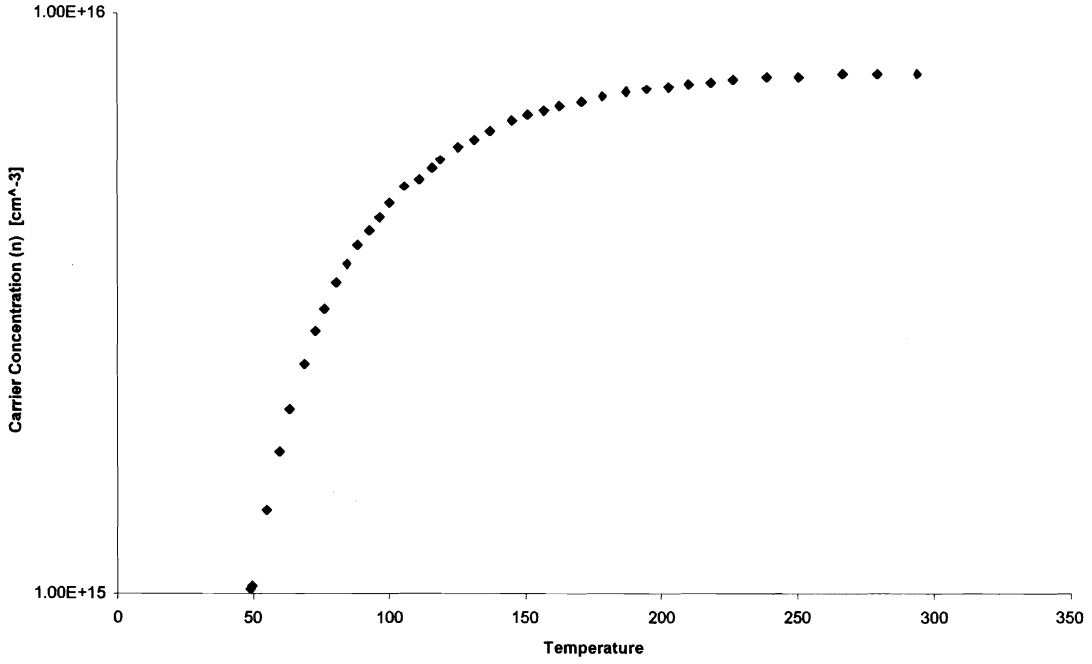

Figure 4 - Carrier Concentration vs. Temperature

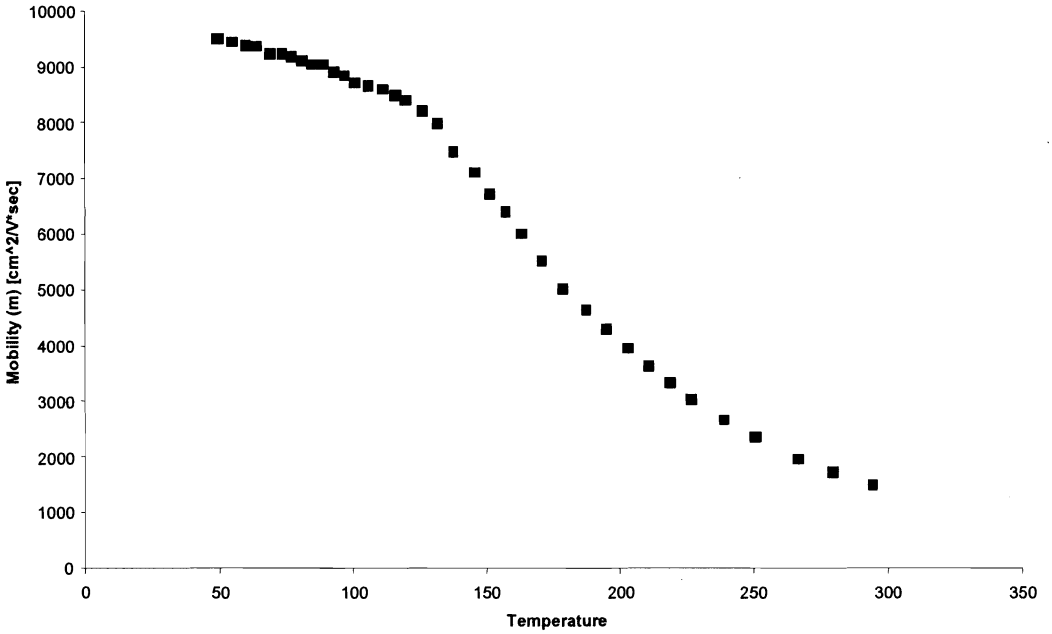

Figure 5 - Mobility vs. Temperature

The results presented here show that HVPE films have a high mobility and this particular film was n-type. The carrier concentration decreases with decreasing temperature and the mobility has a peak value of 9516.8 $cm^2/V \cdot sec$ at approximately 49.8 K and a room temperature value of 1498.4 $cm^2/V \cdot sec$. These values are larger than some presented in literature, indicating a better Ohmic contact and / or thin film of GaN.[29] Figure 6 - Experimental and Theoretical Mobility vs. Temperature compares the theoretical mobility expressions to the measured Hall data.

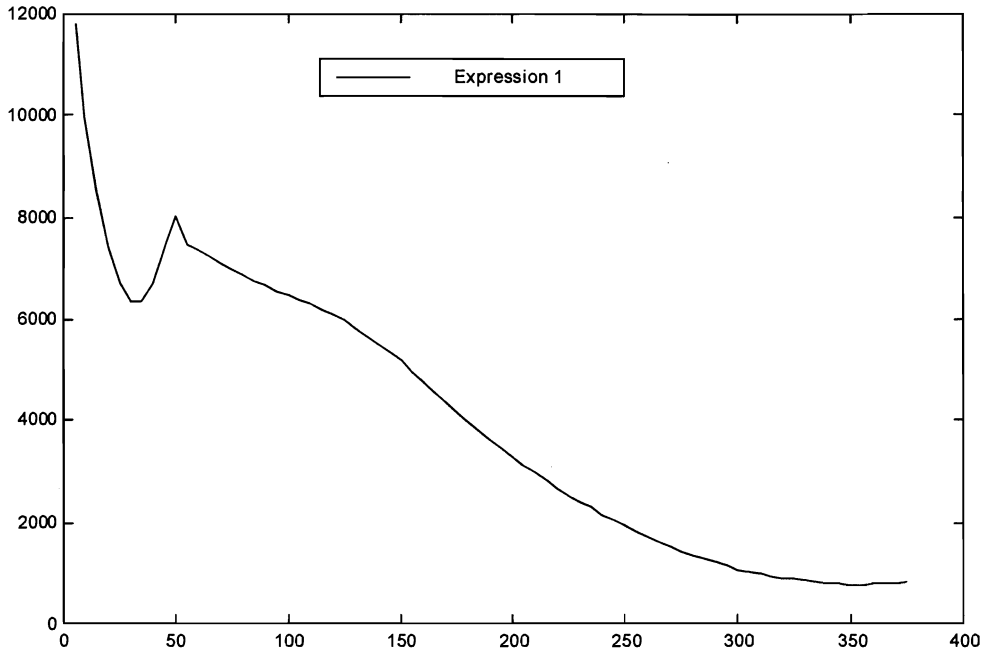

Figure 6 - Experimental and Theoretical Mobility vs. Temperature

For heterostructures the effective mobility can be much higher than in a bulk material, as demonstrated by Manfra et al., reported mobility figures of 75,000 at 4.2 K for a 2-DEG density of 1.2×10^{12} cm^{-2}.[12] The same report identified the calculated maximum mobility for alloy scattering in an $Al_{0.05}Ga_{0.95}N/GaN$ heterostructure, with a 2-DEG density of 1.5×10^{12} cm^{-2} and mobility of 80,000 $cm^2/V\cdot s$.

2.2.1.1 Mobility and Scattering Mechanisms

Carrier scattering is dependent on the crystal type, constituent elements, concentration of defects, film temperature, and layer structure. Liouville equations

describe charge distribution in a solid; however, Boltzmann found that the zeroth order term was sufficient in scattering mechanisms, thereby reducing the complexity of carrier distribution.[6] The Boltzmann equation is a distribution function represented in phase space, with generalized coordinates of the (x, y, z) spatial components and the (k_x, k_y, k_z) momentum components, constructed from the collection of Bloch functions related to the specific scattering event. To further the concept of carrier interactions with the lattice, Boltzmann equation's Taylor series is evaluated at steady state, assuming there is no change in the charge distribution of the crystal and the system has no memory.[5] Applying this assumption to the Taylor series leaves three terms: a change in the distribution versus time, movement in momentum and real space.

A collision term specific to the scattering mechanism can be introduced as a disturbance to the steady state distribution function, establishing a relationship between the collision integral and the subsequent changes in momentum and real space. The collision integral is proportional to a term that contains the lattice disturbance potential and the wave functions before and after the scattering event. The wave functions relate the momentum and spatial vectors of the carrier to the lattice deformations, or phonons. Each scattering mechanism is a lattice perturbation that interacts with an electron in space and momentum. The scattering potential of the lattice's free energy causes the shift in phase space of the carrier's wave functions, which can be elastic / conservative or inelastic / non-conservative. The mechanisms exhibiting elastic lattice interactions are acoustic, piezoelectric, impurity and alloy scattering. The inelastic scattering mechanisms are the optical phonon and intervalley scattering.

The relaxation time approximation relates the carriers' momentum relaxation time to the drift velocity. The amount of time it requires the electron to return to a randomized path, alternatively viewed as the amount of time it takes for the gained carrier momentum to disperse, is termed the momentum relaxation time and is specific for each mechanism. A ratio that expresses the percentage of energy lost in the collision is defined by dividing the mean free time in-between collisions into the energy relaxation time taken from the Boltzmann equation. For acoustic phonons at room temperature, approximately 0.1% energy is lost to the phonon- carrier collision and for optical phonons at room temperature the ratio is on the order of 1.[6]

A purely elastic process, ionized impurity scattering is the dominant scattering mechanism at near absolute zero temperatures.[1] It is derived classically from the Rutherford atomic scattering model where a particle is deflected in a hyperbola by the nucleus. The ionized lattice atoms deflect or attract the carriers, disturbing them from their initial, steady-state, phase space trajectory. Numerical expressions can be derived classically or from a quantum mechanical point of view, though both models need a correction factor to account for the screening of other electrons in the sub-valence shells of the ionized impurity atom. Ionized Impurity Scattering is one of the two most important scattering mechanisms. It is necessary to model ionized impurity scattering in every application.

Neutral impurities are atoms that have bonded into the crystal lattice and do not exhibit columbic interactions on carriers. Rutherford scattering effects are not associated with neutral atom carrier interactions. Neutral impurity scattering is relatively

unimportant at room temperatures and negligible at liquid nitrogen temperatures.[7] Neutral impurity scattering accounts for elastic carrier collisions with stable lattice sites.

Acoustic phonons are low frequency oscillations of the crystalline structure.[5] The individual lattice atoms are shifted from their equilibrium positions as the acoustic wave traverses through the crystal. A localized lattice potential results which resists the displacement imparted by the acoustic wave. This potential is used in the collision integral of the Boltzmann transport equation to describe the statistical ensemble of carrier wave permutations that can result from the localized potential. In 1950, Bardeen & Shockley published a formulation for acoustic phonon scattering.[7] The force exerted on the lattice by the acoustic waves also causes a proportional shift in the energy band diagrams. Acoustic scattering is relatively unimportant in most applications, except at low temperatures. There are some high power applications where a significant amount of acoustic phonons could be introduced into the bulk material and some devices utilize the production / absorption of phonons.

Piezoelectric scattering is present in noncentrosymmetric crystals where there is an applied external stress or strain caused by mismatched heterojunctions.[30] In addition to internal strain, external compression on the semiconductor, high-pressure environments, and applications where the device has an applied or internal force causes the piezoelectric scattering rate to increase. As a crystal is compressed from the equilibrium atomic spacing, a restoring potential arises that resists the compressing displacement. The piezoelectric restorative potential-carrier interaction affects the wave functions by altering their trajectories in phase space. This potential is incorporated in

the Boltzmann equation through the collision integral. In the piezoelectric effect, the strain creates a restoring potential that will diminish when the lattice spacing returns to equilibrium.[5]

Polar optical phonon scattering is the dominant scattering mechanism at room temperature, particularly in GaN. There can be a significant optical phonon population in a semiconductor, especially when dealing with optical detection and generation applications. The optical phonons deform the local crystal's electronic structure by introducing vibrations in the conduction and valance bands that can significantly interfere with the transport of carriers through the lattice. As the temperature decreases, the optical branches decrease in activity and the electron generation rate due to band gap excitation becomes negligible. The optical phonon spectrum is inarguably coupled to the defect microstructure of a given sample.

It would be impossible to state the effects of intra-valley polar-optical phonon scattering given just the mobility figure due to the simultaneity of the competing scattering mechanisms. Accordingly, a low drift mobility figure would divulge no details as to the nature of the scattering mechanisms that are responsible at a given temperature. These situations dictate further insight and formulation into the nature of semiconductors, their electronic and optical structures, and growth techniques to optimize the mobility to its theoretical maximum. Simulations establish the theoretical limits and provide a comparative basis for samples.

2.2.2 Current - Voltage Measurements

When a potential is applied a material junction, the potential distribution in the material will influence the motion of the carriers under the constraints of the energetics imposed by the physical system. In conditions where there is a non-uniform distribution of semiconductor material, such as a p-n junction, the current density also has a diffusion component that is added with the drift expressions presented below. The highest impedance will limit the semiconductor – contact system's properties. In the case of an Ohmic contact, the carriers move relatively unimpeded through the metal semiconductor junction with the resistivity of the semiconductor ideally determining the current flow. On the other hand, the carrier motion in a Schottky diode is impeded by the presence of a barrier induced by the energy discontinuity present at the metal semiconductor junction, thereby creating the rectifying behavior. In a specific Schottky diode, the current density is a function of the dominant conduction mechanism attributable to some physical electron transport process. Conduction fallacies are a result of imperfections in the growth of the semiconductor or fabrication devices, unique and mostly unwanted conduction behaviors may arise.

The Schottky contacts investigated at MMDL were of two types: vertical or lateral geometry. In the lateral geometry, dislocations play an increased role –as they limit the mobility in the in-plane direction. In the vertical case, the reduced resistance out of plane due to the threading dislocations increases the mobility.[31] Expressions can relate the vertical Schottky contact saturation current to the out of plane mobility when

characterized as a function of temperature. Except for the Samsung HVPE Schottky diodes, all of the devices in this study were fabricated in a lateral geometry.

In the unlikely case the current flow is mediated by another aspect of the Ohmic, GaN, Schottky diode system than the barrier at the Schottky – GaN interface, formulations involving the rate limiting step would be necessary to explain anomalous conduction. A subset of the current mechanisms used in curve fitting of current voltage responses on Schottky diodes will be presented succinctly.

2.2.2.1 Thermionic Emission

For properly formed Schottky devices on high quality, low carrier concentration, material this is the expected means of current transport. Thermionic emission characterizes the transport of charge over a potential barrier created by the metal-semiconductor interface. As the cathode voltage of the device is increased, the current will begin to respond in an exponential relationship with the applied voltage, according to the following expression.

Equation 33 - Thermionic Emission Mechanism

$$J_{te}(V,T) = J_{teo}\left[\exp\left(\frac{qV}{kT}\right)-1\right]$$

Equation 34 - Thermionic Emission Saturation Term

$$J_{teo}(T,\phi_B,\Delta\phi) = A^{*}T^{2}\exp\left[\frac{-q(\phi_B-\Delta\phi)}{kT}\right]$$

In the above expressions, J_{te} represents the thermionic emission current density that would be compared to experimental data, J_{te0} represents the thermionic saturation current, V is the applied potential to the device, k is the Boltzmann constant, q is the fundamental charge, T is the temperature, A^* is the effective Richardson's constant, ϕ_B is the Schottky barrier height, and $\Delta\phi$ is the image force lowering term. The voltage term in the thermionic case needs to be replaced with $(V\text{-}IR_S)$ to account for the series resistance of the material. At high voltages, the series resistance, from the mobility limiting effects of the bulk, causes the response to saturate and the response becomes linear. The fundamental charge is generally a correction for units and can be neglected in numerical calculations, more importantly ensure exponential / trigonometric operations are operating on a unitless number. The saturation current is termed J_{te0} and is primarily a function of temperature for a given device. Fitting parameters for curve fitting using thermionic field emission are the saturation current, J_{te0}, and the ideality factor, n. Although theoretical expressions detail the fundamental origins of the saturation current, this parameter is used as a fitting parameter, therefore a prior knowledge of the interdependencies are not necessary, reference 1 can provide further details.

Image force lowering characterizes the effects of free carriers screening the potential discontinuity of the semiconductor metal interface, thereby lowering the effective potential of the Schottky barrier according to the following equation:

Equation 35 - Image Force Lowering Term

$$\Delta\phi = \sqrt{\frac{qE}{4\pi\varepsilon_s}} \quad [V]$$

In the proceeding equation, E is the electric field in the semiconductor underneath the Schottky contact and ε_s is the semiconductor dielectric in units of F/cm^2. Image force lowering can significantly increase the conduction volume of carriers for a given voltage and temperature. If image force lowering is a significant contribution then thermionic field emission may need to be looked into as another candidate for a conduction mechanism.

The effective Richardson's constant is a measure of the effective mass of the material. The following expression describes the relationship between the effective mass and the effective Richardson's constant.

Equation 36 - Richardson's and Effective Richardson's Constant

$$Richardson's: A = \frac{4\pi q k^2 m_0}{h^3}$$

$$Effective\ Richardson's: \quad A^* = A\left(\frac{m^*}{m_0}\right)$$

In the above equations, q is the fundamental charge, k is Boltzmann's constant, m_0 is the carrier free mass, h is Plank's Constant, and m^* is the semiconductor's effective mass.[1] Plotting the saturation current density as a function of temperature can reveal the Richardson's constant and the barrier height / image force term. The intercept is a function of the Richardson's constant if the x and y-axis have not been corrected for in an Arrehenius plot of the saturation current. If the axis are corrected by 1/T and $\ln(J_0/T^2)$, then the Arrehenius plot takes the form of the traditional Richardson's plot. As an alternative method for determining the Richardson's constant, a modified Norde plot can

be used.[32] The Norde method relies on finding the inflection point with respect to a specialized function in the turn-on response of the Schottky device.

Equation 37 - Norde Function

$$F(V) = \frac{qV}{2kT} - \ln\left[\frac{I}{T^2}\right]$$

To correctly implement the Norde method a matrix is formed using the Norde equation for each point of the forward responses of the Schottky devices as a function of temperature. Finding the minimum point of the Norde function for each temperature curve defines the inflection point; the corresponding voltage and current are used in axis functions to create the modified Norde plot. The axis assume the form of the following expressions in the modified Norde plot:

Equation 38 - Norde Axis Definitions

$$y-axis: \quad 2F1_m + (2-n)\ln\left(\frac{I_m}{T^2}\right)$$

$$x-axis: \quad \frac{q}{kT}$$

The variable $F1_m$ is the minimum value in the forward Norde expressions, I_m is the corresponding minimum current, T is the temperature in Kelvin, k is the Boltzmann constant, and q is the fundamental charge. From the intercept the Richardson's constant can be determined, and the barrier height from the slope. The Norde method is only useful resolving properties from devices exhibiting thermionic emission; other current mechanisms will require alternate methods.

2.2.2.2 Thermionic Field Emission and Field Emission

Thermionic emission occurs in Schottky devices when the carrier concentration is low enough that the depletion depth under the contact prevents tunneling behaviors. Thermionic-field emission is a combination of thermionic emission over the barrier with a tunneling component, exhibiting depletion depths on the order of 10-100 nm. A depletion depth of less than 10 nm is representative of field emission. If there is a conductive interfacial layer, or the carrier density is extremely high, the contact behaves more like a parallel combination of resistors and a diode, rather than the pure thermionic diode response of a well-formed Schottky contact. Field emission can be the result of metal induced gap states (MIG's), processing related surface states, high doping concentrations, or defective material. Depletion depths greater than 100 nm are generally pure thermionic emission. The major difference between thermionic, thermionic field and field emission is the contribution of a tunneling component in the measured current flow through the contact with respect to the applied potential and / or the field beneath, and around, the Schottky contact.

Thermionic field emission is associated with moderately defective or doped GaN films. Carrier concentrations as low as 10^{17} cm^{-3} in the bulk can demonstrate thermionic field emission in the best case. In thermionic emission there is a contribution to the current flow from the applied potential and an energy term, E_0, that characterizes the transparency of the contact with respect to carrier transport, i.e. tunneling. The following expression is for thermionic field emission.

Equation 39 - Thermionic Field Emission

$$J_{tfe} = J_{tfe0}\left[\exp\{\frac{qV}{kT} - \frac{qV}{E_0}\} - 1\right]$$

In this expression, J_{tfe0} is the thermionic field emission saturation current, k is Boltzmann's constant, T is the device temperature, V is the applied potential, q is the fundamental charge constant, and E_0 is the energy transparency term, defined by the following expression.

Equation 40 - Characteristic Energy

$$E_0 = E_{00}\coth\left(\frac{E_{00}}{k\,T}\right)$$

The E_{00} term is a characterization of the field starting at the metal semiconductor interface and extending under the contact, defined by the following expression.

Equation 41 - Energy Transparency Term

$$E_{00} = \frac{q\hbar}{2}\sqrt{\frac{N_D}{\varepsilon_s m^*}}$$

In this expression $\hbar$ is the modified Planck's constant, $\hbar = \frac{h}{2\pi}$, N_D is the donor concentration of the majority carrier, ε_S is the semiconductor dielectric and m^* is the effective mass of the majority carrier. Using curve fitting techniques the energy transparency term was selected as a tuning parameter, and values ranged from several electron volts to greater than 20 eV, at low and room temperatures respectively. Presented in Figure 7 - TFE Conduction as a function of E_{00}, is the theoretical TFE Current versus Voltage for various values of E_{00}.

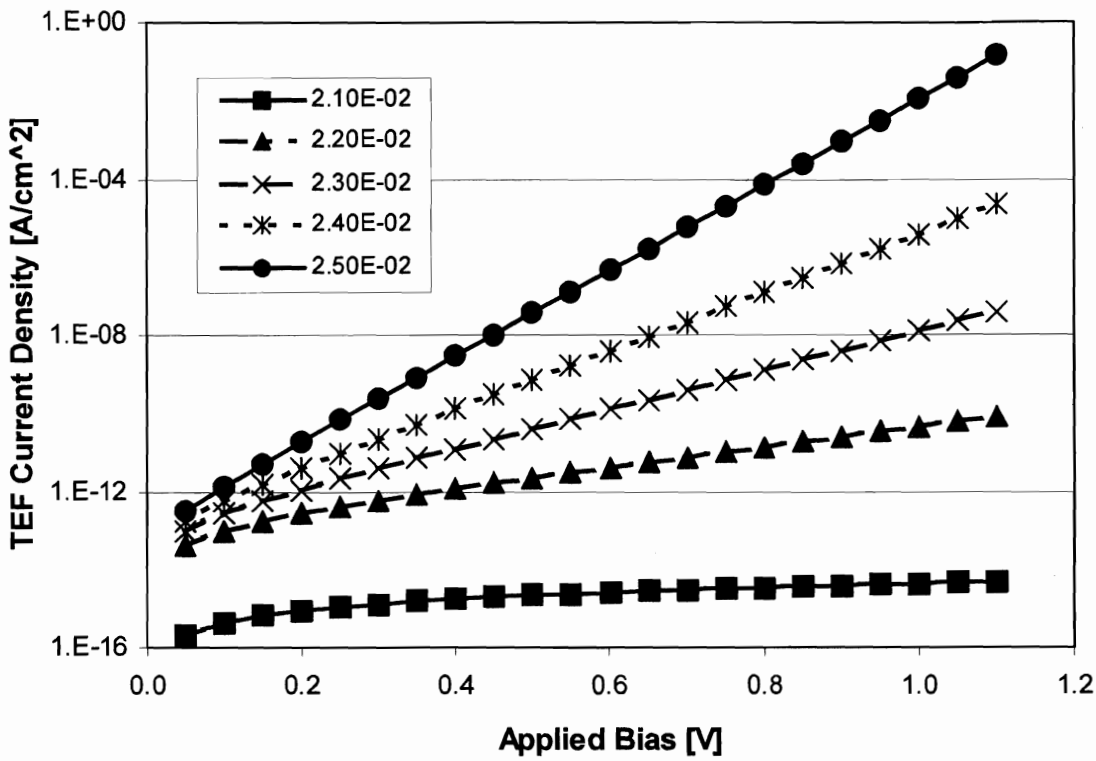

Figure 7 - TFE Conduction as a function of E_{00}

Note the distinct curvature at low biases associated with the tunneling component of the current response. At higher biases, the current density becomes an exponential response associated with thermionic emission.

If the carrier concentration is greater than 10^{18} cm^{-3} then thermionic field emission yields to field emission, where only the field under the contact determines the current response. In cases of field emission, the transparency term dominates the conduction mechanism and the temperature dependent voltage term can be neglected. In highly defective material, field emission is the predominantly observed current mechanism, as

the depletion depth under the contact is increasingly smaller and the high density of carriers can tunnel through the Schottky barrier.

Equation 42 - Field Emission

$$J_{fe} = J_{fe0}\left[\exp\{\frac{qV}{E_0}\} - 1\right]$$

The saturation term J_{fe0} is a fitting parameter, details on the fundamental dependencies can be found in ref. 1.

2.2.2.3 Frenkel-Poole Conduction

Poole-Frenkel conduction involves detrapping and incomplete ionization of defect or donor states near the conduction band edge. The application of a field to the sample causes a barrier lowering to the trap's Columbic potential well. Poole-Frenkel conduction has been reported in variety of materials from amorphous glassy materials to diamond and TiO films. Traps that participate in Poole-Frenkel conduction must be neutral when filled and charged when empty. Additionally, if a trap were neutral when occupied and charged when unoccupied, then there would be a small or $\xi^{-3/2}$ dependency of the capture process.[33] The Poole-Frenkel expression for the current density, considering emission of carriers in both directions out of the trap, can be written as:

Equation 43 - Complex Frenkel-Poole Conduction Mechanism

$$J_{FP} = A'(T)\exp\left[\frac{q\phi_i}{mkT}\right](\alpha\cosh\alpha - \sinh\alpha), \qquad where \quad \alpha = \frac{q\beta E^{1/2}}{kT} \;\&\; \beta = \left(\frac{q}{\pi\varepsilon_s}\right)^{1/2}$$

A'(T) is some function of temperature, ϕ_i is the donor binding energy at zero field, β is a term characterizing the potential lowering due to the Poole-Frenkel effect, and ε_s is the high frequency dielectric of the material. The variable m in the exponential factor containing the ionization term ϕ_i scales for two cases. The first case, corresponding to m=2, represents a high density of acceptor sites as compared to donor sites and conduction band electrons, while m=1 is used for a large concentration of donor and acceptor sites as compared to conduction electrons. Curve fitting with the above expression would be performed using two expressions for each value of m, and tuning parameters for the saturation terms, A(T'), and α.

A reduced form of the Poole-Frenkel expression can be obtained as follows:[8]

Equation 44 - Simple Frenkel-Poole Conduction Mechanism

$$J_{FP} = J_{FPO} \exp\left(\frac{\beta_{FP} E^{1/2}}{kT}\right)$$

Equation 45 - Expression for β

$$\beta_{FP} = \left(\frac{q^3}{\pi\varepsilon\varepsilon_o}\right)^{1/2} \quad \left[\frac{eV\ cm^{1/2}}{V^{1/2}}\right]$$

Here J_0 is the saturation term, β_{PF} is the exponential slope factor that characterizes the trap dynamics, q is the fundamental charge, ε_0 is the free space dielectric constant, and ε is the semiconductor dielectric. The tuning parameters are the saturation term, J_{FP0}, and the exponential slope, β_{FP}. A typical Poole-Frenkel current-voltage response generated

using the simplified expression is presented as Figure 8 - Frenkel-Poole Current Voltage Relationship.

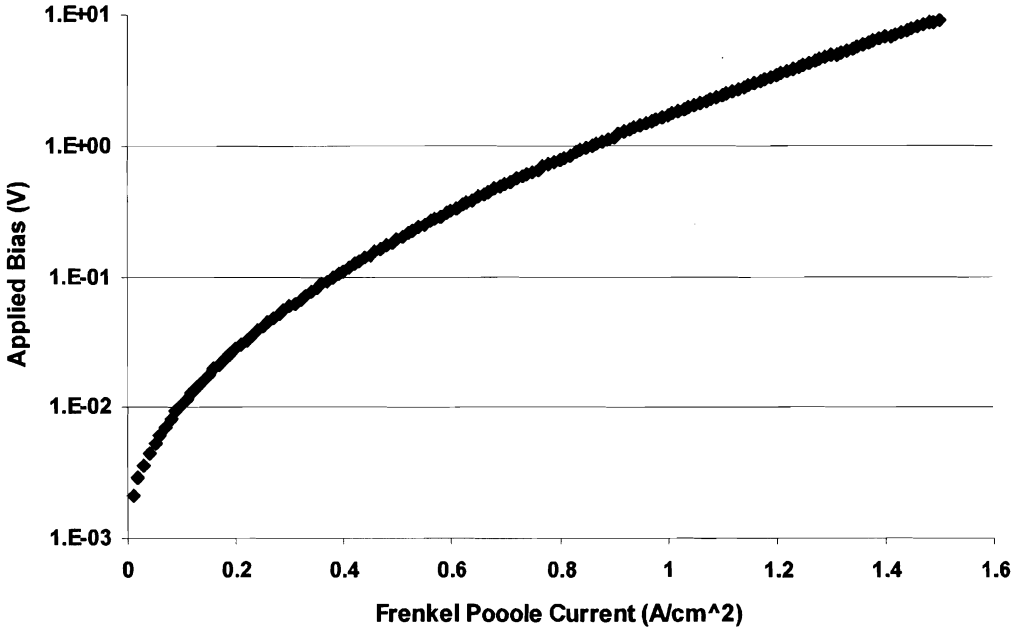

Figure 8 - Frenkel-Poole Current Voltage Relationship

If one is interested in the Poole effect the α term can be replaced by (qsE)/(kT), where 2s is the distance between defect centers. Alternatively, the Schottky effect is represented by multiplying the β term by 4. The major difference in the Schottky effect and the Poole-Frenkel effect is the image charge at a Schottky interface on the metal side is mobile, where as the Poole-Frenkel charge is fixed due to bound nature of the trap. The conductivity of samples exhibiting Poole-Frenkel conduction should also follow an exponential function of the field identical to the reduced form. All of the above

permutations were compared to the experimental current-voltage data with the saturation term and at least one, depending on the mechanism, exponential term as tuning parameters.

2.2.2.4 Hopping Conductivity

In highly defective films, the density of inter-bandgap defects can be exceedingly high, thereby forming a situation in which networks of preferential sites have a significant spatial and energetic overlap. In this case, electrons do not have to enter the conduction band to travel through the semiconductor; a lower energy parallel conduction path exists. Percolation theory was used to describe the earliest forms of hopping conductivity based on rate limiting paths in the defect structure. Simplified exponential relationships assume the following form,

Equation 46 - Hopping Conduction Mechanism

$$J_{HP} = J_O \exp \left[\frac{qaCE}{2kT} \left(\frac{T}{T_O} \right)^{1/(1+n)} \right]$$

where C is a constant on the order of 18, q is the fundamental charge, a is the characteristic length, kT is the thermal energy, and n is the dimension of hopping. The signature of Hopping conductivity is the power dependency in the $(T_0/T)^{1/(n+1)}$ term, where n denotes the dimension in which hopping will occur. Fractional values of n are indicative of phonon assisted hopping conductivity. The parameter T_0 is the characteristic temperature, it is a measure of the defect structure and free energy, and is given by the following expression for a multi-particle hop,[34]

Equation 47 - Multi-particle Hop Characteristic Temperature

$$T_0 = E_{ST}\left(\frac{l}{a}\right)^{1/4} \qquad \text{where, } E_{ST} = \frac{q^2}{\varepsilon a}$$

E_{ST} is the bare single particle excitation energy, l is the distance from trap to trap, a is the localization length of a trapping potential, and ε is the high frequency dielectric constant. Figure 9 - Hopping Conductivity vs. Applied Potential shows the Hopping Conductivity expression presented above as a function of applied bias.

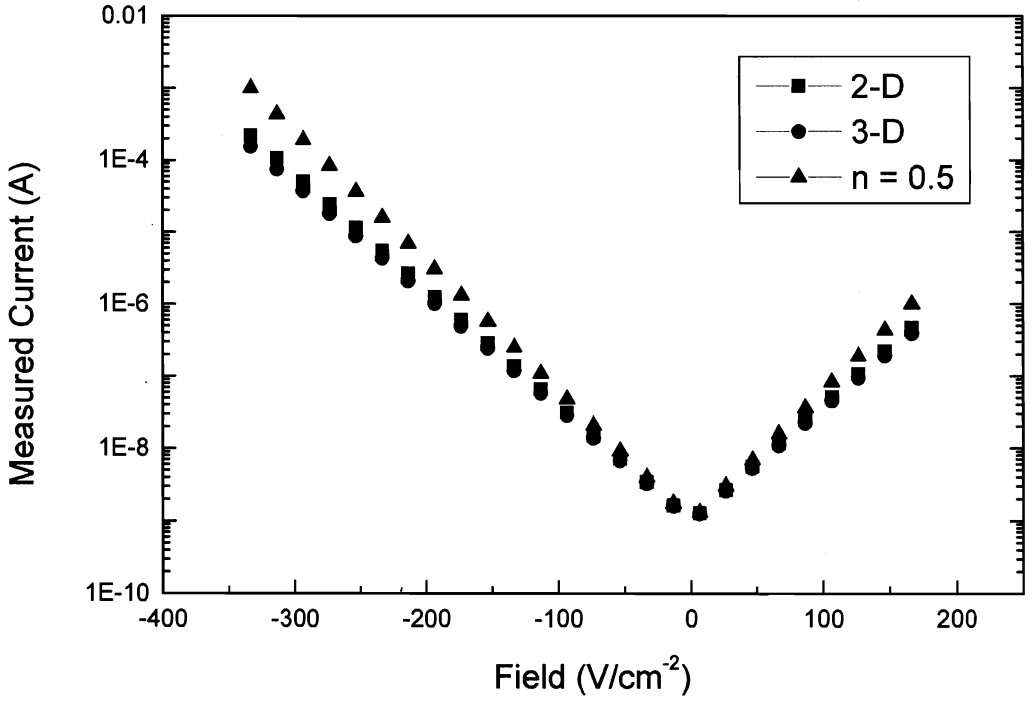

Figure 9 - Hopping Conductivity vs. Applied Potential

For curve fitting, tuning parameters were selected as the saturation term and a factor representing the product of C and a. A separate expression was compared to the experimental data for each dimension of Hopping, n = 1, 2, and 3, considered.

2.2.3 Capacitance-Voltage Measurements

Every material has an intrinsic capacitance and inductance. In a Schottky contact, the energy disparity about the interface introduces a depletion depth under the contact according to the following relationship:[8]

Equation 48 - Capacitance & Depletion Depth Relationship

$$\frac{C}{A} = \frac{W}{q\varepsilon_s}$$

Above, W is the depletion depth, ε_S is the dielectric constant, q is the fundamental charge, A is the contact area, and V is the applied potential. Equation 48 - Capacitance & Depletion Depth Relationship provides the means for relating an applied bias to the depletion depth of a Schottky contact. The void of carriers under the contact introduces a contact capacitance that can be modulated with the depletion depth by applying negative biases. The capacitance voltage relationship is given following:[8]

Equation 49 - Capacitance Voltage Relationship

$$\frac{1}{C^2} = \frac{2\left(V_{Built-in} - \frac{kT}{q} - V_{applied}\right)}{A^2 q N_d \varepsilon_S}$$

In the above expression, $V_{Built\text{-}in}$ is the flat band voltage, k is the Boltzmann constant, T is the temperature, q is the fundamental charge, A is the contact area, N_d is the carrier concentration, and ε_S is the semiconductor dielectric. For Schottky diodes, the capacitance will delve information about doping concentration and depletion depth with response to an applied AC voltage offset by a negative DC bias. Care must be taken in performing the capacitance as defects can complicate the frequency response of the material. If a defect is slower than the probing AC wave then the defect should stay in a filled state and contribute little to the measurement. If the defect has a higher charge / discharge frequency than the probing AC wave then intermittent discharging will add noise to the measurement.

By plotting the inverse capacitance squared versus the applied potential, one can determine the intrinsic carrier concentration as a function of the slope and the built-in voltage as a function of the x-axis intercept. The barrier height can be calculated from the built-in voltage of the contact as follows:

Equation 50 - Capacitance Barrier Height Definition

$$\phi_{CV} = q\left(V_{Built-In} + V_n\right)$$

The term V_n is the thermal voltage, defined by:

Equation 51 - Thermal Voltage Definition

$$V_n = \left(\frac{kT}{q}\right)\ln\left(\frac{N_C}{N_D}\right) = \frac{E_C - E_F}{q}$$

where k is the Boltzmann constant, T is the temperature, q is the fundamental charge, N_C is the conduction band density of states, and N_D is the density of states. The term conduction band density of states is defined by the following expression:

Equation 52 - Conduction Band Density of States

$$N_C = 2\left(\frac{2\pi m_n^* kT}{h^2}\right)^{3/2}$$

Capacitance-voltage measurements are used to verify current-voltage characterizations, and provide insight into physical parameters.

2.2.4 Deep Level Transient Spectroscopy (DLTS)

Determining the source of an electrical anomaly ultimately relies on several techniques. Deep level transient spectroscopy (DLTS) is an electrical technique used to determine the nature and character of bulk mid-gap defects. It is similar to C-V profiling, though the measurements are more rigorously designed in order to identify defects either as a response to charge / discharge times or probing AC frequency. Combining DLTS measurements with irradiation techniques is useful in determining the nature of defect levels in semiconductors. Electron beam irradiation at an energy of 1 MeV is cited as introducing a defect at E_C-E_t = 0.18 eV.[35] Fang *et al.* noticed no defect or doping related effects for 1 MeV doses under 1×10^{15} cm^{-2}. Helium and proton bombardment were examined by Goodman *et al.*,[36] while Ar+ bombardment was explored by Polyakov *et al.*[37] CW Wang *et al.*, investigated the effects of neutron irradiation on Au-sputter deposited Schottky contacts. Neutron irradiation was capable of suppressing the N-

vacancy related defect levels and improved quenching of the yellow luminescence band.[38]

In reality, both surface and bulk effects contribute to the difficulties in obtaining high quality devices on n-type GaN. In studying bulk defects in MOCVD grown n-type GaN, Hierro *et al.* identified several traps with deep level transient spectroscopy (DLTS) residing at 1.35, 2.64 and 3.22 eV in concentrations of $10^{14} - 10^{16}$ cm^{-3}. The 1.35 eV trap is believed to be a result of carbon contamination and the 2.57 – 2.64 eV is attributed to a minority hole trap.[39] Other bulk defect levels identified in GaN layers reside at 0.23 – 0.27, [40] 0.5,[41] 0.53-0.56,[40] 0.79-0.82,[40] 0.81,[42] 1.05, [41] and 1.07 eV,[40] with gallium vacancies identified as causing the 0.8 eV level at a density of 5×10^{15} cm^{-3} and cross section of 2×10^{-14} cm^{-2}.[41, 42]

In order to realize the full range of microelectronic devices donor and acceptor type material must be controllably produced. Acceptor, p-type, GaN growth is problematic for good electrical characteristics because a good dopant has yet to be identified. Films reported by Nguyen *et al.*, demonstrate Mg-related recombination in acceptor levels at temperatures below 230 K and series resistance dominated behavior above 230 K.[43] Nakano *et al.* have attentively assigned the Mg related shallow impurity at ~ 112 meV.[44] The position of the defect can be a strong function of the material deposition and post processing conditions. Deep defect time constants, in Mg doped GaN, have been measured to as long as $8.3*10^3$ seconds by Shiojimia *et al.*[45] Magnesium doping can be problematic as there is competition between impurity and dopant behavior.[46] A DLTS study of p^i GaN revealed four trap levels located at E_C-E_T = 0.23-

0.27, 0.56, 0.82, 1.07 eV.[47] The deep level defects identified at energies 0.56 eV and 0.82 eV are suspected to be related to extended defects.

2.3 Microscopy Techniques

Surface properties of semiconductors are as important to device characteristics as the bulk properties. On crystalline surfaces, states emerge in the energy structure related to structural bonds. Only a few characterization techniques, such as X-ray photoemission spectroscopy (XPS) transmission electron microscopy (TEM), and scanning tunneling microscopy (STM), can resolve the small aspect ratios required for surface investigations.[48] The defect structure of films is studied with hot acid and base preparations to etch selective portions of the sample and examine the specimen with AFM. Quality control of fabrication processes is also a primary use of surface microscopy techniques, mainly scanning electron microscopy (SEM) and AFM. In this study, atomic force microscopy techniques were used to investigate the surface defect structure with current spectroscopy and conductive atomic force microscopy (CAFM).

2.3.1 Scanning Electron Microscopy (SEM)

Scanning electron microscopy has been the standard surface microscopy technique for many years. Images of the surface can be obtained at magnifications above 100,000 times. The technique relies on bombarding the surface with a collimated beam of electrons, utilizing the de Broglie wavelength of the energetic particle to image a sample. The electrons are emitted from a filament using accelerating electrodes, which also specify the electron energy and density. An accelerated divergent beam of electrons

is emitted towards the sample through a column of beam collimating and focusing electromagnetic lenses. Two types of detectors, primary and secondary, collect the electrons emitted from collisions with the surface. The primary detector collects electrons primarily involved in elastic collisions, emitted at normal angles to the surface, while the secondary lens collects electrons at wider angles of incidence and wider distribution of energies due to the inelastic nature of their collisions. An image of the surface is constructed from the detectors' signals by a computer interface. The major aspects of obtaining the best SEM images are the working distance, distance between the beam source and sample, the beam energy, beam collimation, and chamber vacuum pressure. It is essential to have a conductive sample as charging renders imaging impossible and could damaged the sample if the beam energy and, or, electron density is too high. Charging also limits the abilities of SEM to resolve insulative materials like semiconductors and materials with oxide coatings. There are a number of techniques, such as EDX and Auger Spectroscopy, that utilize the EM setup to obtain additional data, see reference 48.

2.3.2 Transmission Electron Microscopy (TEM)

Akin to scanning electron microscopy, transmission electron microscopy (TEM) uses a collimated beam of electrons to image a thin cross section of a sample. A major difference is the electrons forming the image pass through the sample and the image is obtained on the side of the sample opposing the electron beam. The transmission length of electrons, for a given imaging energy, in the given medium determines the maximum thickness of the sample. TEM is the premiere microscopy technique for information and

scale of magnification, though sample preparation is tedious and limits the technique's implementation. Transmission electron diffraction (TED) is performed in the same apparatus, though it uses a different configuration of lenses behind the sample to obtain a diffraction pattern rather than an image, which is possible due to the wave-particle duality of electrons. The resolution of TEM is unrivaled by other microscopy techniques providing the best information about structural defects' density and physiology. Zuzana Lintel-Weber provided the TEM data presented in this study.

2.3.3 Atomic Force Microscopy

The main advantage to atomic force microscopy is its ability to image nanoscale features in atmospheric conditions. Using a cantilever and a laser beam deflection scheme, the atomic structure of a sample's surface can be probed in two manners, either contact mode or tapping mode. In contact mode, the cantilever is dragged along the surface with a designated force, dictated by the deflection voltage. As the cantilever deflects from the physical interaction with surface structures, the laser beam is reflected off the topside of the cantilever and the deflections are registered in a detector array. Tapping mode differentiates from contact mode because the cantilever does not rely on structural deflections but rather the electrostatic interaction between the oscillating cantilever and the surface. Every cantilever has a unique resonance frequency because of the material and geometry. Interactions of the atomic structure of the surface with the cantilever's sharp tip will cause a shift in the resonance frequency and the amount of force necessary to maintain a given cantilever amplitude and correction to the impedance phase shift in the load coupling. If the driving force maintains the frequency, these

interactions result in a change in the nature of the deflected optical signal. In either mode, the software converts the electrical signals from the laser detector and the AFM head into an image of the surface and any other variables measured, such as phase shifts or tip deflection.

Atomic force microscopy (AFM) provides insight into the morphology of a films surface, and extensions can allow coupling of morphological features with specific signals, i.e. increased conductivity. There are numerous extensions to the standard tapping and contact mode AFM techniques: Magnetic Force Microscopy (MFM), Electric Force Microscopy (EFM), Conductive AFM (C-AFM), Scanning Tunneling Microscopy (STM), and Torrosional Force Microscopy (TFM), are a few of the extensions commercially available for the Dimension 3100. In essence, all of the extensions involve investigating a particular aspect of the material by isolating the force of interest on the tip. Electric Force Microscopy, a tapping mode extension, is used to profile the relative change in the electric potential of a material's surface. Care must be taken when interpreting results from particular techniques, such as MFM, as the effects of the electric potential distribution need to also be considered to ensure the validity of the data.

All samples investigated in this study by AFM techniques used a Dimension 3100 AFM. For techniques involving a metallized cantilever, numerous metallizations and styles were examined. For CAFM and EFM, a MIKROMESH NSC14 Pt cantilever was selected for measurements due to the high detail and durability. The NSC14 has a length of 125 μm a width of 35 μm and an average thickness of 2 μm. The characteristic

frequency of the NSC14 averages 160 kHz, with a minimum force of 1.8 N/m, maximum force of 12.5 N/m, and average force of 5 N/m. Other cantilevers investigated included CrAu metallization and the NSC 16, NSC 18, and CSC 17. The triangular tips were unable to image in CAFM mode, presumably due to a large contact resistance. Given that there is a significant current passing through the Pt-tip, catalytic interactions with the surface are a topic of interest beyond the scope of this study.

2.3.3.1 CAFM Measurements

Conductive AFM (C-AFM) uses a conductive metallized tip that acts as a mobile contact to the sample. CAFM has proven abilities at discerning localized conduction by numerous groups. [22, 49] The CAFM capabilities of the Dimension 3100 are implemented in the form of two modules, the C-AFM (200 pA-2 μA) or TUNA (1 pA-100 pA) module, and a specialized tip holder that allows the current from the cantilever to be transferred to the modules. A specialized linear pre-amplifier converts the conduction between the tip and sample's surface into either a localized spectra or a map of conductivity across the sample surface depending on the mode of operation. By utilizing both of these features, the AFM can investigate the conduction characteristics of defects in various materials, temporally and spatially. The SSRM extension has a logarithmic amplifier, but does not have the spatial resolution of the C-AFM or TUNA modules, and cannot perform spectra.

When choosing a metallized cantilever for a given material system consideration must be given to contact friction effects on induced current and tip coating longevity. With a given metallization, the tip may also act as a catalyst for chemical reactions

involving the sample's surface and the atmosphere, or may degrade and react with the crystal along the scan cycles. Both processes would induce false current readings and characterize more the reaction of the cantilever coating than material under investigation. The measurements presented for Pt coated cantilevers on GaN may indicate more a localized reaction of Pt in atmosphere with GaN than the conduction aspects present in a Schottky contact.

2.4 GaN Devices

Fabrication of devices on GaN requires a strenuous series of processes. The exact nature of the clean room processes involved depends on the device type, though all samples should be cleaned and appropriately passivated, or etched, before device fabrication. Some devices need to be isolated on mesas or implanted with dopants. In a typical device fabrication the first step is sample cleaning in organic solvents, and possible wet or dry etchants. After sample cleaning, the next step in creating a contact is pattern transfer, using a mask aligner, into a photosensitive coating spun onto a semiconductor film. With a mask, the appropriate contact scheme is burned in the photosensitive material with ultraviolet light supplied via the mask aligner. The sample is then placed in a vacuum chamber, either electron beam (e-beam) evaporator or sputter machine, where the appropriate contact metal is deposited. Liftoff of the remaining photosensitive material defines the metallization of the contacts where a window was previously burned into the photosensitive material.

Contact metallization depends on the electronic properties that are desired and the material system under investigation; see sections 1.3.3 Electronic Properties, 2.2.2 Current - Voltage Measurements, and 2.4.1 Schottky Diodes. With multiple types of contacts in a device structure, it is necessary to consider the stability of contacts with respect to subsequent processing to determine the order in which they should be placed on the semiconductor to minimize degradation. Generally, any dry or wet etching to define mesas, or similar structures, will be the first step, followed by Ohmic contacts then Schottky contacts.

Achieving the desired electronic properties is a primary end point in semiconductor materials research and development. Contact adhesion is an essential aspect of commercial processing, a lack of it and devices are unreliable with a low yield. Working devices require wire bonding between the contacts and packaging with electrical leads. Adhesion is less of a concern with Ohmic contacts than for Schottky contacts, as the annealing after metal deposition aids in the diffusion of contact metal into the semiconductor, thereby drastically increasing the mechanical integrity and creating a low resistance path to the bulk material. Conversely, the Schottky contact cannot have alloying at the metal-semiconductor interface because this will add perturbations to the barrier height; and in the worse cases, could introduce parallel resistances to the Schottky contact. Parallel resistances provide an alternative route for electrons to move from the semiconductor into the Schottky contact, shorting the desired conduction response, and undermining the barrier and depletion depth of the contact. Threading dislocations, stacking faults, and surface conditions, among other defects, complicate the fabrication of

devices and accelerating degradation mechanisms in the thin film. Over time, degradation of the metal semiconductor contact can involve phase transitions of the surface and bulk material, resulting in contact alloying and oxidation, in some instances the interaction of these systems may become of interest.

Device contacts must be able to tolerate a wide distribution of temperatures and other forms of free energy in end-use devices. Unintentional reactions of the metal contacts and the semiconductor surface throughout any of the device processing will undoubtedly perturb the electrical properties. The growth conditions of a given film determine the unique defect structure and post growth treatment and exposure can significantly alter the native film's surface properties. Consequently, real devices have an ensemble nature about the conduction at a given potential and field, with many conduction mechanisms contributing to the measured current.[50] Regardless of the source of leakage current, available current conduction mechanisms can provide insight into the physical response of carriers to applied biases.

2.4.1 Schottky Diodes

The Schottky diode is an integral device in semiconductor electronics. A brief mention of diode properties from literature, with a focus on theoretical aspects begins the discussion, followed by a review of Schottky metallizations and reported properties. The next focus highlights the contact methods that have been successful or explored to achieve better performance. Concluding, devices utilizing Schottky contacts are included.

GaN Schottky contacts can reveal a wealth of information about the fundamental electronic properties. Schottky contacts are not only a critical component of many other devices, but they are also useful in establishing film properties and quality with various characterizations of the contact. Although early investigations proved the feasibility of III-V devices, numerous problems persist in literature concerning the quality of Schottky contacts on GaN. High leakage,[51] poor transport characteristics,[52, 53] or non-uniform / non-ideal barriers[54, 55, 56, 57, 58, 59, 60] plague Schottky contacts throughout literature.

Some boundaries have been established on material properties for free carrier concentration. Carrier concentrations above $10^{17}cm^{-2}$ introduce a tunneling component to current voltage responses; the source of this tunneling component is still in debate. Some groups attribute the abnormal transport mechanisms and non-ideal barriers to surface states,[61, 62, 63] while other groups identify dislocations [22, 23, 64] and bulk defects[39, 40, 41, 42] Reverse leakage current has been ascribed to electrically active defects, such as screw[22, 64] and edge disocations.[23] Point defects are ascribed as undoubtedly playing a dominant role in anomalous leakage in GaN devices.

Numerous metallizations have proven to produce Schottky diodes on GaN and AlGaN. N-type and p-type GaN have become prevalent and as a result various groups have characterized more metallizations. [1, 65, 66] The n-type metallizations are as follows: Au,[32, 67] Ag,[68] Al,[69] Ir,[70] Ni,[23] Mg,[71] Re,[72] Pd,[73] Pt,[50] W,[74] PdIn,[75] Cu_3Ge,[76] Au/Ni,[77, 78] Ta/Ni,[79] Au/Pt,[80] Pt/Au,[81, 82] RuO_2,[83] and ITO;[84] with the following metallizations nonexclusively suitable for AlGaN: Ti/Al,[85] Pt/Ti/Au,[86] Ni/Au,[86] Pt/Au,[81, 86] Ir/Au,[87] Au,[88] RuO_2,[89] Re,[90] and Pt.[91] Metallizations, Schottky and Ohmic, for p-type GaN

material are as follows: Ni,[92, 93, 94] Nb,[95] Ru,[96] RuNi,[97] NbAu,[95] Ni/In,[98] Pt/Au,[50] Ni/Au,[99, 100] Ti/Au,[101] Au/Pd/Mg/Pd,[102, 103] and TiN_x.[104] Pt has also been shown to be an effective Schottky contact to n-(GaMn)N by J. Kim *et al.*[105]

In addition to bulk properties, surface conditions play a critical role in determining the quality of Schottky interfaces,[106,107] where chemical absorption is the primary affecter of the surface energy structure. X-ray photoemission studies (XPS) elucidate the complex nature of GaN contacts in showing certain metals (Au, Pt, Ti), pin the surface of n and p-type material at different levels, while other metals (Ni, Pd, Al) follow Schottky-Mott theory in that the Fermi level is independent of doping.[108] Danielsson *et al.* determined the effects of substrate and buffer layers on the film's band offset, ranging from 0.6 – 0.9 eV, suggesting through modeling that recombination assisted tunneling plays a critical role in the transport of the film.[109] N.C. State laboratories showed in ultra high vacuum that Pd barrier heights are a complex mixture of material properties, including Metal-Induced-Gap States (MIGS) among others, resulting in a XPS and UXS barrier height of 1.3 eV.[110] A recent photoemission spectroscopy (PES) study indicated that both n and p-type GaN experiences band bending resulting in a Fermi level residing 2.55 eV above the valence band maximum.[111] Another report of Fermi level pinning states that both n and p-type GaN is pinned at 2/3 the energy band gap.[58] These results are problematic for Schottky contacts and indicative of the disparity in film quality from group to group.

There are other intrinsic properties providing more degrees of freedom for device fabrication of III-V semiconductors. For example, device geometry can yield devices

with tremendously different properties due to the propagation of dislocations on the growth front. In 2000, Mishra *et al.* reports marked improvements in mobility in Schottky contacts in the vertical mobility.[31] The film had a doping concentration of N_D = 1-2×10^{17} cm^{-3} and lateral mobility, $\mu_{lateral}$ = 150-200 $cm^2/V{\cdot}sec$, as determined from hall measurements and a reverse saturation current determined by current voltage measurements, Is = 1-10×10^{-9} $A{\cdot}cm^{-2}$. The reverse saturation current measurements of diodes in the vertical geometry yielded a mobility of $\mu_{vertical}$ = 1950 cm^2 V·sec. There was also a vertical mobility report by Mishra, Sampath, & Moustakas 2000, $\mu_{vertical}$ = 950 cm^2 V·sec, on a film with slightly lower doping concentration N_D = 8-9×10^{16} $A{\cdot}cm^{-2}$ and barrier height of 0.95 – 1 eV. [112] Zhang *et el.* reports on the difference in figures-of-merit for vertical versus lateral and varying area of Schottky edge terminate rectifiers. For 75 μm vertical Schottky contacts V_B ~ 700 V, yielding a figure of merit of 162.8 $MW{\cdot}cm^{-2}$, versus lateral V_B ~ 250, yielding a figure of merit of 36.5 $MW{\cdot}cm^{-2}$.[113] Differences in vertical and lateral properties are associated with dislocations in the film. As an interesting note, GaN Nanowires formed by CVD exhibited rectifying behavior for Al contacts and Ohmic behavior for Ti/Au contacts. The Nano-Schottky diodes possessed a 0.4 V turn on voltage at room temperature, which linearly decreased to 1 V at 10 K.[114]

Several groups have recorded the difference in barrier heights for the gallium and nitrogen faces of GaN. The reported barrier height of the Ga face ranging from 1.1 - 1.27 eV and the nitrogen face ranging from 0.75 - 0.9 eV. [115, 116, 117] It is suggested that spontaneous polarization plays a critical role by other reports, reporting differences over 1 eV can be obtained in N and Ga face samples.[118, 119] The large disparity could be a

result of MIG's. The question of polarity is clouded by recent reports showing that the N face of GaN is unstable, with the both clean unreconstructed faces showing midgap states with enhanced electron densities due to polarization.[120] Polarity is another unique characteristic of the III-V semiconductors, resulting from the wurzitic crystal structure. GaN films can terminate in Ga or N polarity; as a result, the barrier height has been shown to depend on the surface.[115] Complicating the situation though is the presence of inversion domains, small domains of inverted polarity. This question of polarity is clouded by recent reports showing that the N face of GaN is unstable, with the both clean unreconstructed faces showing midgap states with enhanced electron densities due to polarization.[120]

The thermal stability of numerous metallizations have been considered for GaN, among others: Re[72], W, [74] WSiN, [74] Nb, [74, 95] Ni/Au[77], Pt,[86] Ni,[86] and Ru.[96] Prompting the need for higher temperature contacts and demonstrating the importance of thermal stability, platinum Schottky contacts on AlGaN are reported to degrade at temperatures as low as 300 °C.[121] In addition to the contacts, the GaN epitaxial thin film may degrade with thermal cycling thereby inducing degradation in the Schottky contact properties.[122] Thermal stability studies establish operation regimes for metallization schemes. Ohmic contacts are generally insensitive to thermal effects, with contact resistance usually improving with increased temperature. In the extreme cases the contacts, or associated bonding in a packaged device, may experience oxidation / corrosion causing critical failures. Schottky contacts are much more sensitive to thermal effects, in the worst cases degrading into Ohmic contacts with no rectifying behavior.

2.4.2 MODFET's

The MODFET is a three terminal device composed of a source, gate, and drain. The source-drain bias sets the operation point, with the source is normally grounded. The drain and source are Ohmic contacts and the gate is a Schottky contact. The internal field at the heterojunction causes a depletion of charge from the barrier and accumulation in the buffer, creating a two-dimensional electron gas (2-DEG). At low source drain fields the response of the carriers is linear, though as the field increases the conduction volume of the channel saturates due to the field – mobility relationship. The proceeding carrier dynamics are characterized by field dependent mobility in the linear region, at some critical field the velocity saturates, becoming the limitation on device operation. By reverse biasing the gate junction, the charge in the 2-dimension electron gas (2-DEG) can be modulated with gate bias controlling the effective cross-sectional channel volume for source-drain carrier flow, defined as the transconductance (dI_D/dV_G). Increasing the gate bias in negative polarity will eventually cause a quenching of conduction form the source to the drain; this point is defined as the pinch-off voltage (referenced from the gate). Before pinch-off has occurred, the saturation point on the source-drain current-potential response will move to smaller values, as the critical field for velocity saturation decreases with decreasing channel cross-section, or increased reverse bias.

In most operational respects the MODFET resembles the familiar workhorses the Metal Oxide Semiconductor Field Effect Transistor (MOSFET) and the Metal Semiconductor Field Effect Transistor (MESFET), yet improves on their DC and high frequency responses by isolating the charge for device operation in a high quality low

scattering channel. From a DC electrical characterization point of view, the MODFET also improves on MOSFET's breakdown and saturation characteristics and can demonstrate better transconductances. The MODFET achieves this by increasing the carrier concentration in the buffer without introducing doping related scattering and utilizing the buffer's strain enhanced channel mobility. The density of carriers in the channel will determine the mobility to a first extent, as layer and interface quality, among other aspects, are secondary. Ultimately the goal in MODFET applications is to provide a device with stable operation, maximum current density in the channel and a symmetric large transconductance, achieved by maximizing the confinement of carriers in the 2-DEG at the heterointerface with minimal scattering in the channel.

The MODFET relies on the population of a quantum well formed at the heterointerface by carriers from the large bandgap strained film, the barrier, to the smaller bandgap semiconductor, the channel. Lattice matching of the barrier and the buffer will increase the quality of the barrier film and the resulting quantum well that contains the 2-DEG at the heterointerface. Ideally, in an n-N heterostructure without a gate contact, the energy band diagram from the surface of the barrier will have an upwards-curving slope in the conduction band that ends abruptly at the interface. From the interface, the buffer's conduction band takes on a saturating effect, starting well below the Fermi level at the interface; and saturating at some distance from the interface into the buffer, at the buffer's conduction band energy.

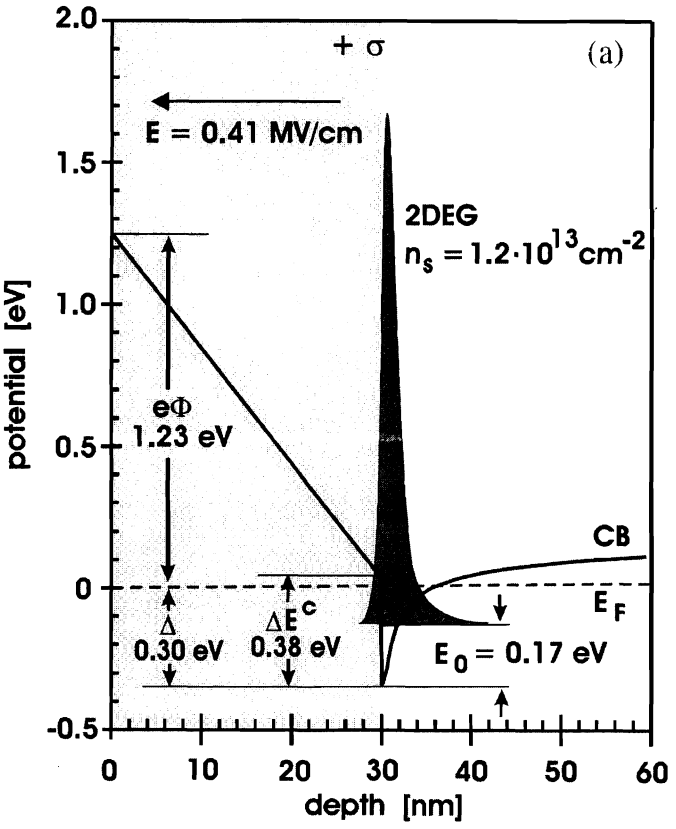

Figure 10 - MODFET Energy Band Diagram and 2-DEG Characteristics

Using the following formulations for polarization and spontaneous charge, the 2-DEG carrier concentration, n_S, the 2-DEG first energy level, E0, the conduction band offset, ΔEC, and the Ni barrier height including surface polarization charges for an undoped Ga-face Al0.3Ga0.7N/GaN (30/2000nm) heterostructure was determined (from Ambacher *et al.*).[15]

Figure 10 - MODFET Energy Band Diagram and 2-DEG Characteristics details an energy band for a MODFET, is a conduction band energy diagram of the MODFET

heterointerface with a gate contact, energy states will form in the area contained by the interface, the saturating buffer conduction band edge, and the Fermi level, confining carriers and creating the 2-DEG. Additionally, with the consideration of the gate and surface polarization charge, at the surface the conduction band starts at the modified gate potential and slopes linearly to the interface. The population of these energy states and the 2-DEG's existence can be proven from low temperature magnetic studies involving Shubnikov de Haas oscillations[123] or with temperature variant PL measurements. Adding an extra degree of freedom in device design, piezoelectric and spontaneous polarization complicate the particulars of MODFET design in the III-V's, introducing a new set of challenges for reliable device fabrication.

The material's structure determines the drain-current response; consequently, if the material is poor then the contacts cannot correctly modulate the current in the devices. To a first order, the physical limitations that must be dealt with are the quality of the 2-DEG, with the resultant mobility and velocity field relationship. Growth conditions such as layer thickness, alloy composition and doping of AlGaN, and structure, determine the density of carriers in the 2-DEG. By choosing the appropriate mole fraction for the barrier, the piezoelectric strain in the heterostructure can be used to maximize the electrical characteristics. Polarization in ionic non-symmetrical crystals, such as the III-V's, will enhance the charge depletion in the barrier and accumulation in the channel. In order to increase the mobility, and saturation velocity, a well formed 2-DEG with low interface scattering, alloy disorder, and dislocations is essential.

Achieving a high mobility film is essential for microwave device performance. A optimized useable device must have a large number of carriers, ~1 A/mm on sapphire, channeled through the device with a small applied bias source to drain, and an even scaling of transconductance with swings in gate voltage. A competitive GaN transistor on sapphire would have an f_T over 20 GHz and an f_{MAX} over 50 GHz. A power added efficiency of 25% with a noise figure of ~ 1 dB at a gain of 10 dB with transconductances in the range of 150 – 200. These goals can be achieved through layer optimization, reduced contact and channel resistance, and ideal Schottky gates. The product of mobility and sheet carrier concentration is often used as a figure of merit for HFET structures;[124] a realistic goal for high quality transistors would require this product to be in the range of 10^{16} $(cm*V*Sec)^{-1}$. For minimal carrier-carrier interactions, this would require sheet carrier densities of 10^{13} cm^{-2} and a room temperature mobility of over 1000. Sheet carrier concentrations over 10^{13} cm^{-2} would increase carrier scattering and the increase thermal effects.

Qualities of poor MODFET devices include: poor current capacity, low drain breakdown voltage, non-uniform (or low) transconductance, large noise figure, and low drain output efficiency. Electrically active defects introduce increased Columbic scattering, while non-electrically active defects are non-radiative scattering centers, both increasing scattering, and consequently noise, in the channel current. Interface roughness, as well as no uniform barrier composition and thickness can highly influence charge localization in the channel of MODFET's. Charging point defects mediate the transient characteristics of the transistor, as well as increasing scattering.

The buffer and substrate can contribute significant problems to the device operation. If the device layer, or substrate, has a low thermal conductivity then heat generated in the device cannot be dissipated to the environment. For the III-V's on sapphire, internal heating of the device will cause an increase in the carrier concentrations and increased device heating through inelastic scattering mechanisms, starting a run away condition for the device under extended operation. Leakage through the buffer can also cause severe problems for the MODFET, gate control would be lost in a buffer with low resistivity resulting in a defunct MODFET, two step saturation or high linear slope in saturation (could also be the result of leaky gate). One possible cause of a low shunt resistance through the buffer is high concentrations of point defects in the buffer, resulting from either poor growth conditions or a bad substrate / interface. Increasing the resistivity of the buffer in III-V's and eliminating this effect is achieved by compensating the buffer with Zn, Co, Be, or Mn.

A normal MODFET device structure consist of a wide bandgap semiconductor, barrier, grown on a smaller bandgap semiconductor, buffer. An improvement on the normal MODFET design is the inverted MODFET, which has a thin (~2-5 nm) capping layer of the buffer semiconductor, or other smaller bandgap semiconductor, to increase the effective barrier of the gate terminal, thereby preventing conduction from the gate into the channel. The back-doped heterostructure field effect transistor (BD-HFET), another design improvement, is a structure with a larger bandgap material backing the channel.[125] In this design, the carrier densities in the channel are very high $3X10^{13}$ cm^{-2}

with very thin barriers 12 nm, this allows for high transconductances due to the thin barrier with extremely high current densities 1.2 A/mm.

In improving the layers from the growth side, an investigation was done to characterize the effects of strained layers underlying the channel with respect to parallel conduction.[126] It is widely reported that the introduction of strained layer multiple quantum wells (MQW's) can be effective in reducing the threading dislocations and correspondingly improving the layer, though the possibility of parallel conduction in the MQW's could undermine the MODFET's performance, especially Rf characteristics. The introduction of strained layers improved the channel mobility from 1187 $cm^2/V{\cdot}s$ to 1443 $cm^2/V{\cdot}s$ with carrier densities in the range of 1.0-1.2 $\times 10^{13}$ cm^{-3}. A reduction in the interface and dislocation related scattering are identified as the primary reasons for the improvement in mobility. Capacitance voltage data from Pt contacts on a 45 nm $Al_{0.22}Ga_{0.78}N$ / GaN heterostructure was analyzed by Zhou *et al.* considering multiple interface properties, using 3-d Fermi calculations.[127] The results yielded a polarization-induced sheet charge density of approximately $6.78*10^{12}$ cm^{-2}.

Aside from these fundamental channel issues linked to MODFET's design, gate issues further complicate reliable fabrication. Native oxides are notorious for transport and frequency related effects. Nonuniform tunneling barriers exist across the contact, varying as a function of oxide thickness, thin film's defect microstructure, and gate geometry variances. With extended defects creating nonuniform potentials, native oxide growth would tend to passivate areas within the range of environmental thermo-chemical

reactions. Additionally, screening of surface structures would lead to an ensemble of barrier heights, introducing variable regions of conductance and capacitance.

Leakage associated with the gates of MODFET's is a primary flaw in devices. Once leakage issues are resolved, including any electrically active dislocations, surface interface states, metal induced gap states (MIGS), bulk trapping defects, and polarization issues with dislocations, more fundamental problems such as persistent photoconductivity, drain current lag, and current collapse (all of which are beyond the scope of this text) can be clearly investigated. The solution for optimizing MBE films on sapphire lays in improving layer quality and passivation any surface anomalies, to ensure reliable and proper device characteristics. It is essential for MBE grown films to utilize novel growth techniques, such as nanolithography, porous regrowth, or etched surface regrowth, to achieve DD in the range of 10^8 and minimal point defect concentrations for suitable MODFET performance.

A series of representative MODFET curves and relevant theory are presented to demonstrate the coupling of leakage to the operation of a higher-level device. A standard measure of a transistors characteristic is the drain-source current, I_{DS}, as a function of the drain bias and negative gate bias. The drain-source current versus voltage curve for a representative device is presented as Figure 11 - MODFET Drain current curves - I_D vs. V_{DS} as a function of V_G.

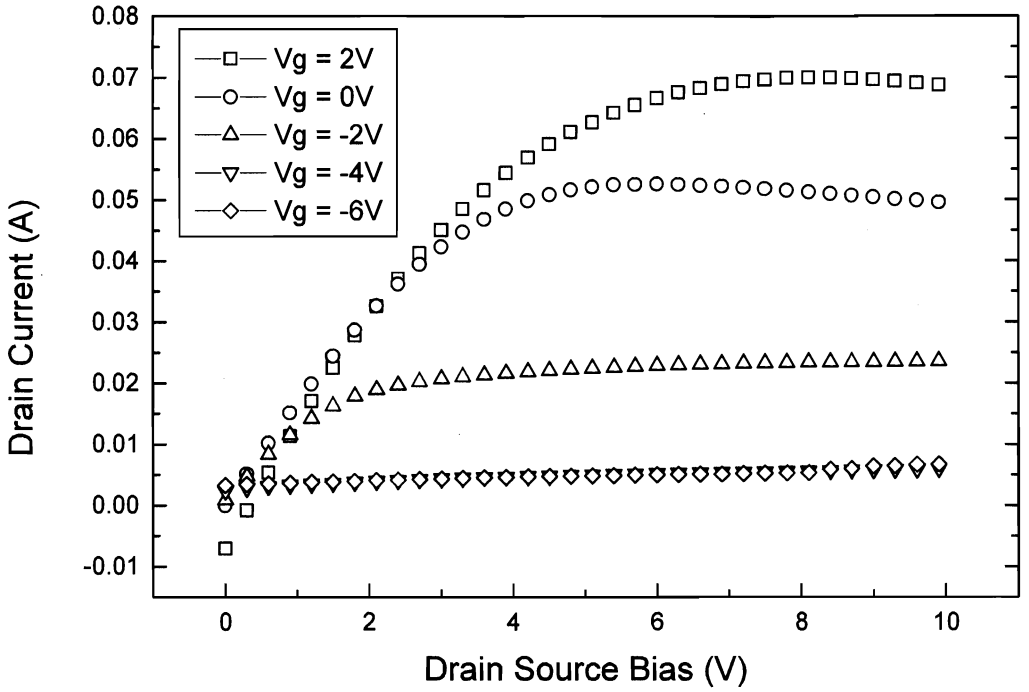

Figure 11 - MODFET Drain current curves - I_D vs. V_{DS} as a function of V_G

The point at which the drain current begins to saturate defines the critical field where the carrier transport in the channel has become velocity limited; the corresponding voltage is the knee voltage. The drain-source current quenches between 4 and 6 V, defining the pinch-off voltage, V_p, and the separation of the I_D associated with a given V_{DS} (dI_D/dV_G constant V_{DS}), defines the transconductance. The drain-source biasing point is defined as the quicient point, ideally the most linear region of the device's transfer function. The large signal characteristics are limited by the quicient point and symmetry of the

transconductance, while the small signal characteristics are limited by leakage and material quality. Figure 12 - MODFET Transconductance Curve characterizes a typical transconductance curve for a device at MMDL.

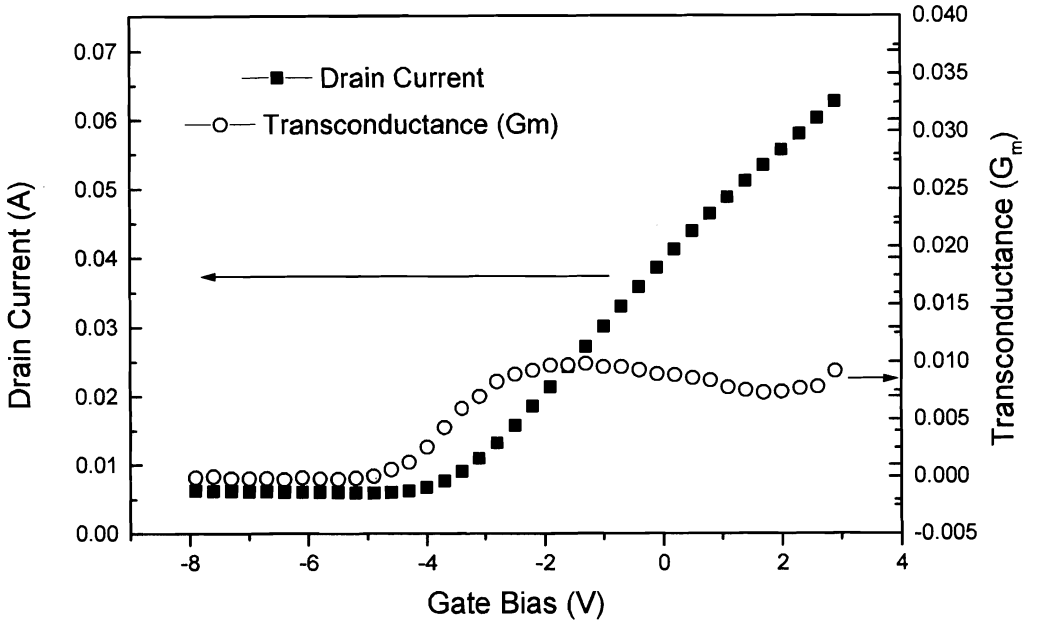

Figure 12 - MODFET Transconductance Curve

The transconductance curve is obtained by sweeping the gate voltage at a constant drain-source bias, ideally slightly large than the knee voltage. Large signal voltages on the gate may swing the drain current response into unstable regions of operation. The current is divided by each voltage step according to Figure 12 - Equation 53 - Transconductance.

Equation 53 - Transconductance

$$g_m = \frac{\varepsilon v_{dsat} W_g}{d} = \left| \frac{\partial I_{DS}}{\partial V_{GS}} \right|$$

In the above expression, g_m is the measured transconductance, ε is the semiconductor's dielectric constant, W_g is the gate width, and d is the channel length. The max transconductance defines the gate bias for best device operation. By finding the intercept of the transconductance curve at biases just more negative than the max transconductance reveals the pinch-off voltage, V_p.

With the moderate MODFET characteristics of this device, the gate leakage enumerates the potential of high quality material. Gate leakage is measured by sweeping the gate bias and measuring the current with the drain and source grounded, Figure 13 - MODFET Gate Leakage Curve.

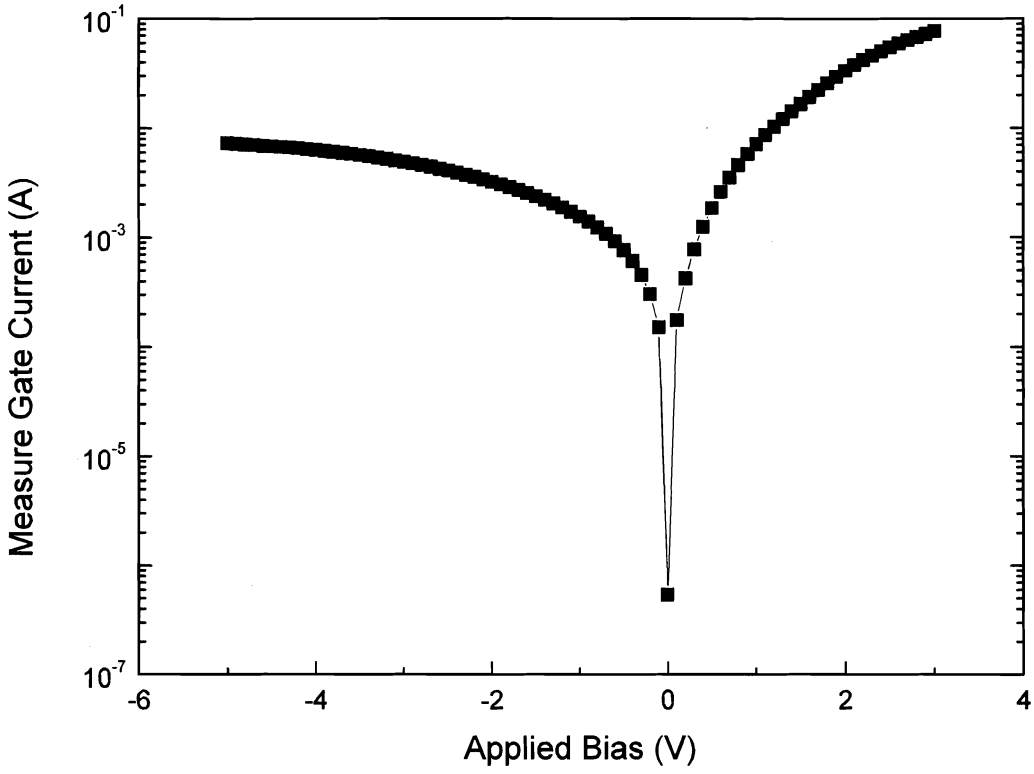

Figure 13 - MODFET Gate Leakage Curve

Standard techniques for analyzing Schottky diodes can be on the above data when considerations of the additional factors at play are considered.

2.4.3 Other Devices

The family of III-nitrides offers a unique opportunity for heterojunction p-n junctions. Using a high quality acceptor substrate with a high quality n-type GaN overgrowth, or other III-nitride, a superior p-n type device can be created utilizing the

heterojunction capabilities to manipulate interface charge. Although the devices do not have Schottky contacts, there are comparable expressions that can be used to understand the current density flow of majority and minority carriers on each side of the heterojunction. Serious issues with the heterojunction bipolar devices include interface quality and extended defects. Curve fitting techniques enumerated in this study could be used to gain insight into the carrier dynamics. The most critical aspect of the p-n heterojunction is the interface between the p and n type material, where strain is the greatest, and extended defect nucleate with heteroepitaxy. If the interface is less than perfect, a plethora of interface states will effectively short the device into a resistor.

A popular microwave device is the negative deferential resistance (NDR) device, or the Gunn diode. An NDR device utilizes a series of heterostructures to create a quantum well array. The tunneling aspects of carriers are a function of the well structure. Given the presence of a series of quantum wells under the influence of a field, the states in adjacent wells are unaligned, or inaccessible due to low tunneling probabilities. As a potential is increased the states in the quantum wells align and the tunneling probability drastically increases. At some voltage, a current peak is observed in a log(I) vs. V plot of the device. When the potential is further increased the states in the quantum wells becomes unaligned and the effective resistance of the structure increases causing a decrease in measured current. A Gunn diode is a special case of an NDR device, as is a heterostructure NDR device, which utilizes the relaxation of energetic carriers into adjacent conduction band valleys to alter the effective resistance and cause a current spike in a log(I) vs. V plot. The quality of material is again the crux of the device. An

attempt was made to deposit and fabricate heterostructure resonant tunneling diodes (RTD's) at MMDL, though no NDR effect was seen at liquid nitrogen temperatures.

The remarkable potential of the III-Nitride materials has demonstrated many other working devices. Sought after oxide based field effect devices have gained ground as of late, with 1998 reports of insulated gate hetero field effect transistors (IG-HFET's) with transconductances in the range of 235 ms/mm for a 1.4 mm gate on MOCVD films, AlGaN/AlN (4 nm)/n+ GaN (15 nm)/GaN.[128] The first reports of spintronic based Schottky contacts are based on polycrystalline $La_{0.7}Sr_{0.3}MnO$ (LSMO) thin films.[129] LSMO thins films of 500 AA thick undergo ferromagnetic behavior at 330 K. Optical detectors were also fabricated at MMDL though leakage issues severely hindered their performance.

2.5 Sample Preparation

Fabrication procedures for any semiconducting material involve some degree of substrate cleaning and preparation. Following cleaning, the sample will have contact metallizations defined and contacts formed via e-beam evaporation, sputter deposition, or some form of plating. In some cases, mesas must be defined with a variant of plasma or wet etching. Crystal etching is an effective method of not only removing material, but also changing the surface conditions depending on the etchant and processing conditions used.

A comparison of dry versus wet chemical etching displays the potential benefits in reduced on-state resistance of wet over dry etching.[130] Mistele *et al.* showed that

active N_2 is effective at increasing the Schottky nature of contacts, while Ar and $ArCl_2$ processing produced Ohmic contacts.[131] The diatomic nitrogen species removes the near surface N-vacancies thereby improving the device characteristics. A UV-ozone technique was described by Zhang *et al.* for partial restoration of device characteristics.[132] In a similar study boiling NaOH was used for treating plasma induced surface damage.[133] Recessed gate FET processing using SF_6+N_2 plasma is proposed by Rong *et al.*[134] Increasing the number of N vacancies has been shown to shift the Fermi level by as much as 0.5 eV towards the conduction band edge for Cl_2 plasma etching,[135] and increasing the Ohmic nature of Ti/Al contacts by Jang *et al.*[136]

Annealing is another approach aimed at improving the quality of the bulk semiconductor material and contacts. Bell *et al.* present ballistic electron emission microscopy (BEEM) data for Au Schottky contacts that demonstrate the improved transmission characteristics of moderately annealed temperatures.[137] Annealing the semiconductor material in an ammonia ambient at ~450 °C prior to contact processing was identified as a better preparation method over conventional HF and HCl wet chemistry preparations.[138] The ammonia anneal not only restored the stoichiometeric balance to the surface but also left the surface halogen free. High residual traces of halogens were found to occupy the dangling bonds on the GaN surface after HF and HCl treatments. Cao *et al.* investigated H_2, N_2, Ar, and $ArCl_2$ dry processing effects on GaN. The findings also identify a near surface nitrogen vacancies as a source of leakage. Plasma processing introduces defects in the near surface region, annealing at 750 °C in

N_2 environment followed by wet etch removal of 0.5-0.6 nm fully recovered device characteristics.[139]

. Jang and Seong report on the effects of a buffered-oxide etch showing a decreasing Pt barrier height with increasing time.[140] The mechanism responsible is recognized as a reconfiguration of the Ga 2p and Pt 4f core levels determined through XPS. HFET's Ohmic contact resistance was lowered using KOH etching, buffered with $K_2S_2O_4$, under UV illumination.[141] Using PEC techniques with an aqueous KOH solution, etching, oxide growth, or oxide removal is possible.[142, 143] PEC etching is the most advanced technique, in that it controls the most degrees of freedom from a free energy prospective. The above reports identify the necessity to investigate the sequence and extent of each processing step. Introducing known perturbations, such as etching, and correlating the results to other characterization techniques is essential to understanding the cause of problems and identifying processes to produce reliable contacts.

2.5.1 Sputter vs. E-beam / Thermal Evaporation

Deposition of contacts are generally done in vacuum by two methods, either sputter deposition or electron beam / thermal evaporation. There are advantages to each technique, sputtering has the advantage of insulator deposition though both techniques are capable of depositing metals on a variety of materials. Sputter deposition relies on bombarding a target of ultra pure material with plasma of a given carrier gas, usually Ar, O, or N, creating a flux of reactive high energy target species towards the substrate. On

the other hand, electron beam deposition utilizes a beam of electrons to elastically excite and eject material from a target boat towards the intended substrate. Thermal evaporation resistively heats a filament, or boat, of target material. Process variables for the above techniques are chamber pressure, flux rate, flux energy, flux distribution, sample heating characteristics, and sample orientation / rotation. Just as with semiconductor thin film, the chamber pressure is important two fold, first it can incorporate impurities into the contacts / interface through background partial pressures, and secondly the chamber pressure (and introduction source) determines the rate and the spatial-energetic distribution of metallization flux. The other interrelated deposition chamber process variables are defined in mass, heat, and charge transfer.

It is imperative to remember the effects of processing on the final product as demonstrated by a DLTS study of sputtering effects of Au Schottky contacts, performed by Auret *et al.*[144] The comparative study of resistively evaporated versus sputtered formed contacts uncovered speculative sputtered induced trap levels at E_C-E_T = 0.22±0.02, 0.30±0.01, 0.40±0.01, and 0.45±0.01 eV. The 0.22 eV trap is correlated to a radiation induced nitrogen vacancy and the 0.30 eV trap; reported to be related to a bulk defect. Aside from the very base differences between e-beam / thermal and sputter contact deposition, i.e. target excitation, sputter deposition allows for forms of ion assisted deposition and the ability to change the ambient gas of the chamber, providing for more exotic device / contact structures. Electron beam deposition has the same degree of control as sputter deposition, as far as flux excitation, and is oriented more

specifically to contact deposition. Devices characterized in this study were fabricated using E-beam / thermal deposition of contact metals.

2.5.2 Surface Preparation

At MMDL, when dealing with high-level devices, such as the MODFET's, film adhesion was a major problem cited with the Schottky gate contacts. After lift-off of the photolithography mask, partial or non-existence gates were common with low quality films. Two competing ideas arise to explain the lack of adhesion. First, the metal-semiconductor junction is significantly chemically contaminated with oxygen, chlorine, or some other species either from process or environmental exposure, evidenced in the iridescence of contacts and films after device processing. The second possibility is that reactions at the semiconductor-contact interface are enhanced by the extended defects, or stress and strain in the contact becomes significant enough to cause delamination of the Schottky contact. High temperature annealing is a predominant method for rugged near ideal Ohmic contacts with good adherence, identifying diffusion and alloying as the primary mechanisms responsible. Adhering metals for Schottky contacts, without introduction of alloys between the semiconductor and contact metal, is essential for high quality heterostructure devices. The cleanliness of the material and processes, film surface roughness, and defect structure are primary affecters for adhesion.

In wet beaker chemistry the environmental conditions, such as agitation, temperature, pressure, etc., determine the free energy of the solution and crystal. The most important area is the interface between the crystal surface and the solution. Chemical preparation of the surface can remove detrimental non-uniform thin oxide

layers,[138, 145] with several parameters determining the rate of a given reaction: solubility, diffusion, charge transfer, chemical potentials, and temperature. Advanced techniques, chemical mechanical polishing (CMP) and electrochemical (EC) techniques control more degrees of freedom increasing the range of etch variations.

Using electrochemical techniques, the quality and anisotropy of the etching mechanism can be controlled better than non-anodic wet beaker chemistry. Using a standard reference probe, generally isolated from the solution, potentials can be applied to the sample, working electrode, increasing the availability and reactivity of free electrons. The counter electrode is used as the ground and is generally a platinum alloy, or platinum coated alloy. By sweeping the potential, or forcing current into or out of the working electrode, the chemistry at the sample solution interface can be highly controlled. Among the advantages are a direct measurement of the mass exchange (identification and count) and extended ability in control over the anisotropy, rate, and by-products of the reaction. The most basic experiment is the open circuit potential (OCP) of the system. If the OCP is unstable, it denotes that a significant reaction is taking place. On the other hand a stable OCP does not indicate no reaction, just that the rate is small at the given conditions. The potentiodynamic measurement can identify corrosion rates and ranges of potential for given reactions, i.e. oxidation versus corrosion. The addition of illumination adds another degree of freedom, termed photoelectrochemical etching (PEC). Electrochemical impedance spectroscopy (EIS) is capable of identifying chemical species in an etching process.

Chemical passivation is effective at improving device transport characteristics and reducing leakage through Schottky type interfaces. The following materials / substances have been shown to effectively passivate GaN and AlGaN materials: NH_4OH,[146] $(NH_4)_2S_X$,[145, 147, 148] SiO_2,[149, 150] NiO / NiO(Li),[151] Al_2O_3,[152] Si_xN_y,[86] and SiN_x.[153, 154, 155] The most effective form of passivation is demonstrated through a combination of chemical preparation followed by passivation. Hashizume *et al.* show that unstrained SiN_x passivation, verified by Raman studies, preceded with NH_4OH treatment and N_2 plasma-processing yields an interface with a specific charge of 2×10^{11} $cm^{-2}eV^{-1}$.[156] The potential benefits of sulfide containing solutions is illuminated by Martinez *et al.*, increasing photoluminescence intensity by four to six orders, the proposed mechanism is reduced surface recombination velocity.[157] It is believed that the surface is passivated by sulfur reacting with dangling Ga bonds, though extensive effects of sulfides on contacts' properties, thermal, adhesion, and atmospheric stability are yet to be determined.

The complex state of contacting to GaN is largely a result of the surface terminating and bulk defect structure. Numerous interface reactions are a combined result of structural effects and their interactions with free energy in processing steps. Another approach recently reported improved transport characteristics and reduced leakage current in Schottky diodes by locally oxidizing electrically active screw and mixed dislocations with electric force microscopy (EFM).[158] Studies such as Mistele *et al.*, demonstrate the true complexity of surface, and contact, preparation by showing that the processing steps often causes undesirable effects.[131]

3 Results

Leakage current is unarguably a result of fabrication processes, growth conditions, substrate type and preparation, and post growth environmental conditions.[159] Some groups have employed growth techniques to minimize the effects of electrically active defects on leakage current,[160] still the exact nature of leakage current has yet to be completely identified. In the results following, Schottky investigations will be compared with CAFM results, and supplemented with Hall, PL, and TEM data where available. Electrically active defects, identified as highly localized, high conductivity regions at low biases have been identified through CAFM measurements and correlated with Schottky diode properties.[22, 161] Non-uniform native oxides could also be the culprit of a number of transport, leakage, and capacitance related problems for GaN films and conflicting characterization reports.

In the CAFM topography, large area barrier height lowering was observed in the regions of increased conductivity, evidenced in surface structures near electrically active defects conducting at elevated biases independent of polarity, and on the side walls of inversion domains. A complex interplay between crystallographic defects, free charge,

and surface structures is observed in the CAFM scans. As the bias is increased more structures become conductive, in effect create a highly complex barrier height that is a function of the standard metal work function, crystal work function, previous electrical excitation, and crystal / surface defect energy structures. Schottky diodes exhibited varied results with molten KOH discriminately providing benefit to the electrical properties. A number of alternatives exist to reduce leakage, though reducing the density of defects through growth methods remains the absolute key to successful devices.

3.1 Samples

Devices were prepared identically for both as-grown and KOH-etched samples as follows: samples were cleaned in acetone, methanol and de-ionized water, respectively. Aqua-regia (3:1 $HCl:HNO_3$) was then used to remove the oxide layer from the surface of the sample. Optical lithography defined the contact area, 75 μm diameter Schottky diodes with a 300 μm diameter window and an Ohmic pattern interlaced between the diodes. The Ohmic contacts were a Ti/Al/Ti/Au (300 Å/1000 Å /300 Å /150 Å) metallization, deposited using electron beam for Ti and thermal evaporation for other metals. A standard lift off process was applied in acetone to pattern the contacts. The contacts were annealed at 900 °C for 1 min by Rapid Thermal Annealing (RTA) in nitrogen ambient. After liftoff and photolithographic Schottky contact window definition, Ni/Au (300 Å /750 Å) metallization was used to form the Schottky contacts. The samples presented in this study are presented in Table 1 – Sample Designations.

Table 1 – Sample Designations

Sample	Polarity	MQW's	MODFET	I V	I V T	C V	CAFM – Topography	CAFM - Spectra
381	Ga						×	
429	Ga			×	×	×	×	
618	N						×	
666	Ga						×	
680	N						×	
750	Ga	×		×	×		×	×
885	Ga		×				×	×
889	Ga			×			×	
1016	Ga			×			×	×
1026	Ga	×		×			×	
1460	Ga			×			×	
R6565	Ga		×	×				
Samsung	Ga			×	×	×		×

A high quality HVPE sample from Samsung is the reference sample for macroscopic Schottky studies. Schottky contacts were formed on the N and Ga faces of the sample. After mechanical polishing, potassium hydroxide etching was performed on the sample prior to contact fabrication. The current voltage curves as a function of

temperature (IVT's) for Ga polar devices are presented as Figure 14 - Samsung Ga-face Current Voltage Temperature Curve.

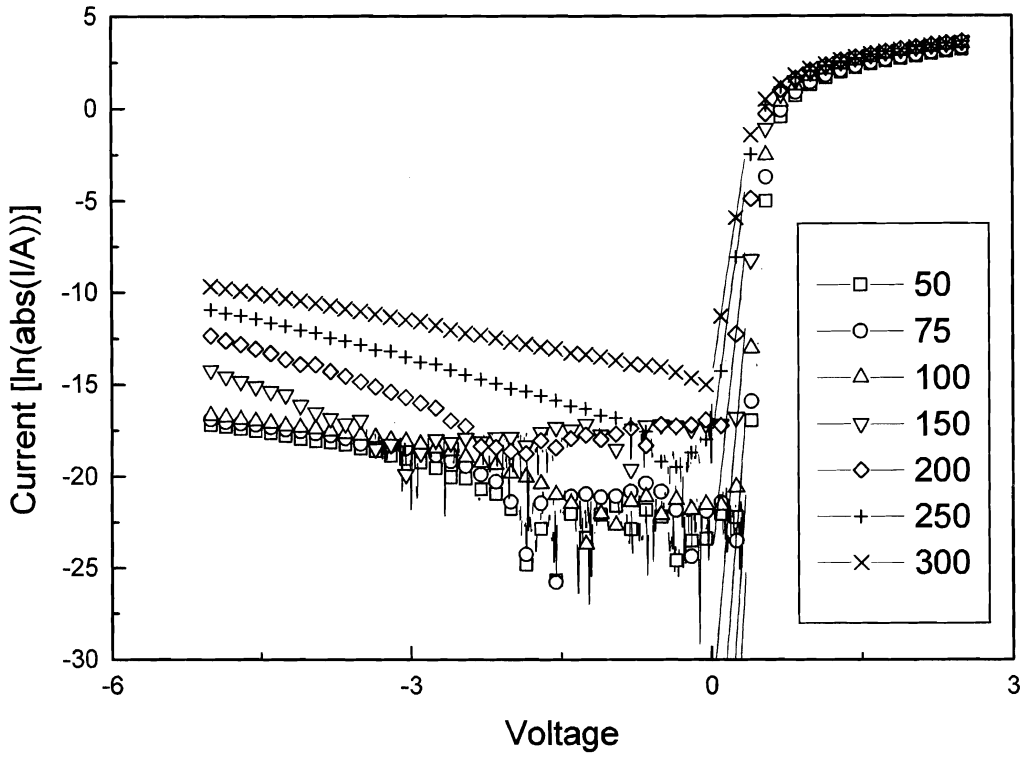

Figure 14 - Samsung Ga-face Current Voltage Temperature Curves

It is interesting to note the noise factor of the leakage current at low temperatures, it may be attributable to defects or vibrational noise in the test setup, though the minimum level seen varies from sample to sample. According to section 2.2 Electrical Measurements, the samples were further investigated by capacitance voltage measurements. The inverse

capacitance squared versus voltage is presented as Figure 15 - Samsung Capacitance-Voltage Curves and the donor concentration versus depletion depth is presented as Figure 16 - Samsung Donor Concentration vs. Depletion Depth.

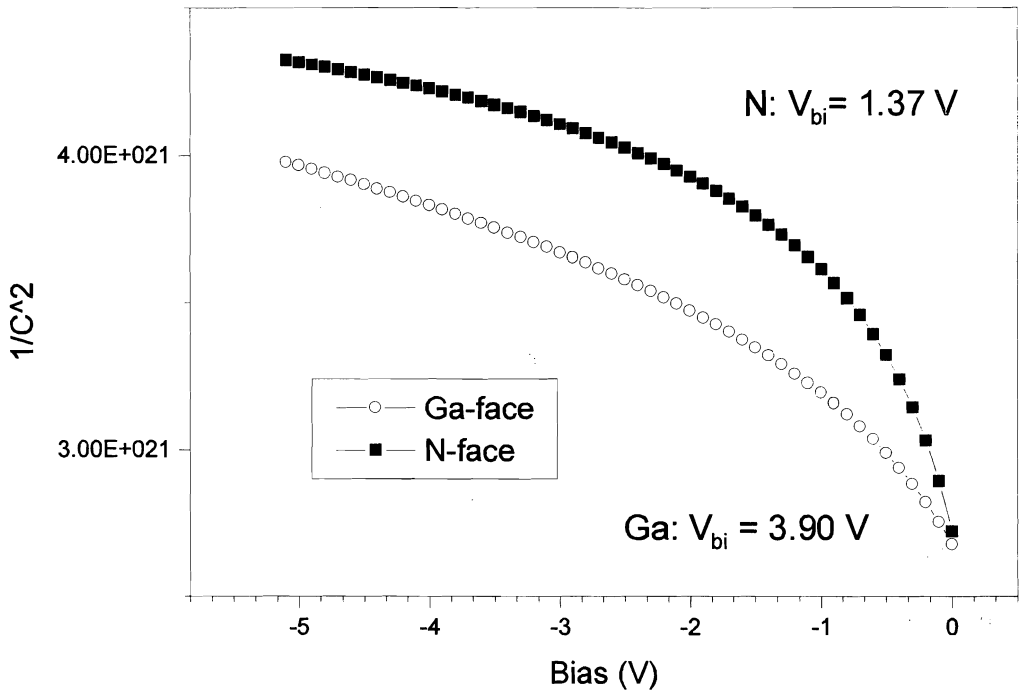

Figure 15 - Samsung Capacitance-Voltage Curves

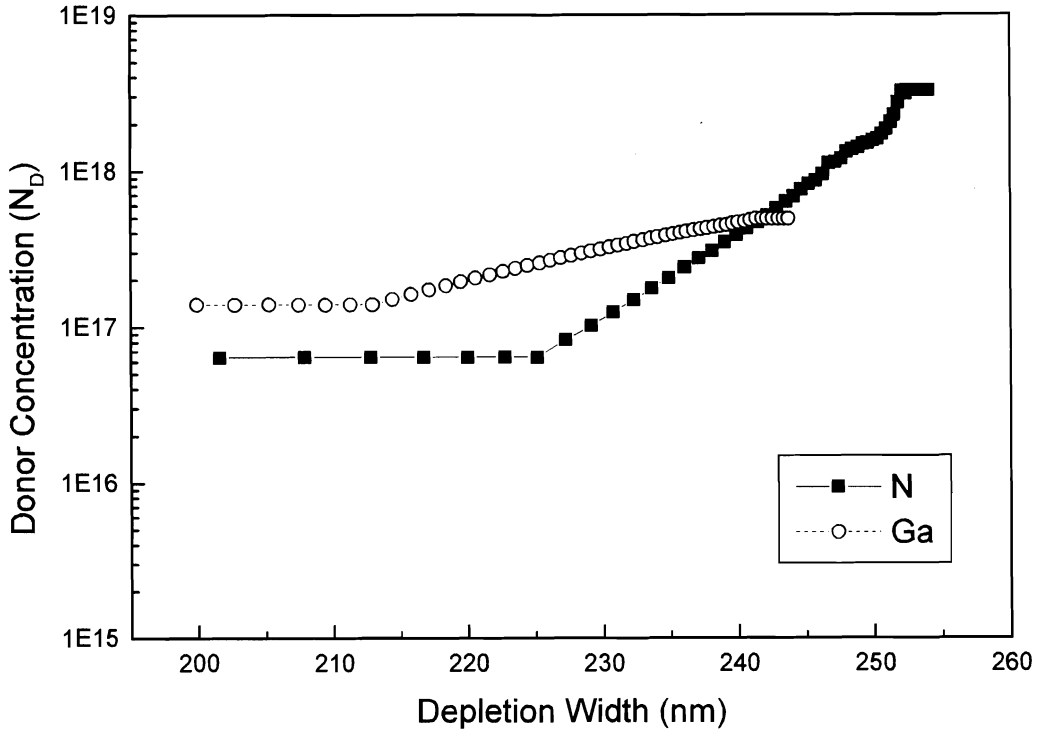

Figure 16 - Samsung Donor Concentration vs. Depletion Depth

The N-face sample had superior IV curves to the Ga-face Samsung samples. The built-in voltage and carrier concentration for the N-face was 1.37V and 6×10^{16} cm^{-3}. The Ga-face had a built-in voltage over three volts and a carrier concentration in the low $10^{17}cm^{-3}$. After verifying the Schottky contact thermionic character, a modified Norde plot was formed from the forward bias portion of the current voltage curves, Figure 17 - Samsung Modified Norde Plot.

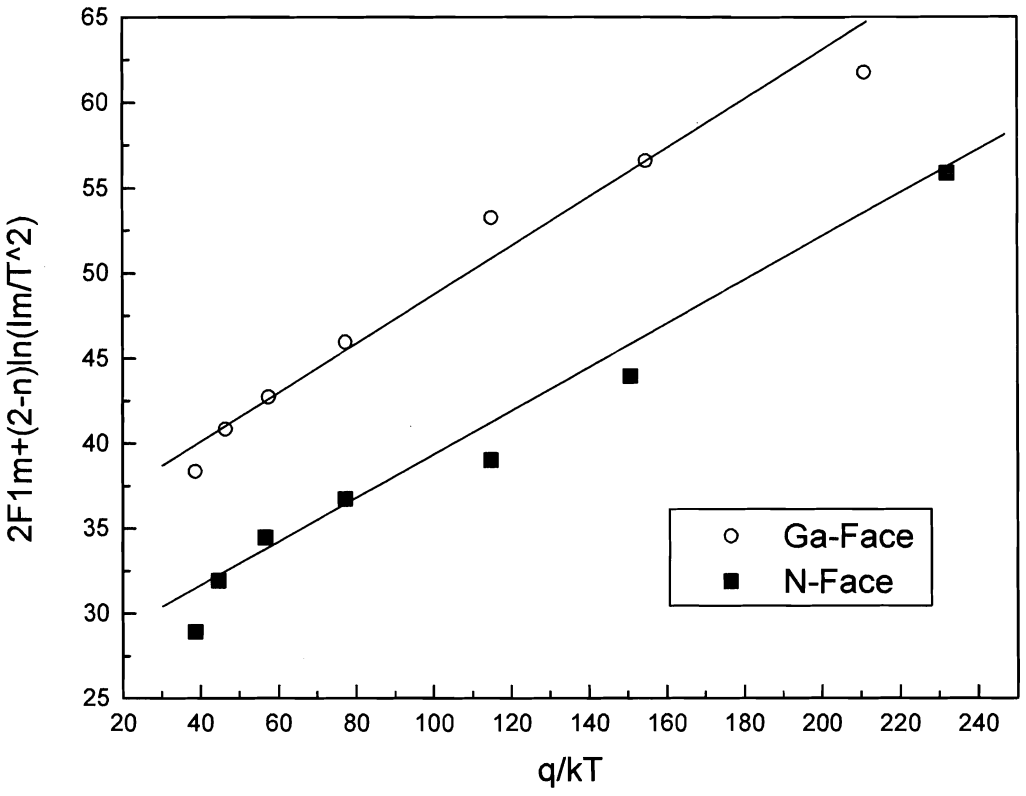

Figure 17 - Samsung Modified Norde Plot

The Richardson's constant is calculated to be 34.94 for the Ga-face and 25.72 for the N-face. The barrier heights calculated as 0.135 eV for the Ga-face and 0.127 eV for the N-face. Both values are also abnormally low as compared to standard methods but may be more indicative of the field emission component of leakage current.

3.1.1 SVT 429

A Ga-polar N-rich n-type overgrowth on sapphire with an NH_3 surface fix,[162] SVT429 represents a high quality, high resistivity MBE reference sample, $n = 10^{17}$ cm^{-3}, $\mu = 472$ cm^2/V · sec, $\rho = 20\ \Omega \cdot$ cm. The layer structure for the overgrowths and material properties can be seen in Figure 18 - SVT 429 Growth Conditions and Material Properties.

Film Thickness: 0.8 μm; N-Rich

Surface Fix: GaN $T_s = 745$ °C
GaN NH_3(30 sccm), $T_s = 928$ °C, P = 3X10^{-5} Torr, 2 hrs
AlN RF(325, 3.16), $T_s = 980$ °C, P = 6X10^{-5} Torr, 25 min
Al_2O_3

- **PL**
  Peak: 3.303 eV
  FWHM: 10.5 meV
  QE: 0.31 %
  Multiple Excitons bound to structural defects

Figure 18 - SVT 429 Growth Conditions and Material Properties

Reference sample SVT429 exhibited ideality factors ranging from 1.0-1.3, the KOH etched devices show similar character exhibiting ideality factors ranging from 1.0-1.2, with $J_{S\ \text{As-Grown}} = 7.9\times10^{-9}$ A/cm^2 and $J_{S\ \text{KOH}} = 2.4\times10^{-9}$ A/cm^2. CAFM images of SVT429 showed highly localized leakage current at forward biases, contact potential reference, that slowly degraded with multiple scans (~ 5 - 8 scans). Increasing the bias increases the area of leakage current and the volume of current measured. Figure 19 - Forward and

Reverse Bias CAFM Images of SVT 429 shows the comparison of images taken at various tip to sample bias for SVT429 As-deposited.

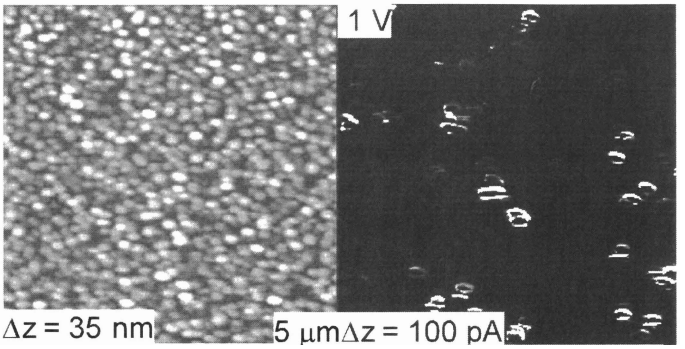

2 % Sat; Turning ON
LFD: 9.6×10^{7} cm^{-2}

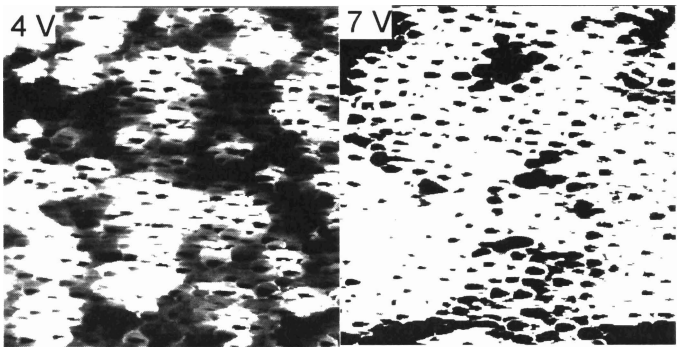

70 % Sat; Saturating
LFD: 1.4×10^{8} cm^{-2}

98 % Sat; Saturated

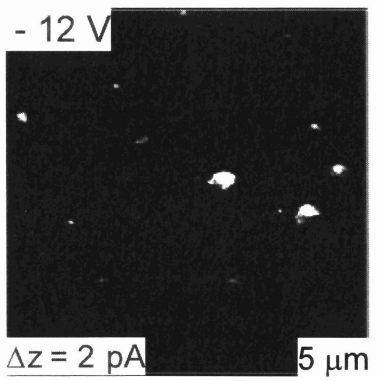

2 % Sat LFD: 4.8×10^{7} cm^{-2}

Figure 19 - Forward and Reverse Bias CAFM Images of SVT 429

Not all hillocks are electrically conductive; some pits selectively conduct on sidewalls or from the bottom. CAFM results confirm the results from Schottky diodes; SVT 429 has somewhat good transport properties with forward biases, a high series resistance, and very little leakage as compared to other samples. A more in depth comparison of KOH and as-grown devices will be presented in sections 3.2.1 KOH Etching for Device Preparation and 3.3 CAFM Measurements.

Capacitance measurements of SVT 429 are typical of MBE GaN on sapphire; there is a large built-in voltage and a high donor concentration, despite seemingly good electrical properties. Figure 20 - SVT 429 Inverse Capacitance Squared versus Applied Potential presents the inverse capacitance squared versus voltage data and Figure 21 - SVT 429 Donor Concentration versus Depletion Depth details the corresponding donor concentration versus depletion depth data.

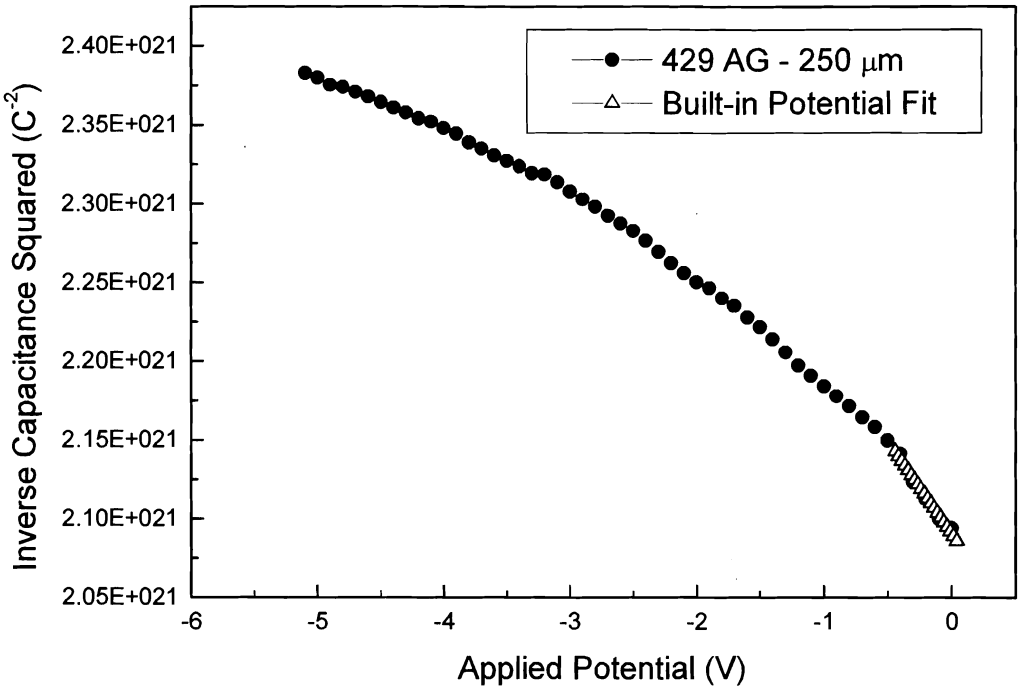

Figure 20 - SVT 429 Inverse Capacitance Squared versus Applied Potential

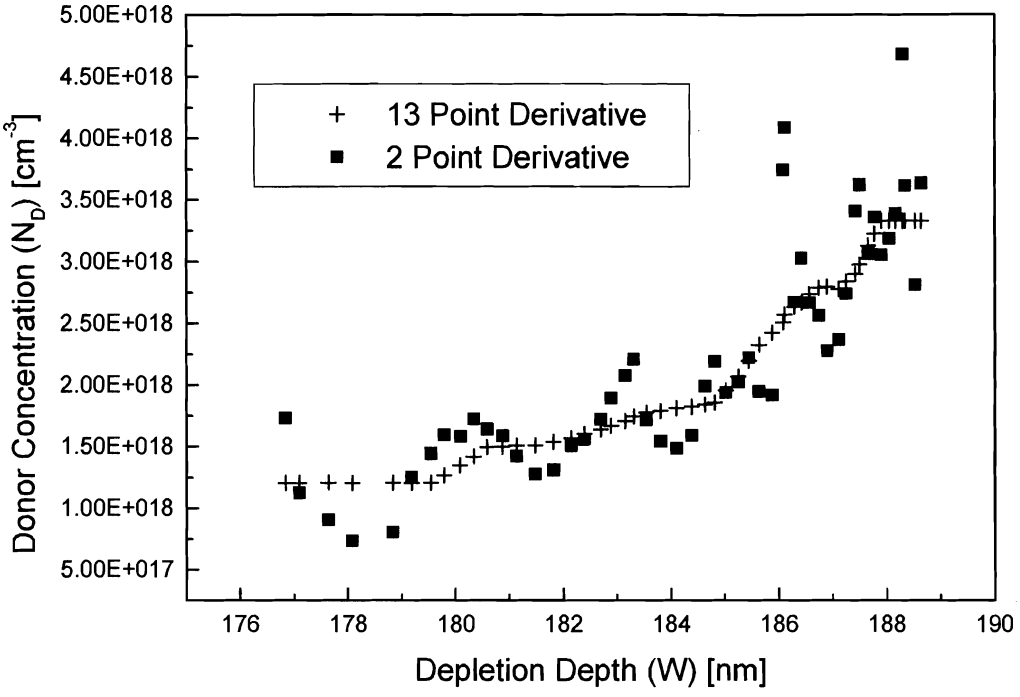

Figure 21 - SVT 429 Donor Concentration versus Depletion Depth

Smoothing of the capacitance data was necessary for the derivative operation, as demonstrated in the plot above capacitance data was extremely noisy. The depletion depths and donor concentration are on the verge of the TE / TFE transport regime, though this sample demonstrates little leakage.

3.1.2 SVT 750

Contrasting the previous low leakage, SVT 750 is a N-rich n-type Ga-polar MBE GaN thin film on sapphire with multiple quantum wells inserted in the GaN buffer layers

to reduce the threading dislocation density. The thin film layer structure and corresponding growth conditions can be seen as Figure 22 - SVT 750 Growth Structure.

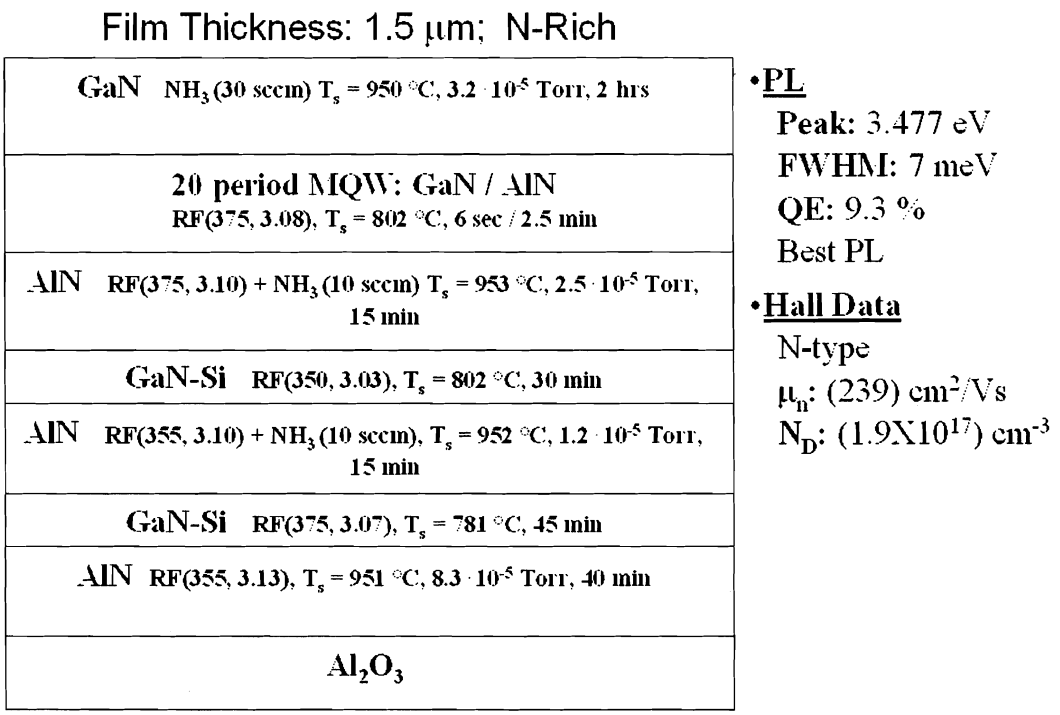

Figure 22 - SVT 750 Growth Structure

Ignoring the electrical characteristics, SVT 750 has the best PL results of all the MMDL samples and has a low donor concentration, as determined by Hall measurements. The mobility, 239 $cm^2/V \cdot sec$, cannot be trusted as there multiple quantum wells in the structure and parallel sheets of lower conduction about these interlayers can be a source of the high carrier velocity. This sample demonstrated significant leakage at forward and

reverse biases in Schottky contacts and in CAFM measurements, CAFM topography can be seen in Figure 23 - SVT 750 CAFM images at forward and reverse biases.

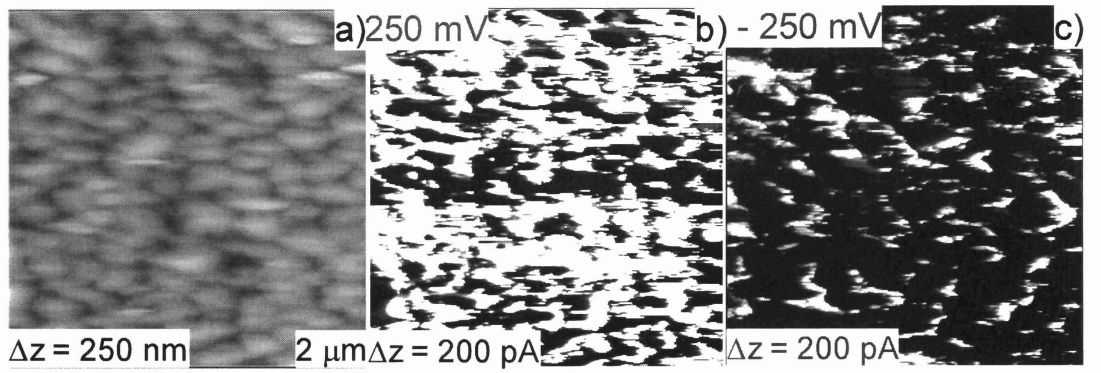

Figure 23 - SVT 750 CAFM images at forward and reverse biases

a) SVT 750 – As-Deposited Topography
b) SVT 750 – Forward Bias 0.25 V
c) SVT 750 – Reverse Bias 0.25 V

Current voltage measurements will be presented in section 3.2.1 KOH Etching for Device Preparation. To illustrate the presence of leakage centers in device contexts Figure 24 - SVT 750 Schottky Diode Image shows a CAFM image of a Schottky diode (lower left of panel a or b) and semiconductor layer separating diode and Ohmic contact.

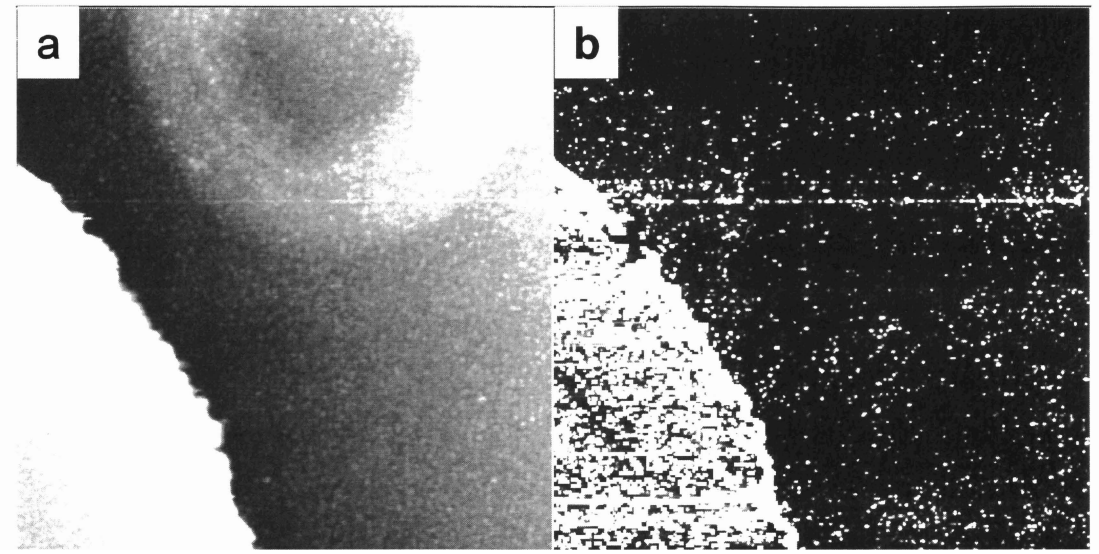

Figure 24 - SVT 750 Schottky Diode Image

a) Topography: Scale: 40 um^2 & Z-Range: 750 nm
b) CAFM image: Sample-tip Bias: 2.5 V, Pt-Tip, CAFM Module Current Range: 200 pA

3.1.3 SVT 889 and SVT 885

Two samples were selected to study as representatives of overgrowths on high quality HVPE templates. Figure 25 - SVT 889 Growth Structure details the growth structure for a high quality MBE overgrowth on the MIT Lincoln Labs HVPE template.

Film Thickness: 0.5 μm; Ga-Rich

GaN RF(375, 3.05), T_s = 583 °C, P = 9.4X10^{-6} Torr, 1 hrs
Nitridation RF(375, 3.05), T_s = 575 °C, P = 6X10^{-5} Torr, 10 min
MIT HVPE

Figure 25 - SVT 889 Growth Structure

The substrate temperature is much lower for the homoepitaxial depositions than for the sapphire substrates. CAFM and IV measurements revealed the sample had good electrical characteristics. The density of screw dislocations was determined from AFM measurements to be in the mid 10^8 range. Temperature profiling of the IV measurements is included as Figure 26 - SVT 889 As-Deposited - Schottky Diodes.

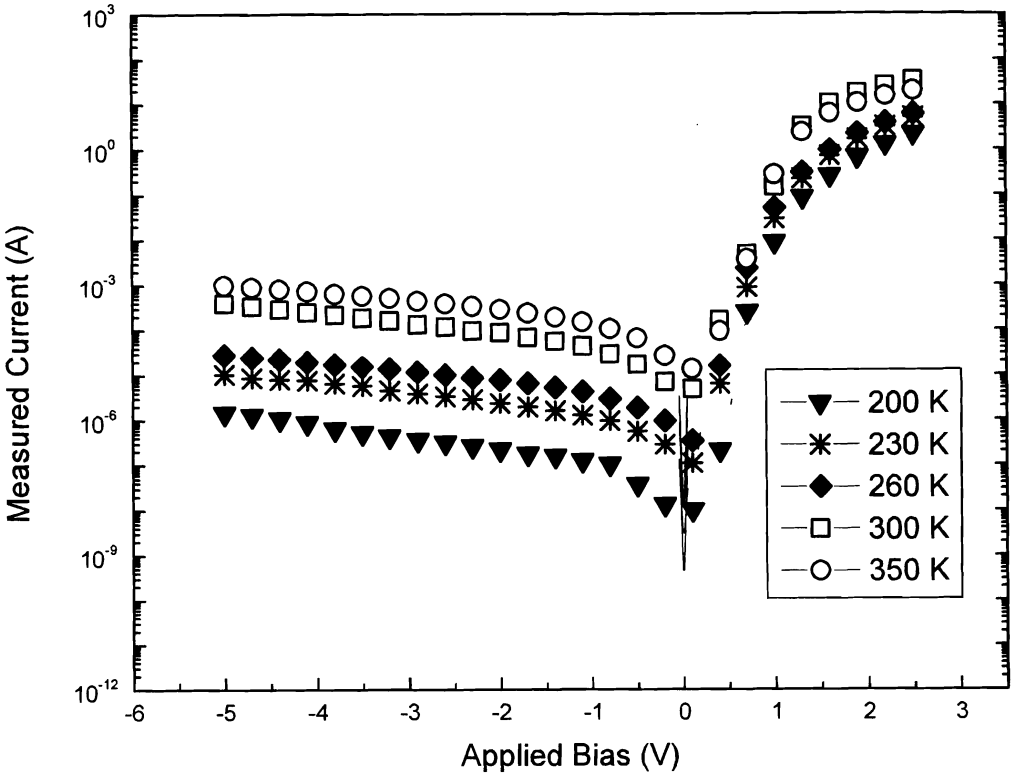

Figure 26 - SVT 889 As-Deposited - Schottky Diodes IVT's

A large variance can be seen in the shapes of the forward current responses and the leakage is consistently uniform between samples until around 200K. The homoepitaxial films' display higher conductivity in the saturation region of the forward response than the devices on sapphire. A comparison for the KOH etched Schottky diodes is included as Figure 27 - SVT 889 KOH Etched Schottky Diodes IVT's

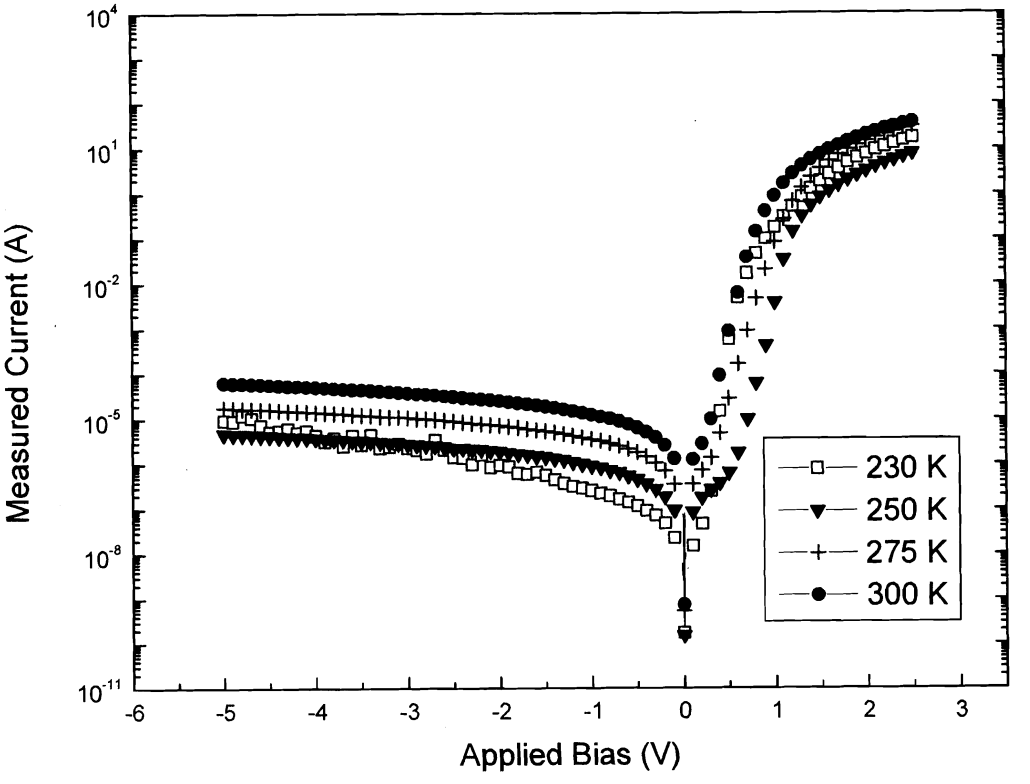

Figure 27 - SVT 889 KOH Etched Schottky Diodes IVT's

As temperature decreases, the leakage and anomalous conduction are diminished. The forward bias responses are mostly single slope, with a small field component at low biases evolving at lower temperatures. The reverse leakage is uniform and scales with temperature, until the onset of the noise floor (seen in the 230 K sample above –2 V).

Sample SVT 885 is a MODFET structure on a film equivalent to SVT 889. The MODFET heterostructure is a 20 nm-thick $Al_{0.12}Ga_{0.88}N$ layer on a 1 μm GaN buffer.

The spiral hillocks are evidence of a high density of dislocations with a screw component, density judged by AFM to be in the mid 10^8 range. The CAFM topography for SVT 885 is presented in Figure 28 - SVT 885 CAFM Current Topography.

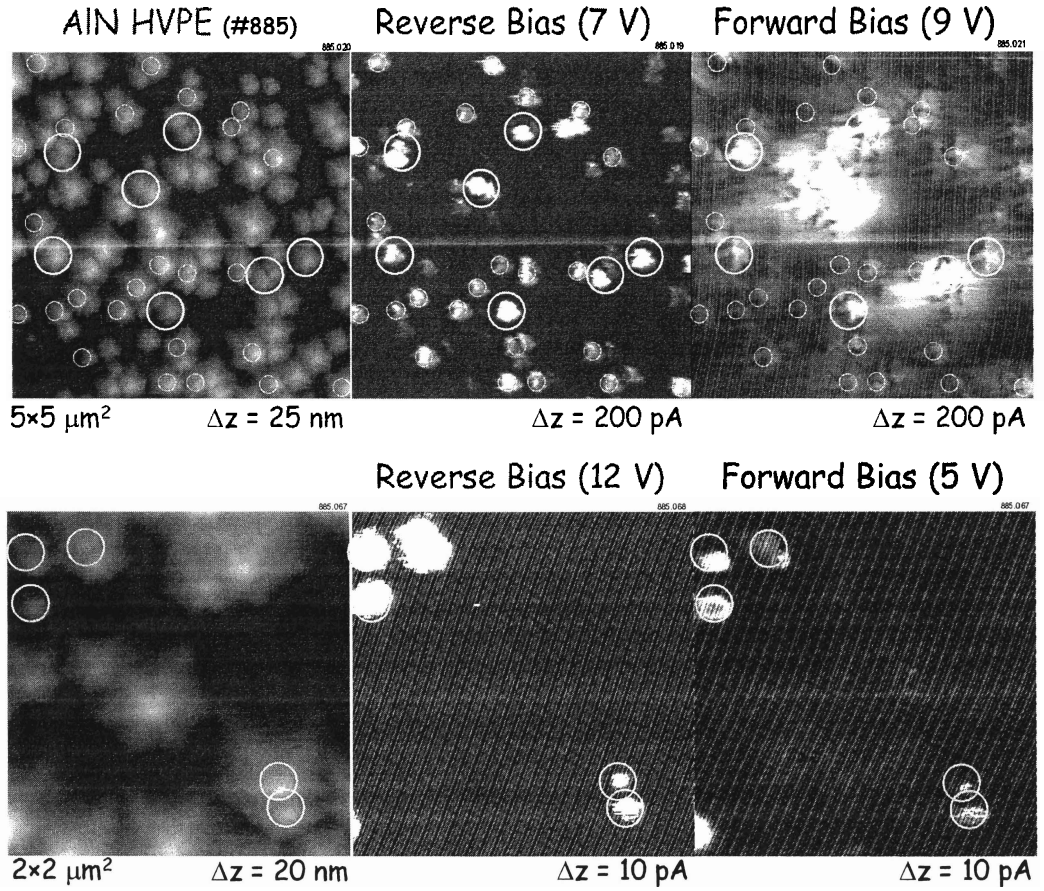

Figure 28 - SVT 885 CAFM Current Topography

Images above clearly show conduction centers at the top of the hillocks with massive barrier height lowering affecting the surrounding structures at forward biases. For reverse polarities, the conduction is more localized and pervasive.

3.1.4 SVT 1026 and SVT 1460

The films SVT 1026 and SVT 1460 were chosen to represent a new overgrowth technique for GaN on sapphire. A template film is grown by MBE, etched in molten KOH, and then a regrowth is performed by MBE. A comparison of the electrical characteristics of the two samples is included. The I-V characteristics from Schottky diodes on SVT 1026 AG are poor with J_S = 0.52 A/cm^2 and measured ideality factor of 3.4. All ideality factors were fitted to at least 0.5 V of the forward log(I) versus V plots. The SVT1026 KOH 5 min sample had 1 order of separation between +/- 1 V. The ideality factor for SVT1026 KOH 5 min samples was better than some of the SVT1026 AG, but still less than desirable (n > 2). CAFM measurements indicate less than 10^9 cm^{-2} leakage spots at forward and reverse bias of 2 volts, however as the bias is increased the density of conductive spots becomes greater than 10^9 cm^{-2}. The growth structure of SVT 1026 is similar to SVT 750 in the use of multiple quantum wells in the buffer to reduce the dislocation density, exact conditions are included as Figure 29 - SVT 1026 Growth Structure.

Film Thickness: 1.5 μm; N-Rich

GaN-Si NH_3 (20 sccm) T_s = 880 °C, 3.3 · 10^{-5} Torr, 2 hrs
20 period MQW: AlN / GaN-Si NH_3 (30 sccm) T_s = 861 °C, 10 min / 10 min
AlN-Si NH_3 (20 sccm) T_s = 874 °C, 3.3 · 10^{-5} Torr, 15 min
GaN-Si NH_3 (20 sccm), T_s = 889 °C, 3.9 · 10^{-5} Torr, 1 hr
AlN RF(350, 3.03), T_s = 880 °C, 1.2 · 10^{-5} Torr, 30 min
Al_2O_3

•**PL**
Peak: 3.478 eV
FWHM: 8.3 meV
QE: 10 %
Good, but strong DAP

Figure 29 - SVT 1026 Growth Structure

The leakage measured by CAFM in the As-Deposited samples is lower in this sample than in SVT 750, though KOH etching cannot obtain better Schottky diodes than etched SVT 750. A possible reason for this is SVT 750 had only a very thin region of point defects localized at the surface, where as SVT 1026 has a larger concentration of point defects throughout the thickness of the film. Detailed electrochemical techniques could definitively answer this question by providing information on each samples characteristic etch rates, and possibly in etching mechanism.

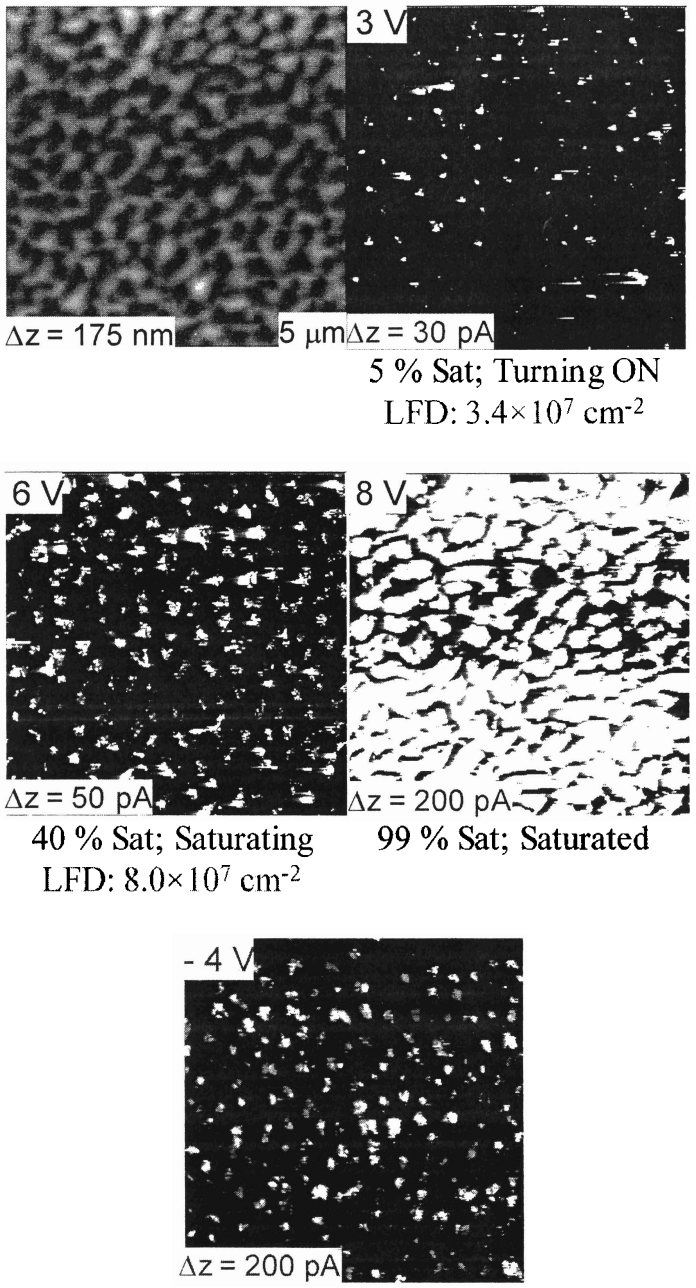

Figure 30 - SVT 1026 CAFM images at forward and reverse biases

Spotty conduction can be seen for low sample-tip biases, 6 V and –4 V respectfully. The leakage feature cross section increases drastically with increasing bias.

Sample SVT 1460 was analyzed by CAFM and with Schottky diodes. The CAFM measurements were inconclusive with behaviors reminiscent of HVPE or MOCVD samples. Conduction will appear, or fade out, midway through a topography scan, possibly due to limited or time dependent conduction capacity. The experiemental groups for both samples were comprised of three etch times proceeding device fabrication: 1, 3, and 5 minutes. As control groups, both SVT 1026 and SVT 1460 As-Deposited devices were fabricated in parallel with etched counter parts. The SVT 1460 KOH 1 min showed improvements in Schottky diode characteristics over SVT 1460 AG, though the SVT 1460 KOH 3 and 5 min showed degradation. Due to limited sample supplies, a second etch experiment at shorter times was unavailable. In both the longer etches, the ideality factor has increased, indicating an increase of the parallel conductive nature of the Schottky contact (the exact mechanism is unidentified). Long-term etching, 5 minutes, for the as-grown film showed some improvements in thermionic and leakage character, though for the regrown devices etched for 5 minutes there was marked degradation. Table 2 – SVT 1460 Current Voltage Results displays the thermionic parameters of interest for SVT 1460.

Table 2 – SVT 1460 Current Voltage Results

Sample	n	Js	Rs
1460 AG	2.19	1.64E-03	317
1460 KOH 1	1.85	2.15E-05	482

min			
1460 KOH 3 min	2.23	1.29E-04	366
1460 KOH 5 min	2.45	1.63E-01	539

3.2 Schottky Contacts

Current versus voltage curves were collected using a Karl Suss probe station and a Kiethley 4200 SCS parameter analyzer. The diode parameters were determined by fitting the current conduction mechanisms to collected diode's I-V curves. Potassium hydroxide etching is presented on Schottky diodes as a method for lowering the leakage current and improving the ideality factor in the Thermionic Emission conduction mechanism. As an extension to standard current voltage curves, the current and voltage of devices under long-term illumination demonstrated some anomalous behaviors that will also be presented.

3.2.1 KOH Etching for Device Preparation

In most MBE GaN films studied, the As-Deposited film was very rough and had a high density of threading dislocations. The point defect nature of the films was only study using photoluminescence. The PL results indicated multiple excitonic peaks and a large yellow luminescence band. To improve the devices a method was devised for reducing the extent of leakage in the Schottky contact using short term molten KOH etches prior to contact formation. It is proposed that by reducing the distribution of crystallographic faces then the probability for leakage manifestation is reduced. The

benefits are probably due to a purer crystallographic interface that will have less intimate connection of the extended defects to the Schottky contact, removal of near surface defects, and the reduced effects of induced barrier lowering.

Pamarico *et al.*, identified KOH etched pit side walls as having drastically increased conductivity over the surrounding c-plane surface using boron doped diamond tips with CAFM measurements. Measurements were taken on KOH etched MBE GaN grown on HVPE templates and sapphire substrates. The picture has been further clarified by recent CAFM measurements showing that current conduction cannot only come from pit sidewalls, but plateaus, hillocks, and bottoms of pits as well. This indicates that KOH etching can help improve device characteristics in some range of etch conditions, notably molarity, temperature, light, agitation, and buffers/catalyst. Electrochemical etching of films can provide a quantitative and consistent method for device preparation.

Molten KOH has been reported to be a reaction-rate limited etching that attacks several crystallographic planes, {10-10} and {10-1-1}, at the sites of defects.[163] The resultant film is relatively flat with a distribution of several crystallographic facets, the area of which is proportional to the density and depth of the etch pits. Due to the symmetry in etching, the pit sidewalls are composed of [10-10] and [10-1-1] planes. KOH is well known to rapidly etch N – polarity GaN, etch rates exceeding 1 μm/s. [164] The particular etch rate of a material depends on the solution parameters and the film properties. Highly defective Ga-polar films can have etch rates exceeding 4 μm/s (1 μm film disappearing in < 15 secs).

The exact mechanism of KOH etching involves forming an oxide layer at the surface, corresponding to introduction of a Ga vacancy in the film, followed by rapid dissolution of gallium oxide into KOH solution.[165] KOH treated Ga-polar films demonstrate a shift in the barrier height to lower values, indicating the presence of an oxide, induced barrier lowering, or an interfacial layer has been removed.[166] In certain cases, such as HVPE templates, the substrate may be attacked by the KOH. To avoid this the sample can be floated on the surface of the etchant, or the sample can be encapsulated with a protective material with the surface exposed. Alternate etching methods include some form of electrochemical or UHV etching techniques.

Utilizing KOH etching in device processing was conducted in Molten KOH, 212 °C 85% by weight KOH. Typical etch times were on the order of 10 seconds for films with the maximum defective composition and 30 seconds to 2 minutes for higher quality films. KOH Etching of films improves the IV characteristics for several possible reasons. First, the c-plane of the crystal is exposed and second pits are introduced where there were significant shifts in the chemical potential of the crystal. In attacking the areas with increased point defects, and consequently a shift in chemical potential, the net quality of material in contact with metal, either from an AFM tip or Schottky device, improves drastically over the as-grown case. Figure 19 - Forward and Reverse Bias CAFM Images of SVT 429 and Figure 23 - SVT 750 CAFM images at forward and reverse biases, demonstrate the marked improvement in surface structure and electrical characteristics with KOH etching.

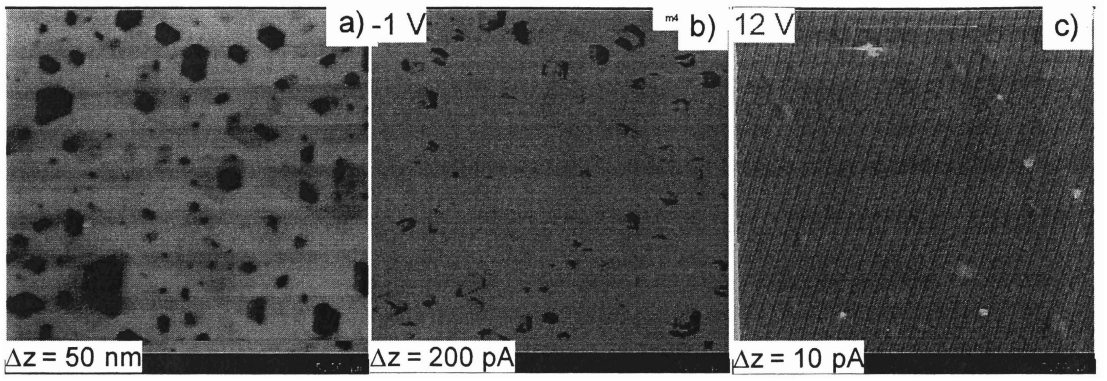

Figure 31 - SVT 429 KOH Etched

a) As-Etched
b) CAFM Module – Forward Bias 1V
c) CAFM Module – Reverse Bias –12V

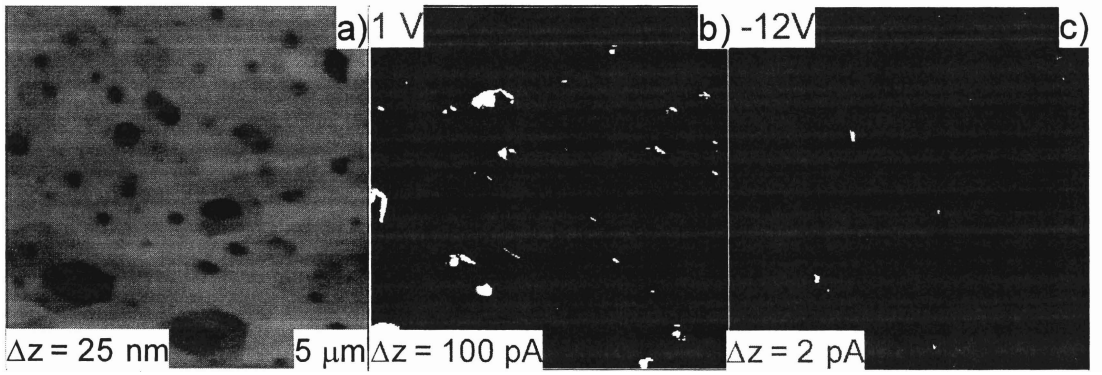

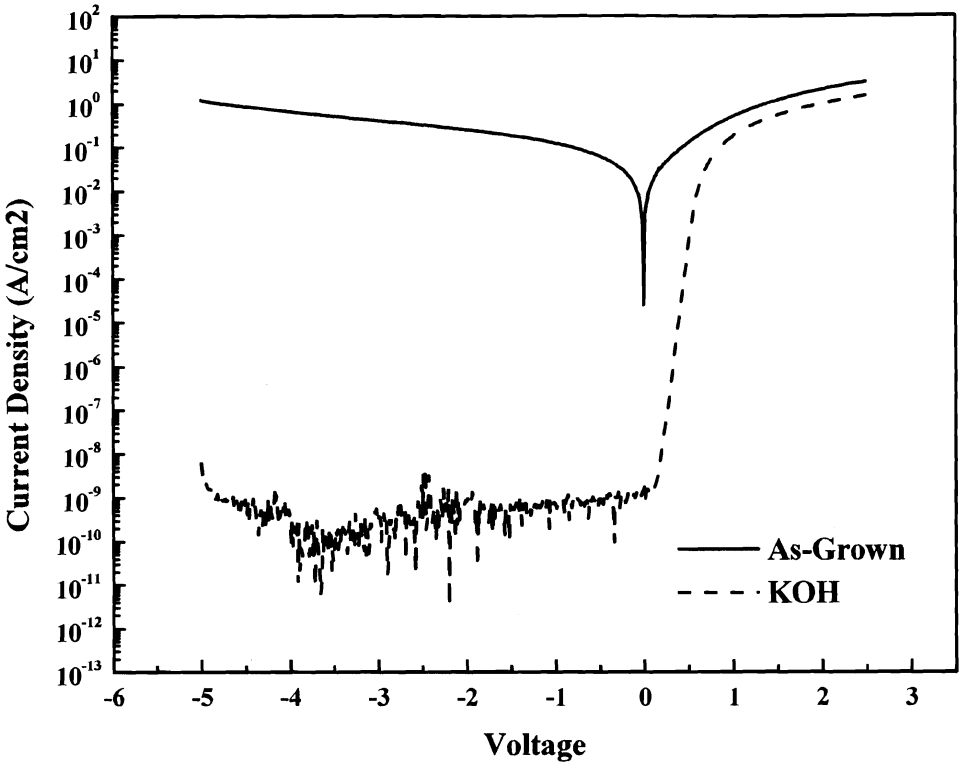

d)

Figure 32 - SVT 750 KOH Etched

a) As-Etched
b) Forward bias 1V
c) Reverse Bias –12V
d) Schottky Diode Current Voltage Curve

The proceeding two sets of figures demonstrate the improvement in electrical characteristics typically experienced with KOH etching. The diodes fabricated on SVT 750 had the best electrical characteristics out of all of the samples measured during these studies, see Figure 32 - SVT 750 KOH Etched panel d.

Experiments were conducted involving various concentrations of KOH at varying temperatures. It was found that 12 M KOH just below boiling is successful at attacking the defective regions of GaN, while producing a mostly similar surface as compared to molten experiments. The benefits of lowering the concentration of the etchant are slightly longer etching times and much safer working conditions. Below 12 M there were selective oxidation regions, evidenced in circles on the sample, and the etch pits were not clearly defined; agitation may have improved this aspect but was not explored. The material etched with lower than 12 M KOH was more reminiscent of hexagonal symmetry in a heavily pitted, or semi porous, material. No cross sections were performed so the bulk character of the film is speculation from top down AFM images. Molten KOH etching was performed for all of the devices and CAFM samples presented in this study. Figure 33 - Surface Roughness vs. Ideality Factor and Figure 34 - Surface Roughness vs. Saturation Current demonstrate the improvements in devices' ideality factors and saturation as a function of surface roughness after molten KOH etching, open shapes are values after etching and closed shapes are before etching.

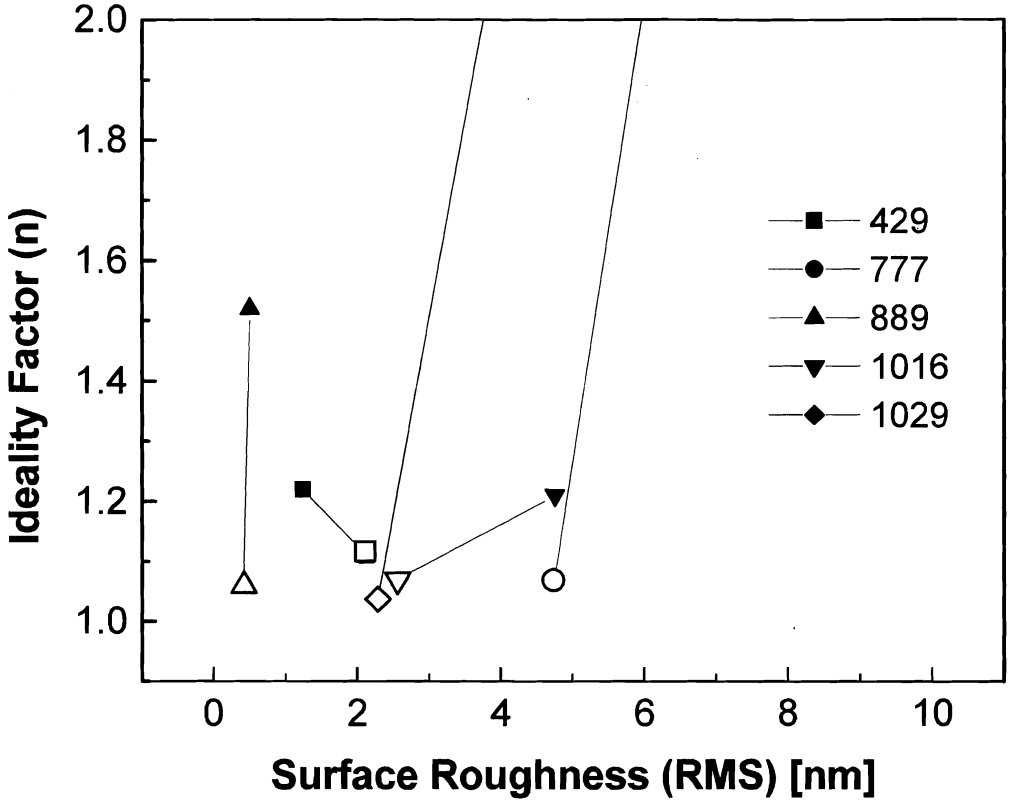

Figure 33 - Surface Roughness vs. Ideality Factor

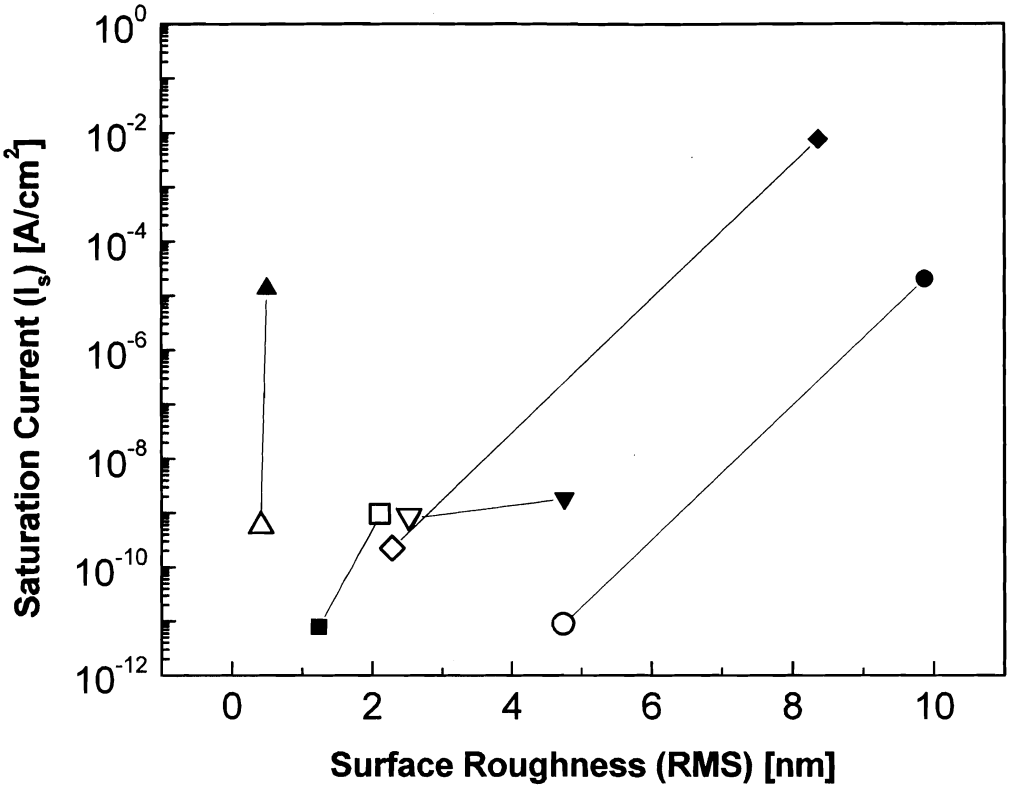

Figure 34 - Surface Roughness vs. Saturation Current

The ideality factor improved regardless of the change in surface roughness, noting only one sample was rougher and probably overetched. The leakage current was directly correlated to the surface roughness for the samples investigated. This seems to be a general trend for the MBE GaN devices studied at MMDL.

A set of ammonia grown MBE MODFET's structures on sapphire, R6565, demonstrated similar improvements in device quality with low molarity KOH etching.

High molarity etching for 15 seconds created a poorer Schottky contact and abysmal drain-source characteristics, probably due to the removal of the capping layer. The low-molarity etched MODFET's demonstrated transconductances in the range of 100 ms/mm with maximum drain current I_{DS} of 20 mA and knee voltage of approximately 6.5 V. The improvements in MODFET characteristics were attributed to a decrease in the surface anisotropy with applied etching conditions that in turn set the stage for good contacts with low alloying and MIGS behavior. With good contacts, the underlying channel current could be controlled. The following two figures, Figure 35 - R6565 As-Deposited MODFET Drain Source Characteristics and Figure 36 - R6565 Low Mol. KOH Etch MODFET Drain Source Characteristics, compare the As-Deposited and Low Molarity KOH MODFET samples' drain current responses.

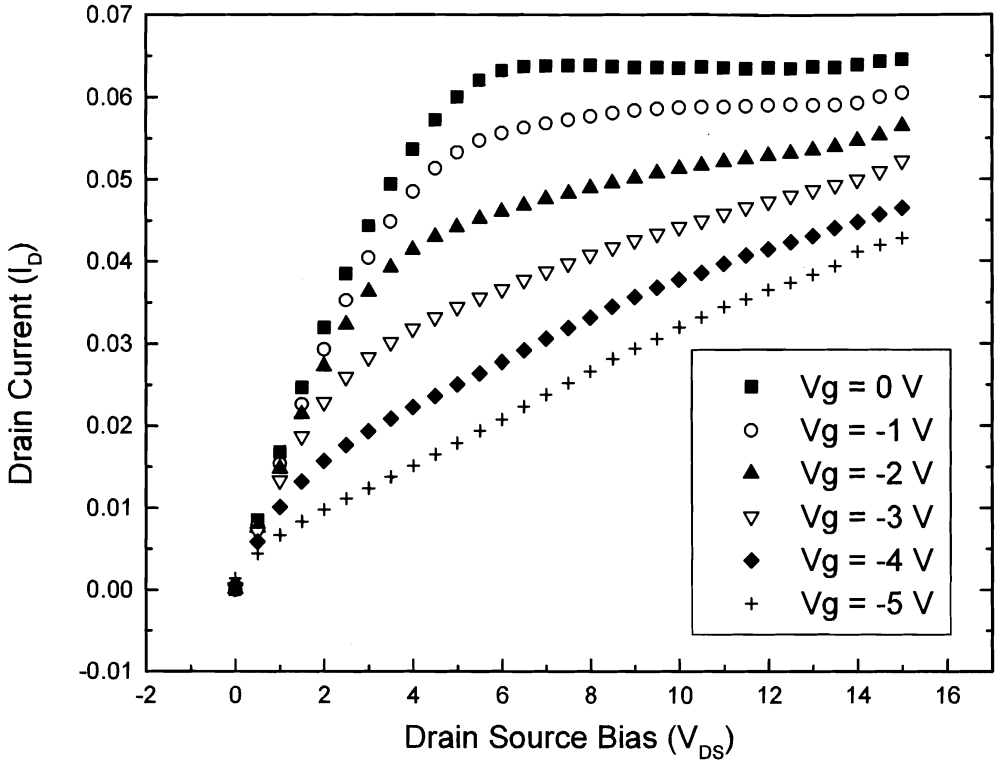

Figure 35 - R6565 As-Deposited MODFET Drain Source Characteristics

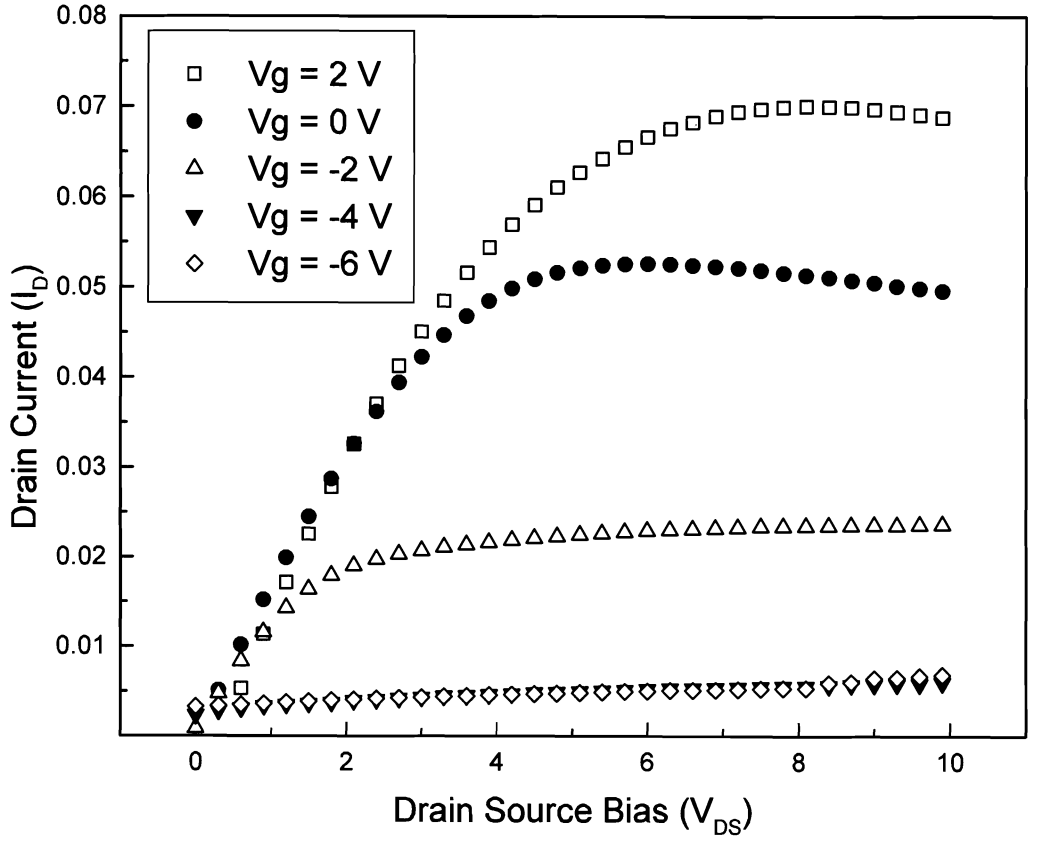

Figure 36 - R6565 Low Mol. KOH Etch MODFET Drain Source Characteristics

The low molarity KOH Etch sample has a reduced contribution to the drain current curves from leakage current, evidenced by the nearly flat response of the drain current in the saturation region. The low molarity KOH etched sample didn't have a significantly higher transconductance or drain source current than the as-deposited chip, but the

uniformity and device yield increased. The results from 2 nearly comparable 100 μm and exactly comparable 310 μm devices are given in table 3.

Table 3 – R6565 As-Deposited and KOH Devices

Sample	Gate Width	R_{ON}	V_{knee}	I_{DSS}	Normalized G_{max}	G_{max} Voltage	$V_{pinch\ off}$
R6565 - AD	100	133.3	6.0	2.3E-02	102.0	-2	-4.5
R6565 - AD	310	57.5	6.1	7.9E-02	80.6	-3.2	-5.4
R6565 - KOH	100	177.0	5.0	1.9E-02	90.0	-1.5	-4.0
R6565 - KOH	310	66.7	4.5	5.0E-02	96.8	-1.2	-4.0

The on resistances for the KOH devices are slightly higher and the knee, max transconductance, and pinch-off voltages are lower by about a volt. The transconductances and max drain currents of the As-Deposited samples are slightly higher, but at the cost of acceptable device characteristics. Preparing MODFET's with KOH etching may be a viable method for improving device quality, but must be verified on higher quality samples.

3.2.2 Curve Fitting Current Mechanisms on Macroscopic Contacts

To gain a better understanding of experimental data, curve fitting was independently performed using Excel and MATLAB, for both current spectra and mobility data. A program was written in MATLAB for mobility data analysis, while Excel and MATLAB were used for the current spectra. Embedded loops were utilized in

constructing the error function to tune the simulation curves. The error function was defined in the Excel spreadsheet as a column of data resultant from the specific theoretical function and based on the dependent variable, the measured current in the case of current spectra. Minimization of the MISFIT, defined following, was the target of the embedded loops.[50]

Equation 54 - MISFIT Expression

$$MISFIT = abs\left[\ln\left(\frac{Experimental\ \ Data}{Calculated\ \ Data}\right)\right]$$

The MISFIT should be zero in the case of a perfect fit, ln(1) = 0.

The combination of Excel spreadsheets and Visual Basic Macros allowed sequential comparing of many theoretical functions to the experimental data. Visual Basic was used to create the tuning ability in the theoretical expressions. The defined tuning variables include a slope adjustment (m) and intercept (b) correction for the most simplistic exponential case. A given conduction mechanism curve can be delineated into either constant or nonconstant slope (on a logarithmic graph). The constant slope conduction mechanisms have an exponential dependence on voltage, such as Hopping or TE. The nonconstant slope mechanisms are very distinct in produced curvature, such as FE or Schottky conduction. Certain mechanisms may require additional tuning parameters. For additional tuning parameters, the user can create an array of a specific mechanism with incremental perturbations to the additional tuning parameter fixed in each expression of the array. In the embedded loops, a panel of 16 combinations of weights on the slope and intercept were constructed. If an adjustment was favorable, an

embedded loop would test exponential deviations to determine if a larger step was more preferable. If the panel was not affective at replacing the current error function on the spreadsheet, the tuning variables change would begin to decay. After a specified number of loops, the program would move to the next expression or column on the spreadsheet. Typical convergences of the MISFIT function for valid expressions were on the order of 10^{-6} to 10^{-8} MISFIT per data point. Figure 37 - Curve Fitting Program GUI shows the curve fitting process in a visualized manner.

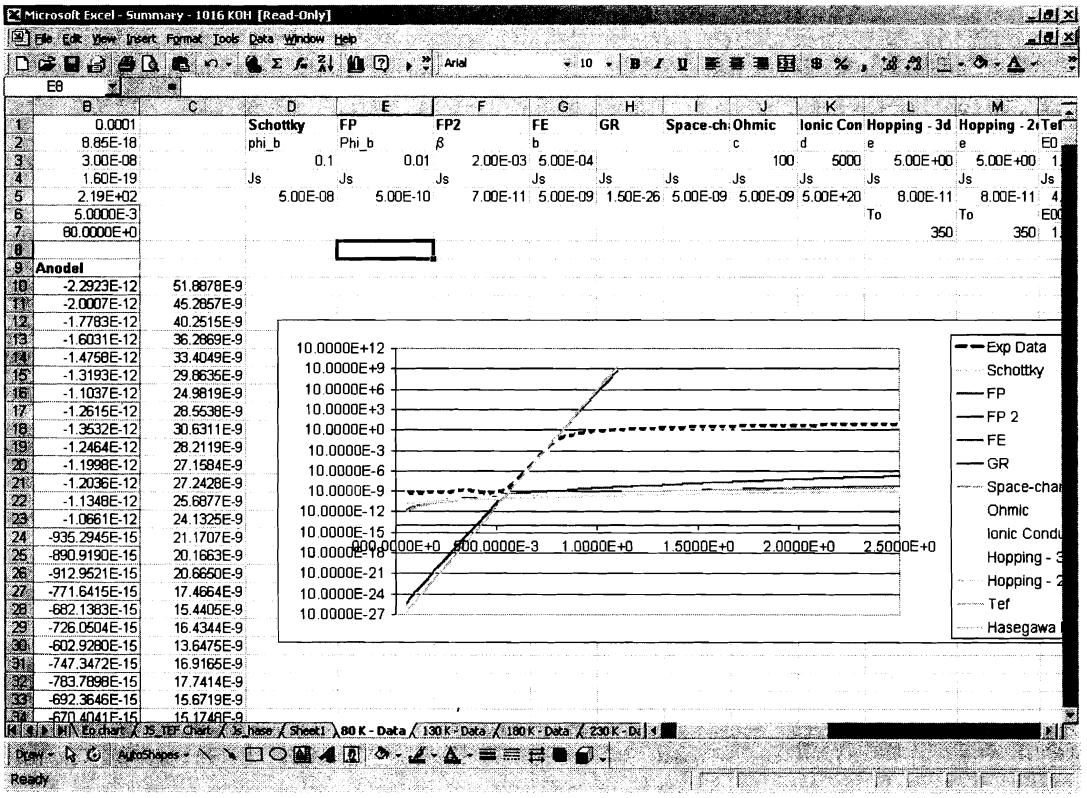

Figure 37 - Curve Fitting Program GUI

A user interface was added to the worksheets to allow easier access to changing the fundamental tuning properties, such as number of worksheets, number of expressions to be fit, tuning weights, loop limits, among others. An offset was necessary for the large potential shifts seen in CAFM measurements. The offset was implemented on a region basis where all of the theoretical expressions in a given region would have the potential shifted by a user-defined bias. The bias was not used as a tuning parameter. A copy of the program and a set of instructions for the program have been left in the care of Dr. Baski.

Additional features that were not added to the curve-fitting program, that would have increased the utility drastically, are described. Convergence times for solutions were highly dependent on the amount of free memory and processor speed. In the current form, the experimental data would each comprise a worksheet within a workbook, and each mechanism would be fit to the experimental data. When there were a large number of curves, the workbook size would become imposingly large. Alterations to the program would alleviate this problem by removing the given experimental data set, i.e. the spreadsheet, into another workbook, close the large workbook cataloging all the data to be analyzed, and perform the curve fitting in a reduced overhead environment of a single worksheet. This would drastically increase the convergence times of larger data sets and make the next extension a possibility. Another feature that would require a little more effort would section the data according to independent variable relationships. Before the mechanisms are currently tuned, the user must define the boundaries on the spreadsheet for the given mechanism. This equates to guessing a region, running the program, and

correcting the boundaries, then rerunning the program, requiring many time consuming iterations. Two approaches could be utilized in correcting this deficiency; first, the program could sectionalize the data according to independent variable permutations and assign corresponding boundaries to the appropriate mechanisms. The other option is for the user to guess an initial region and allow the iterative looping process to determine the best fit, and redefine the region based on fitting results. The first method is preferable, as it should allow faster convergence times and results that are more reliable. The main goal is to select the conduction mechanism that will fit the largest region of data with the highest accuracy. Results form the curve-fitting program for SVT 889 can be seen in Figure 38 - SVT 889 As-Grown Current Voltage Curve at 270 K and Figure 39 - SVT 889 KOH Current Voltage Curve at 275 K, for 250K and 275K, respectfully.

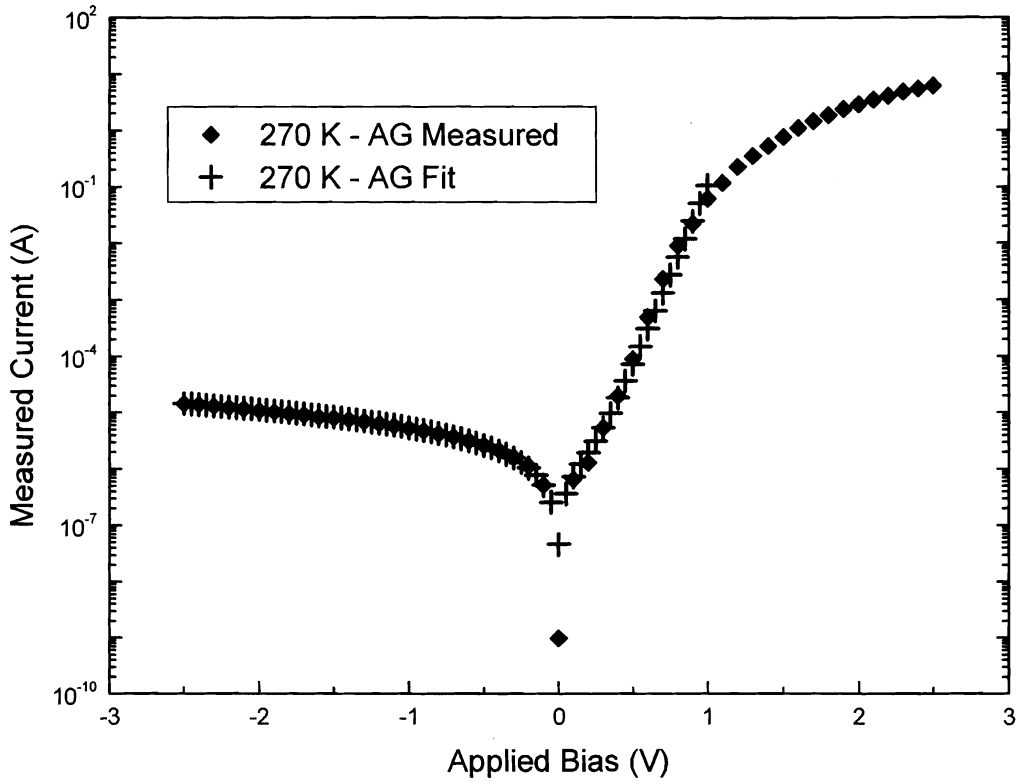

Figure 38 - SVT 889 As-Grown Current Voltage Curve at 270 K

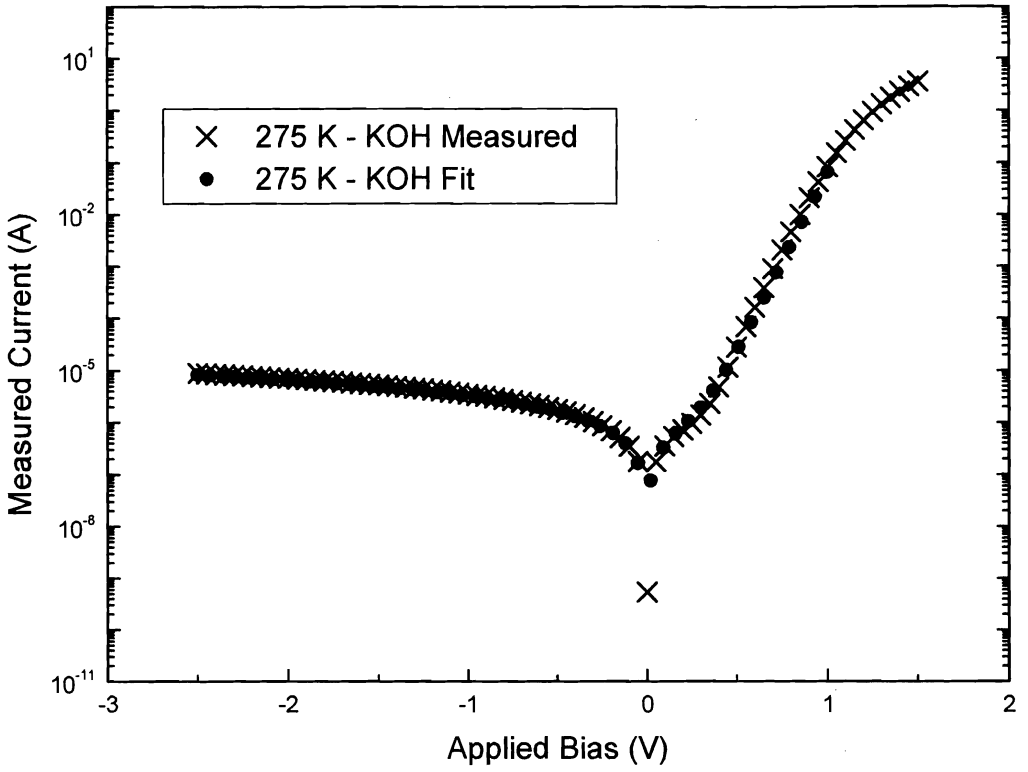

Figure 39 - SVT 889 KOH Current Voltage Curve at 275 K

The leakage current decreases with decreasing temperature, and the forward bias conduction becomes more thermionic in nature. As the temperature decreases the activation of native defects decreases, effectively lowering the carrier concentration and tunneling behavior at the interface. At low forward bias, less than 0.5V, a field related conduction mechanism that can be seen at 270 K in the KOH etched sample. After fitting a series of data points, the fitting parameters for the specific mechanisms, namely the

saturation current, are plotted as a function of the parameter's relationship to temperature. This allows the researcher to determine intrinsic material parameters, such as the Richardson's constant and barrier height by using the saturation current from thermionic data. The following figure, Figure 40 - SVT 889 Arrehenius Plot of Saturation Current, presents an Arrehenius plot of the saturation current and relevant fitting / parameter extraction information.

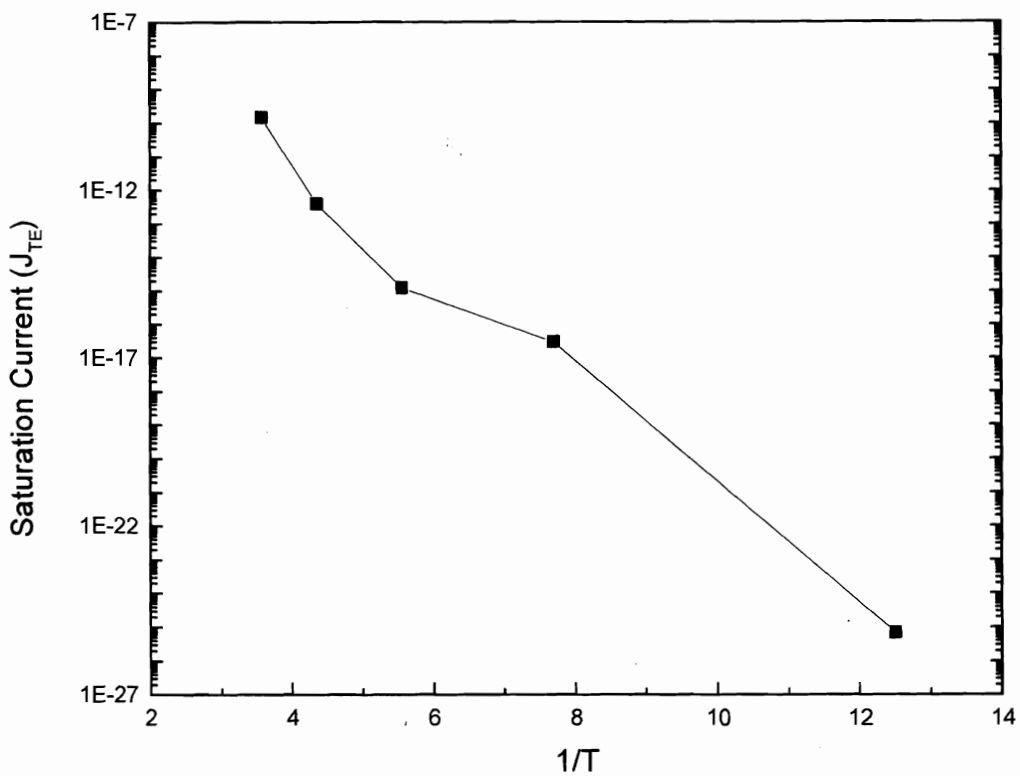

Figure 40 - SVT 889 Arrehenius Plot of Saturation Current

Using the expressions in section 2.2.2 Current - Voltage Measurements, the slope and y-intercept of the expression will reveal information about the barrier height and Richardson's constant for thermionic expressions. The proceeding Arrehenius plot was for thermionic field emission, which reveals different information about the metal-semiconductor interface than the thermionic expression.

Another form of current voltage curve analysis is an activation energy plot. Curves are constructed by plotting the current at a given bias value as a function of temperature. Minimums in the curves identify defect activation energies. This method of point defect identification is vastly inferior to DLTS measurements. A sample activation energy plot for SVT 889 KOH etched device is included as Figure 41 - Activation Energy Plot for SVT 889 KOH Etched Device.

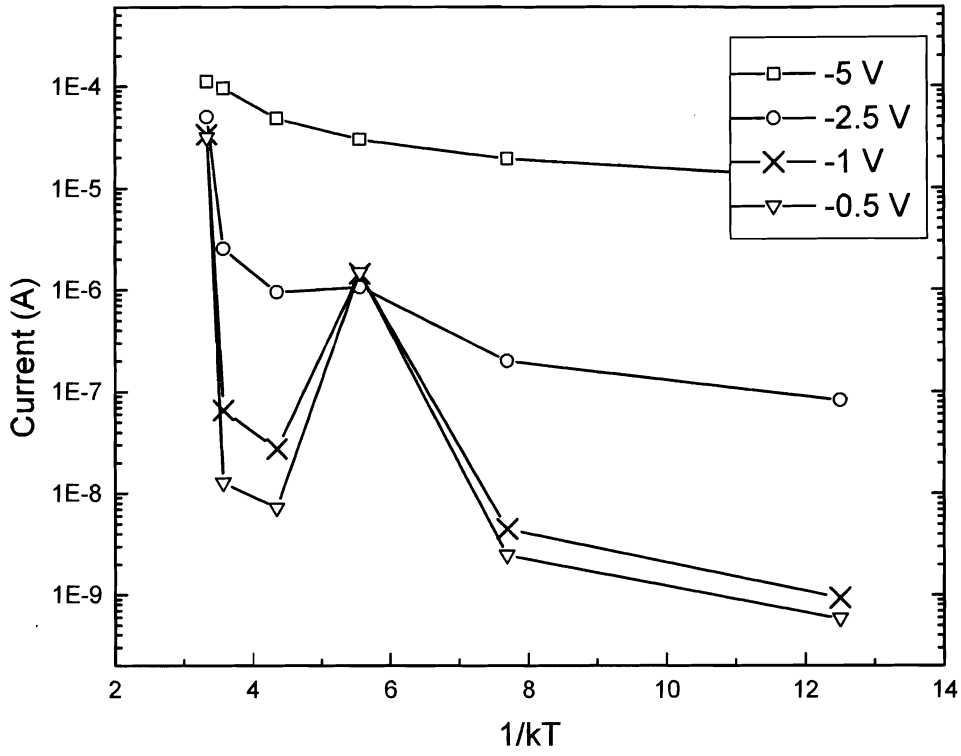

Figure 41 - Activation Energy Plot for SVT 889 KOH Etched Device

A program was also written to crawl collected data. The program would open a directory and catalog the contents onto a table of contents page. Using the table of contents for experimental IV data the program would then create a page for each workbook and analyze the data accordingly for ideality factor, series resistance, saturation current, and catalog the current at several potentials. The output pages were then manually collected and used to create a database. The database provided a method for correlating the Schottky characteristics to the growth conditions, among other results.

Another advantage of this method is that it could be used to provide maps of the integral characteristics of the film and the local sensitivity. A very powerful tool could be created by linking the curve-fitting program with the cataloging program; the current mechanisms could be devolved for any number of diodes in a directory. This method of fitting analytical expressions to collected data would be easily applicable to a number of other applications including: electrochemistry, x-ray, photoluminescence, mobility measurements, etc.

To provide a feeling of the spatial distribution of Schottky parameters the second program was used to process the Schottky IV curves that were collected. The results for sample SVT 1460 KOH Etched 1 min will be presented. The following three figures demonstrate the independent nature of contact transport properties represented by the Thermionic Emission expression presented in section 2.2.2.1 Thermionic Emission. Figure 42 - Ideality Factor vs. Diode for SVT 1460 1 min etch is a map of the Ideality Factor as a function of the diode's location on a test chip; for example, the diode in column 14 and row 2 shows an unusually high ideality factor, but low saturation current and high contact resistance.

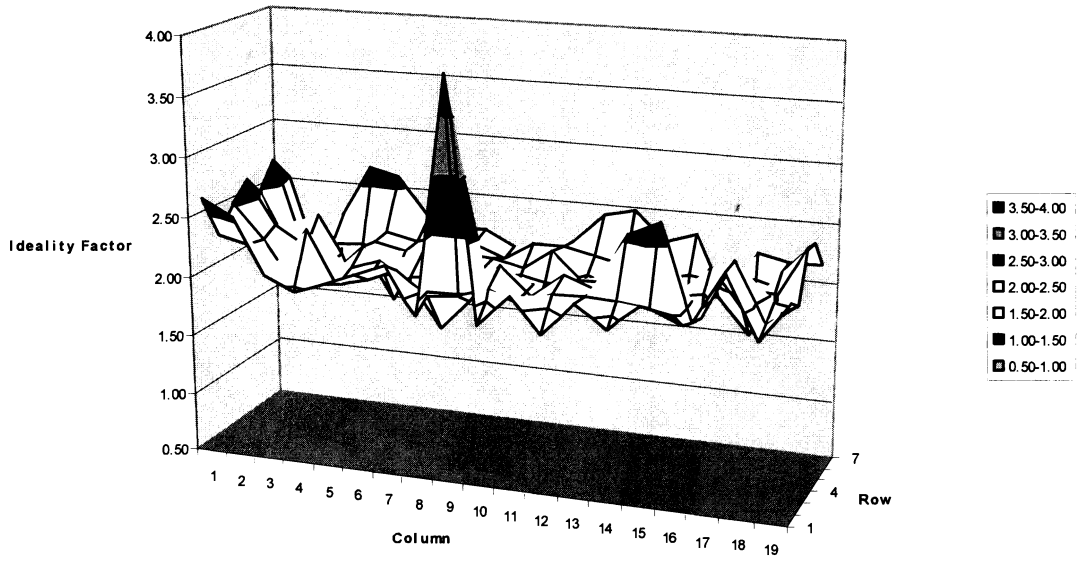

Figure 42 - Ideality Factor vs. Diode for SVT 1460 1 min etch

The highest ideality factor is over 3.5 and the average value is around 2.4, larger than recombination-generation mechanisms with a characteristic ideality factor of 2. The saturation current as a function of diode position on the test chip is presented in Figure 43 - Saturation Current vs. Diode for SVT 1460 1 min etch.

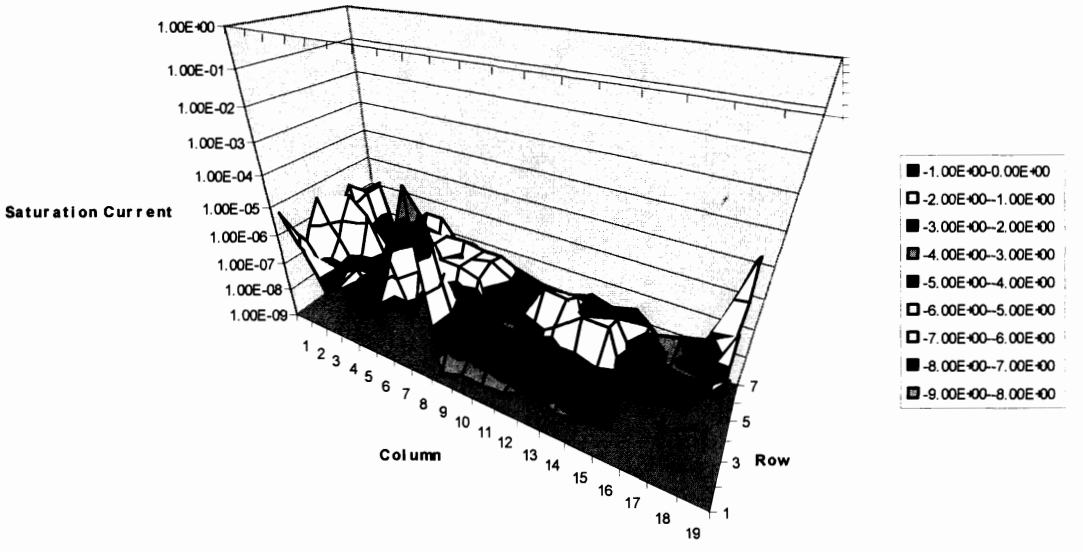

Figure 43 - Saturation Current vs. Diode for SVT 1460 1 min etch

The saturation current is not directly correlated to the ideality factor, common of the diodes investigated at MMDL. The best devices exhibited saturation currents below 10^{-9} A at –5V for a 75 μm Ni/Au Schottky contact with approximately 150 μm separation from diode to Ohmic contact (SVT 750 KOH Etched). Figure 44 - Series Resistance vs. Diode for SVT 1460 1 min etch represents a map of the series resistance of devices on SVT 1460 with a 1 min KOH etch.

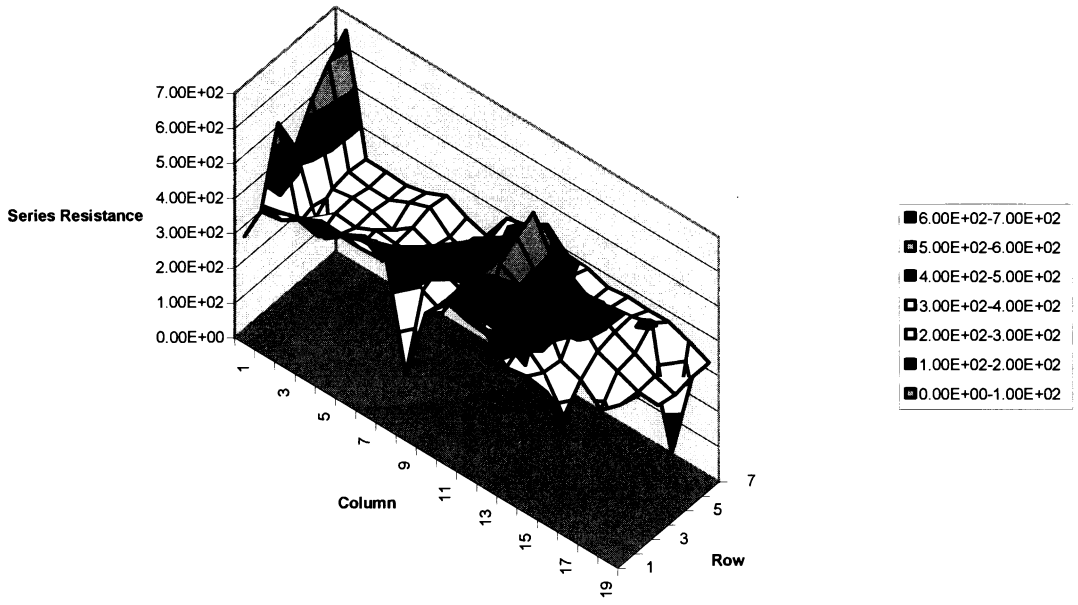

Figure 44 - Series Resistance vs. Diode for SVT 1460 1 min etch

The series resistance is also independent of the two afore mentioned parameters, suggesting that the conduction exhibited in this etch-regrowth sample is not of thermionic character and there is widely varying film properties.

Curve fitting is an invaluable tool in determining the nature of anomalous current conduction. In order to accurately determine the exact source of the excess current it is necessary to perform curve fitting as a function of temperature within a bias range encompassing a saturation region. The potential boundaries defining the transition from one conduction mechanism to another mechanism will fluctuate with temperature. If to small of a potential range is used, numerous conduction mechanisms could potentially appear to be appropriate.

In a given Schottky contact, conduction will assume the form of some exponential as a function of potential, field, or both. The form of the exponential is a result of the underlying carrier physics and defect structure of the system. Ideally the conduction measured in a device is a result of transport over the barrier, though bulk emission mechanisms, surface and defect mechanisms must be examined. If an anomalous conduction response is observed and point defects are the culprit, the conduction will most probably be of the Field emission, Poole-Frenkel, or Hopping Type. The spatial and energetic positions of the defects determine the type of conduction. Field emission is the result of a poorly formed barrier, from either excessive ionized donor concentration or MIG's. Adding to the complexity of the metallic Schottky interface, a continuum of states can form at the metal-semiconductor interface, termed Metal Induced Gap States (MIGS). In the case of mobility-limited conduction, the transport through the bulk or surface region limits the volume of conduction. There are several manifestations of mobility-limited conduction, of which hopping conductivity is the most common.

3.2.3 IV Measurements on Schottky Contacts under Monochromatic Illumination

Utilizing a monochromatic filter with a mercury UV light source and IV probe station the electrical response of Schottky diodes was characterized as a function of illumination. In order to measure the impact of the illumination, the current and potential of the contact was measured versus time as a function of illumination energy. The thermal energy of the contact is inarguably a function of the defect structure and material

quality. The open circuit potential, and current exchange with probes measuring open circuit potential, are a result of the random thermal motion of carriers. Fluctuations in the current and potential would indicate the presence of a significant density of charge centers in a low frequency acoustic resonance with applied illumination, or a situation of competing defect centers that cause the exchange of measured charge. The data presented is more to demonstrate a technique that could be applied to C-AFM measurements to better understand the micro-defect structure.

In the experimental setup, the anode and cathode are grounded with the current and voltage measured in and out of the contacts. For the circuit to be in equilibrium, no electromotive forces can be applied to the circuit. If a current or fluctuating potential is still being measured then the free energy of the experimental setup is being measured. In absolute darkness, thermal equilibrium, and acoustic isolation the current and voltage fluctuations would be a result of the characteristic defects and microstructure of the semiconductor. Introduction of illumination would theoretical excite the defect states present, preventing occupation of defect sites below a given photon energy. The illumination energy would also allow the exchange of carriers between the valance band and any defect states, between defect states, or between defect states and the conduction band, primarily as long as the transition energy is less than the illumination intensity. The other requirements localization and cross-section requisites defined by quantum mechanics. Assuming there is a sufficient density of defects in sufficient distribution of localization in the energy and physical structure of the material are met, a proof based on absorbed power from a resistance will be presented. This exercise is presented as a first

order approach for understanding the fluctuating power spectrum of an illuminated Schottky diode. Following, Figure 45 - Monochromatic Forward Current Response, demonstrates a typical IV response during monochromatic illumination. Figure 46 - Power Illumination Dependency – SVT 889 and Figure 47 - Time Dependency of Luminescence – SVT 1016 demonstrate the power and current behavior of illuminated devices.

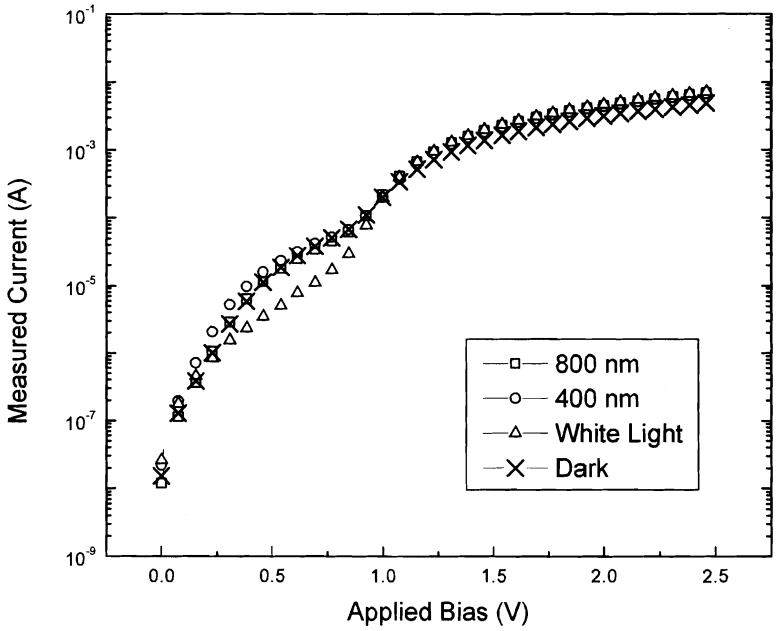

Figure 45 - Monochromatic Forward Current Response – SVT 1016

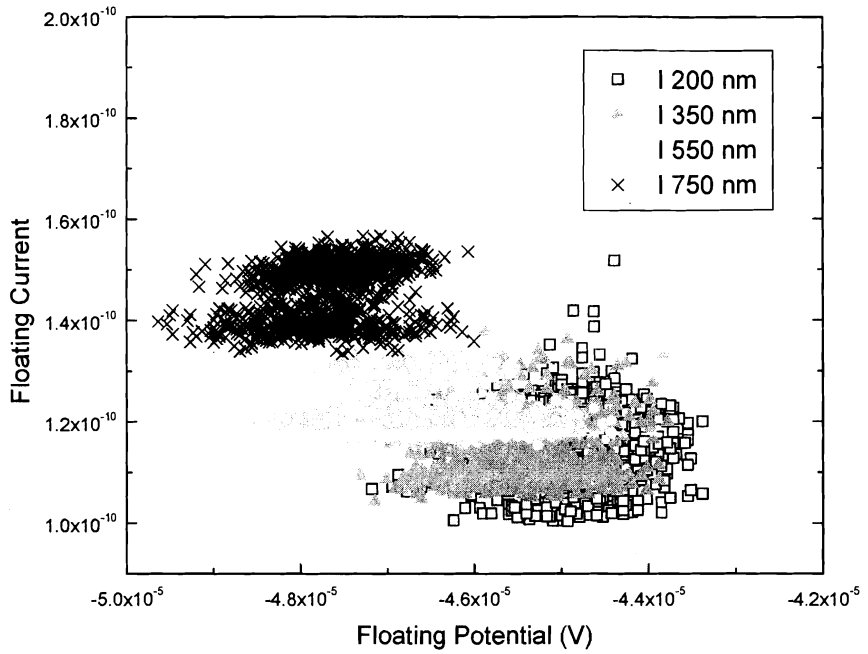

Figure 46 - Power Illumination Dependency – SVT 889

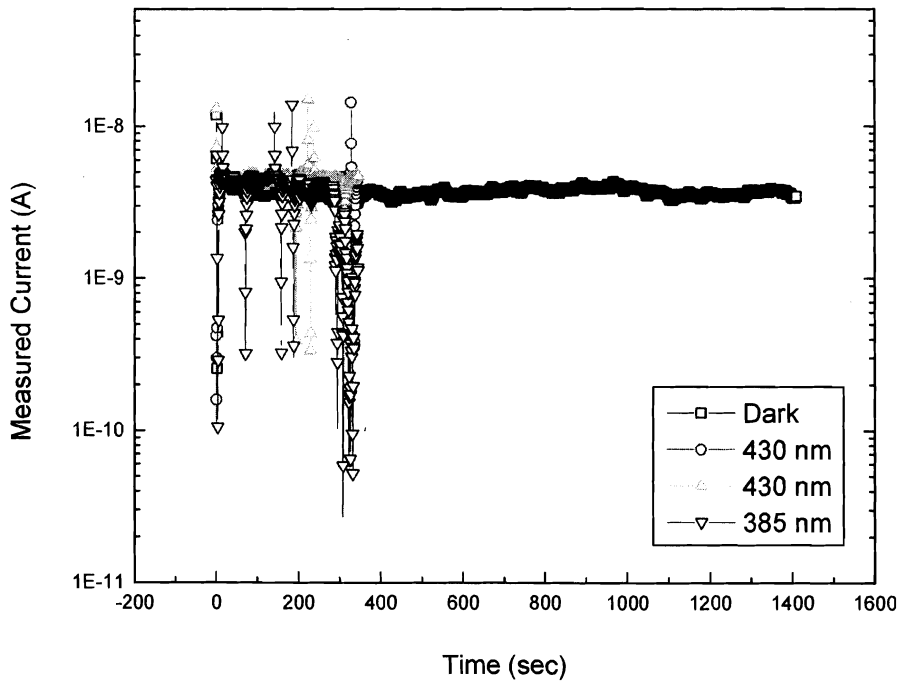

Figure 47 - Time Dependency of Luminescence – SVT 1016

If illumination causes the exchange of carriers, just as any physical mechanism, there will be time constants associated with a given mechanism, characterized by the rate-limiting step. With the imposition of time constants and multiple events, the spectrum of the current and potential, or power spectrum is of immediate interest. The Fourier transform of the time domain data will provide the frequency spectrum. Each of the frequency components is equal to a measurable periodic current, or voltage, collected from the experiment. An ensemble of frequency components in the power spectrum can be correlated to some free energy in the environment. Any physical mechanism will have a range of time constants and correspondingly a set of peaks in the power spectrum. For devices under illumination, any anomalous conduction measurements are attributed to the defect character of the film.

In the ideal case, a resistor representing a section of free standing GaN with ideal contacts will replace the Schottky contact – semiconductor system. The power leaving the unknown resistor R_{GaN} (= R) is transmitted to the multimeter's known resistance $R_{Multimeter}$ (= R'). Any power thermally generated by the multimeter is assumed to be in contact with an ideal ground and not contribute to the measurement. Following a proof from reference 167, the power leaving R is equal to the power entering R' ($P = P'$ and $I = I'$). Power is related to current and voltage by $P=I^2R$, therefore the power absorbed at R' is proportional to the mean value of the current spectrum of R times the resistance R' or

Equation 55 - Power Definition

$$P' = \left|I_O{}^2\right| R' = \left|\frac{V_O}{R+Z'}\right|^2 R'$$

Noting that $\langle y^2(t)\rangle = |y^2|$, R' <> R + Z', and ' denotes the experimental test setup value. Using the alternative Fourier expression for the voltage to express the complex variables as function of frequency, $V(\omega)=|V^2|$, the frequency representation of the power definition is derived as Equation 56 - Frequency Power Definition.

Equation 56 - Frequency Power Definition

$$V_+(\omega)R'(\omega) = V_+'(\omega)R(\omega)$$

This nomenclature change is a result of the expression

Equation 57 - Mean-Square Definitions – Cartesian and Frequency

$$\left\langle y^2 \right\rangle = \left|y^2\right| = \int_{-\infty}^{\infty} J(\omega)d\omega = \int_{0}^{\infty} 2J(\omega)d\omega = \int_{0}^{\infty} J_+(\omega)d\omega$$

Finally, using the Nyquist Theorem,[167]

Equation 58 - Nyquist Theorem

$$J_+(\omega) = \left(\frac{2}{\pi}kT\right)R'(\omega).$$

This derivation shows the frequency dependency of the noise present in a system that has a complex damping force, or resistance. In the most rigorous cases, the resistance is a function of frequency. For a real circuit, a first order approximation of this resistance function is given by the impedance expression given earlier. The generalized coordinates for this system are the resistance, capacitance, inductance, and temperature.

The complete differential expression for the charge system with noise in equilibrium is given by

Equation 59 - Ordinary Differential Equation for LCR Circuits with Thermal Noise

$$L\ddot{q} + R\dot{q} + \frac{1}{C}q = \frac{2}{\pi}kTR$$

In the proceeding expression, L is the circuit inductance, q'' is the double derivative of charge, R is the circuit resistance, q' is the derivative of the charge, C is the circuit capacitance, q is the charge, k is Boltzmann's constant, and T is temperature. Solving the above expression yields a solution for the charge in the system. From the charge differential equation, a solution expressing the current in the circuit due to illumination can be obtained.

Due to the coupling of the photoluminescence spectra with the phonon and electrical admittance spectra, observed fluctuations in power can describe a characteristic temperature of the optically induced defect electrical noise. By changing the illumination frequency, and the equilibrium point, the power produced by the photon recombination could possibly generate a specific power zone for a given dominant defect energy position, capture time, density, and type.

Monochromatic illumination can also be performed for CAFM measurements. Utilizing a monochromatic filter with UV illumination and a fiber optic cable, the standard white light illumination cable can be replaced with a fiber optic cable connected to the monochomatic filter output. CAFM scans could then be sequentially taken in white to ultraviolet light, and in the absence of light.

3.3 CAFM Measurements

To gain a better understanding of non-ideal conduction in GaN thin films, working devices were examined using the Dimension 3100 with a CAFM probe. Current topology of films at forward and reverse biases of one Volt reveals a haunting picture of numerous, ~ $10^7 - 10^8$ cm^{-2}, electrically active regions for MBE films grown directly on sapphire. Some defects appear to be aphoteric in nature, conducting at both polarities, see section 3.1.3 SVT 889 and SVT 885. Measurements have shown that defects are affective at increasing the conductivity of surrounding surface structures. Forward biases exhibit greater barrier induced lowering effects than reverse biases. Defect assisted barrier lowering could be a major source of discrepancy in device reports and a source of difficulty in obtaining good models for GaN devices.

Extended defects are distributed randomly as a function of localized deposition conditions. A number of them become electrically conductive (>10^9 cm^{-2}) at increased CAFM biases (5V sample to tip) for Pt-coated cantilevers. The current density observed in a particular defect was 10 nA peak across 77 nm feature observed at various scan rates. Device implications are significant, including not only alloying that may favor these high conductivity patches, but even in an ideal case a spectrum of interface states will create a complex contact resistance for a given device.

It is assumed that the current image in the CAFM measurements obtained on the Dimension 3100 was a base current transport mechanism between a metal-semiconductor junction (i.e. not characteristic of any environmental reactions). Current transport equations have been presented for anomalous conduction mechanisms, tunneling

components, recombination-generation centers, and thermionic emission. Sample oxidation, cantilever material diffusion, and atmospheric reductions are mechanisms that are neglected in this work, but could be represented in the data collected. There is evidence presented to suggest that a more through review of the tip sample interactions needs to be conducted, as measured current mechanism may be of an oxidation reaction. Providing an enclosure capable of evacuating to very low pressures, or displacing the atmosphere with specific gases, would enable the control necessary to systematically characterize atmospheric-tip reactions.

Another observation for reliable CAFM measurements is ensuring a low resistance path of carriers from the Dimension 3100 chuck to the sample's surface. Works prior to this study were done using silver paste from a metal backing plate to the sample surface. It was found that the bulk annealed Ohmic contact is needed to ensure: 1) a low resistance path for carriers to and from the bulk semiconductor and 2) the sample's surface is at the desired potential.

To correlate the local conduction behavior observed by C-AFM with macroscopic behavior, Schottky contact I-V characteristics were examined in parallel. The results from Schottky contacts on KOH etched GaN thin films support the CAFM measurements presented. Macroscopic devices have decreased leakage, ~ 2 – 3 orders, and better thermionic character, n much closer to 1, while CAFM measurements exhibit a lower extent of surface leakage and higher break-down voltages. Figure 48 - Current Voltage Curves for SVT 429 and SVT1026 shows the I-V curves for 75 μm-diameter Ni/Au Schottky contacts.

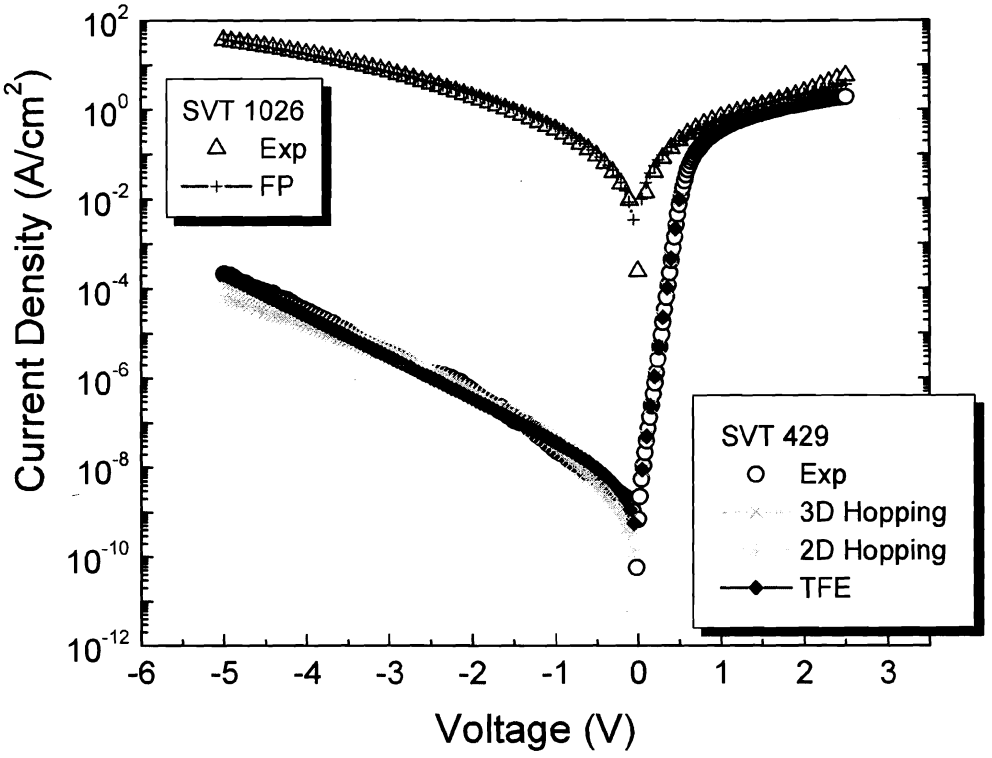

Figure 48 - Current Voltage Curves for SVT 429 and SVT1026

SVT 429 demonstrates more optimal behavior with low reverse-bias leakage and forward-bias I-V data that fits a thermionic emission mechanism (ideality factor = 1.0 to 1.2). SVT 1026 has a significantly higher leakage current and an ideality factor greater than 2. Notice that the rectifying behavior of SVT 429 produces very different C-AFM images in forward and reverse bias, as opposed to SVT 1026 with similar C-AFM data in both biases. The C-AFM images are indicators of what would be expected from the film's Schottky barrier behavior.

Extended defects are partially credited to the conduction fallacies of GaN, though a comparison of TEM results identifying extended defect concentrations did not correlate with the leakage density observed in CAFM measurements. A comparison of five samples is presented as table 4. Note the disparity between TEM dislocation densities and the observed leakage densities.

Table 4 – CAFM Leakage Density compared to TEM Extended Defect Density

SVT Sample	Total Dislocations	Screw	Edge	Mixed	Inversion Domains	Leakage Density
381	1.1×10^{9}	8.0×10^{6}	1.0×10^{9}	1.0×10^{8}	1.0×10^{7}	1.0×10^{7}
666	1.0×10^{10}		7.5×10^{9}		1.0×10^{11}	8.4×10^{7}
618	1.1×10^{9}	1.3×10^{8}	1.3×10^{8}	1.3×10^{8}	1.0×10^{11}	4.8×10^{8}
680	2.0×10^{10}		1.5×10^{10}		1.0×10^{11}	3.6×10^{7}
889		Majority				

All of the units in the table above are defect count per cm^{-2}. Additional growth structures are provided as: Figure 49 - Ga-polar SVT 666 Growth Structure and Figure 51 - N-polar SVT 680 & SVT 618 Growth Structures. The striking contrast in the leakage microstructure can be observed in figures: Figure 50 - Ga-polar Comparison of SVT 381 and SVT 666 and Figure 52 - N-polar Comparison of SVT 618 & SVT 680.

Ga polar + RF (#666)

Film Thickness: 2.2 μm; Ga-Rich

GaN-Si	RF(375, 3.09) T_s = 790 °C, P = 2.6X10^{-5} Torr, 3 hrs
GaN-Si	RF(375, 3.07) T_s = 715 °C, P = 2.1X10^{-5} Torr, 1 hr 2 min
GaN-Si	RF(400, 3.1) T_s = 714 °C, P = 3.3X10^{-5} Torr, 1 hr
GaN	RF, T_s = 503 °C, 15 min
AlN	RF(400, 3.10), T_s = 914 °C, P = 4.1X10^{-5} Torr, 30 min
Al_2O_3	

- **PL**
  - **Peak:** 3.452 eV
  - **FWHM:** 36 meV
  - **QE:** 0.031 %
  - Bad
- **Hall Data**
  - N-type
  - μ_n: 39 cm^2/Vs
  - N_D: 3X10^{17} cm^{-3}

Figure 49 - Ga-polar SVT 666 Growth Structure

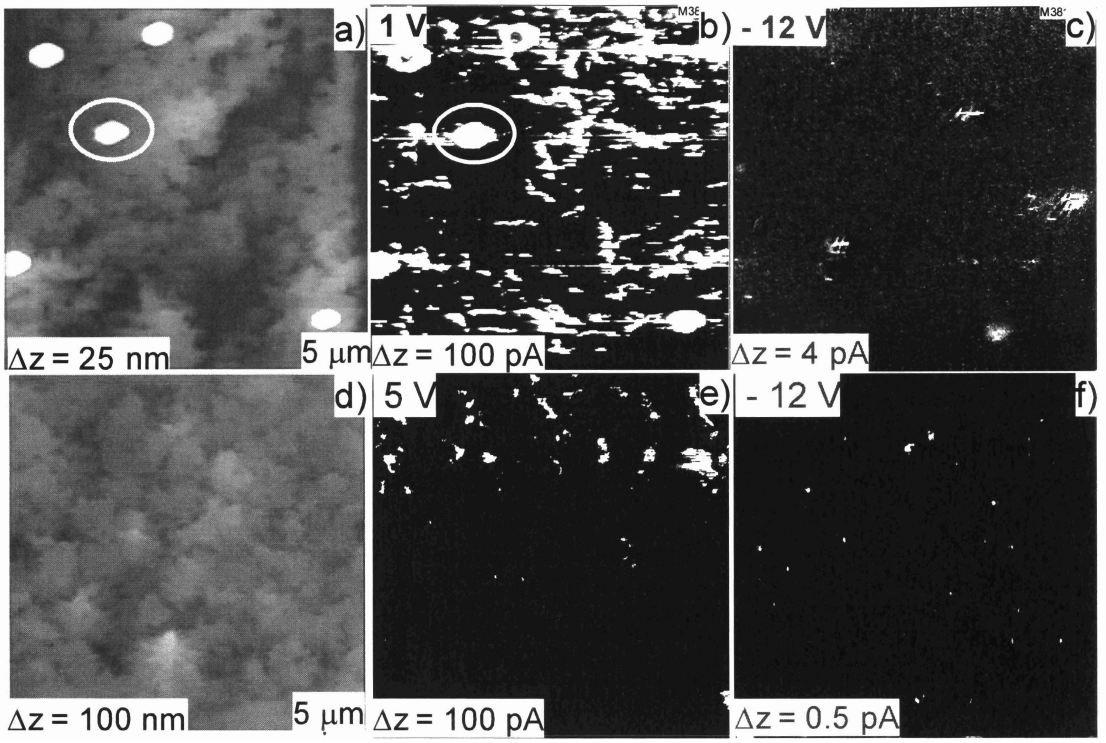

Figure 50 - Ga-polar Comparison of SVT 381 and SVT 666

a) SVT 381: As Grown - Total: 1.1×10^{9} cm^{-2} (Screw: 8.0×10^{6} cm^{-2}; Edge: 1.0×10^{9} cm^{-2}; Mixed: 1.0×10^{8} cm^{-2}); ID's: 1.0×10^{7} cm^{-2}
b) SVT 381: 1V Forward Bias, 45 % Sat; Turning ON, LFD: Indeterminate
c) SVT 381: -12 V Reverse Bias, 1 % Sat; Turning ON, LFD: 5×10^{7} cm^{-2}
d) SVT 666: As Grown - Total: 1.0×10^{10} cm^{-2} (Edge: 7.5×10^{9} cm^{-2}); ID's: 1×10^{11} cm^{-2}
e) SVT 666: 5 V Forward Bias, 15 % Sat; Saturating, LFD: 1×10^{8} cm^{-2}
f) SVT 666: -12 V Reverse Bias, 5 % Sat; Saturating, LFD: 5×10^{7} cm^{-2}

N polar + RF: #680

Film Thickness: 2.6 μm; Ga-Rich

Surface Fix GaN T_s = 779 °C
GaN-Si RF(375, 3.09), T_s = 779 °C, P = 2.9X10^{-5} Torr, 5 h
Anneal T_s = 863 °C, 10 min
GaN RF(400, 3.09), T_s = 580 °C, 6 min
Al_2O_3

- **PL very bad**
  Peak: 3.429 eV
  FWHM: 69 meV
  QE: 0.045 %
- **Hall Data** n-type
  μ_n: 31 cm^2/Vs
  N_D: 1.7×10^{17} cm^{-3}

N polar + RF: #618

Film Thickness: 2.3 μm; Ga-Rich

GaN-Si RF(375, 3.09), T_s = 790 °C, 2.4×10^{-5} Torr, 3 h
GaN RF(450, 3.05), T_s = 725 °C, 1.8×10^{-5} Torr, 1.5 h
GaN RF(450, 3.025), T_s = 505 °C, 1×10^{-5} Torr, 1 h
Al_2O_3

- **PL good spectrum**, no DAP
  Peak: 3.470 eV; **FWHM:** 11 meV
  QE: 0.14 %
- **Hall Data** N-type
  μ_n: 195 cm^2/Vs N_D: 5X10^{17} cm^{-3}

Figure 51 - N-polar SVT 680 & SVT 618 Growth Structures

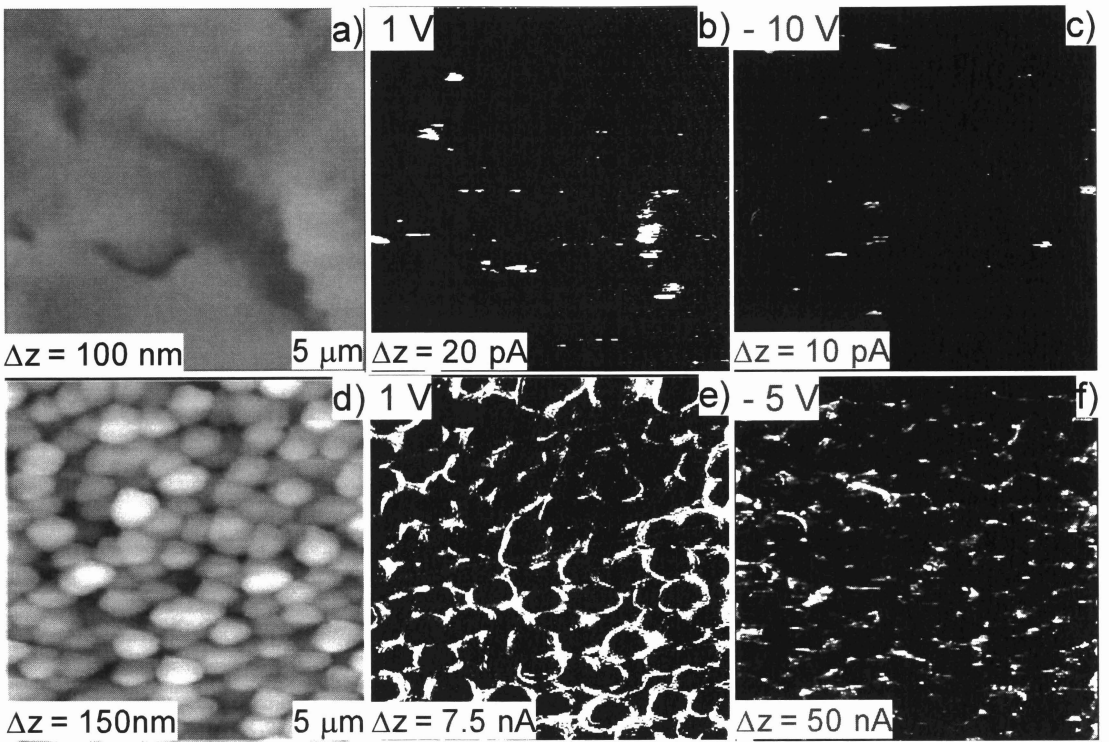

Figure 52 - N-polar Comparison of SVT 618 & SVT 680

a) SVT 680: As Grown - Total: 2×10^{10} cm^{-2} (Edge: 1.5×10^{10} cm^{-2}); ID's: 1×10^{11} cm^{-2}
b) SVT 680: 1V Forward Bias, 5 % Sat; Turning ON, LFD: 6.0×10^{7} cm^{-2}
c) SVT 680: -10 V Reverse Bias, 1 % Sat; Turning ON, LFD: 3.6×10^{7} cm^{-2}
d) SVT 618: As Grown - Total: 1.1×10^{9} cm^{-2} (Screw: 1.3×10^{8} cm^{-2}; Edge: 1.3×10^{8} cm^{-2}; Mixed: 1.3×10^{8} cm^{-2}); ID's: 1×10^{11} cm^{-2}
e) SVT 618: 1 V Forward Bias, 65 % Sat; Saturating, LFD: Indeterminate
f) SVT 618: -5 V Reverse Bias, 25 % Sat; Saturating, LFD: 4.8×10^{8} cm^{-2}

A final observation of etched films lends more insight into the complex nature of GaN thin film conduction. Figure 53 - SVT 1016 CAFM Induced Leakage shows a series of scans exhibiting memory effects in the conduction. In panel (a), the conductivity of the film is nonexistent in the first scan. The second panel, (b), displays evident conduction at the edges of the scan. In the final panel, (c), a 10 μm^2 scan, it can be seen

that conduction is present outside of the area of the previous scans, though it was absent in initial scans.

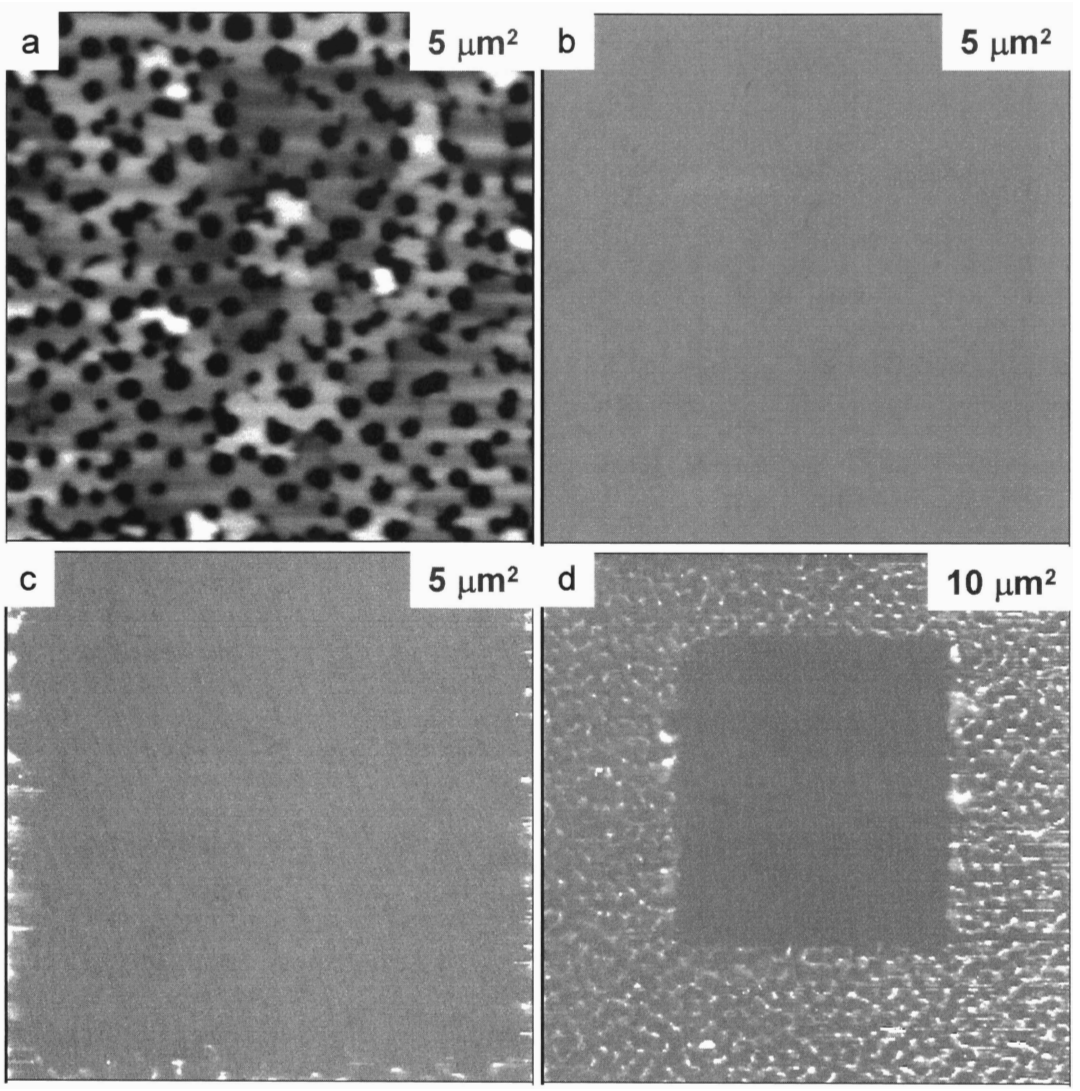

Figure 53 - SVT 1016 CAFM Induced Leakage

Contrasting with the above example, some films show conductivity in initial scans that degrades with successive scanning, as in Figure 54 - SVT 1460 Memory and Degrading Conduction.

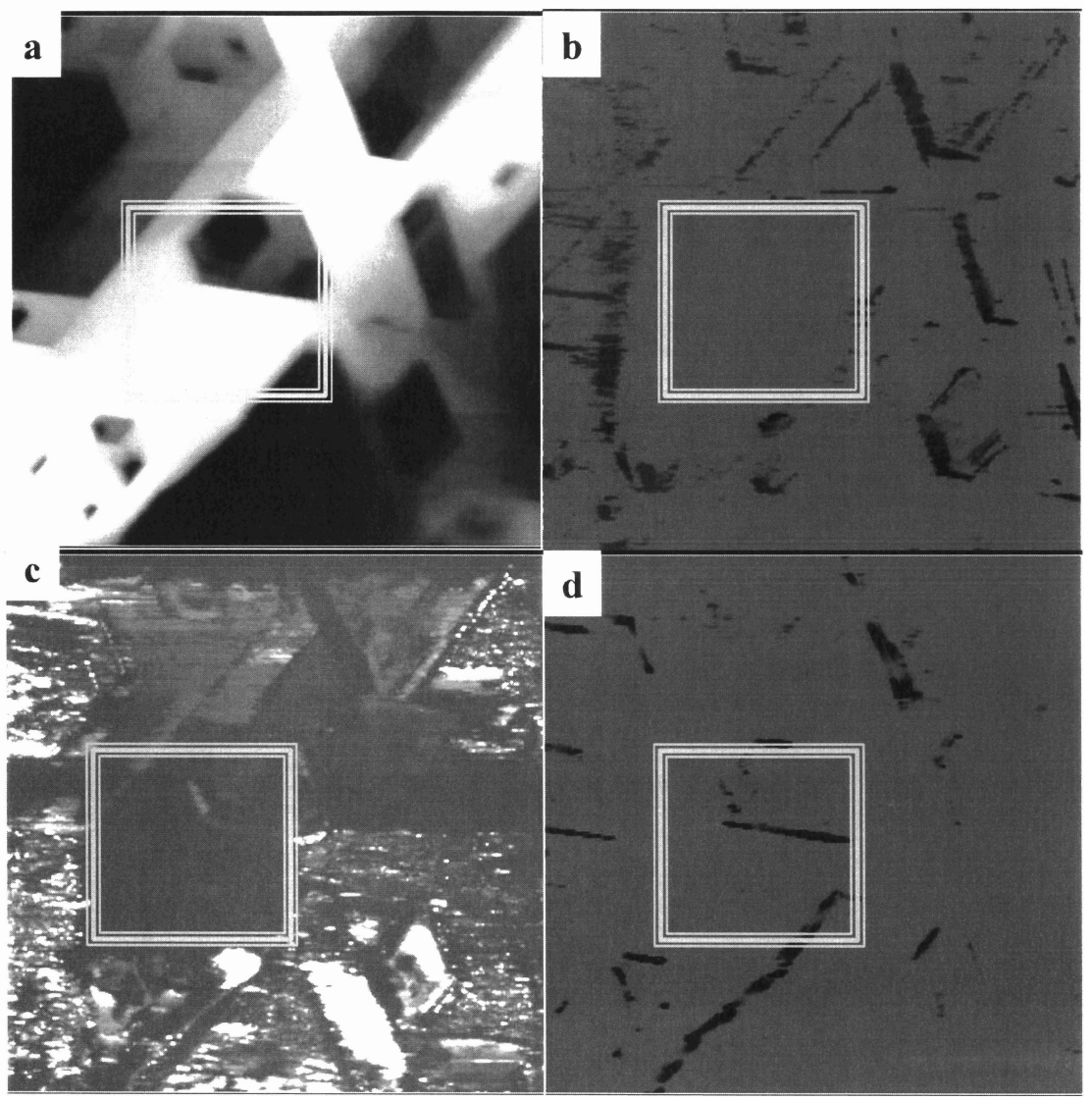

Figure 54 - SVT 1460 Memory and Degrading Conduction

a) topography, b) 0.5 V 4th scan, c) -0.5 V 5th scan, d) 0.5 V 6th scan. Vertical Scale is 100 nm on all images and image scale is 5 μm^2 for images a-d. The CAFM current range is 1 nA for b - d.

A 2 μm^2 area was scanned twice at 0.5 V forward bias and once in reverse bias, denoted by the boxed region in the figure, before the 5 μm^2 CAFM image in panel b was taken at a 0.5 V tip – sample bias. The films' conductivity can be slightly restored with negative polarity, seen in comparing panels c and d. It is believed that part of the observed current is an oxidation reaction, which decreased the overall conductivity of the films surface but enhanced the surrounding defect related conduction areas. The increased conduction areas degraded with many more scans. Another factor at play are point defects' charging and discharging behavior. The charge exchange between bulk and / or surface defects may create instabilities and quasi-memory in the film. Previous scans fill defect states, which may have long relaxation times in complex configurations, and successive scans do not show conduction over charged defect states. By reversing the polarity, panel c, the defect states are possibly discharged. The final scan shows conduction over a larger range of features, suggesting the conduction of more defect states has been enhanced by the non-equilibrium nature of initial scans. Sample-tip interactions were noted to increase in magnitude after CAFM scanning, rendering tapping mode images unattainable in some devices due to massive artifacts. The proceeding data supports claims of environmental aging and surface related effects in devices,[168] and identifies possible memory effects in the GaN system.

3.3.1 Localized CAFM Spectra

The Dimension 3100 AFM is designed to run in two modes of operation, spectra or topography. When investigating the surface topography the tip deflection is monitored through a feedback loop and converted into a representation of the sample's surface. A trace and retrace are taken for each line of topology data. For instance, on a trace the topology can be measured and a second parameter can be measured on the retrace. The spectra mode holds the tip in a single location and ramps a parameter of interest, while measuring another variable. Localized CAFM spectra are obtained in a similar manner to Force spectra, though instead of increasing the force applied to the tip, the bias on the metallized cantilever is swept and the position and force is held constant while measuring the current flow through the tip – semiconductor junction. It must be noted that the drift in the piezoelectric stacks, responsible for maintaining the tip's position, cannot be neglected in taking spectra. It was found that drift is typically on the order of 10's – 100's of nanometers per minute in both spectra and topology measurements. Care must also be taken in selection of the number of integrations, step size, and hold times when taking CAFM spectra, keeping in mind that the tip drift will distort results. In the case of integrations' characteristics affects on electrical measurements in the Dimension 3100, the defect structure observed in SiC, GaN, and ZnO demonstrated significant localized charging effects. It was found that if averaging were done over several spectra, combined drift and charging / memory effects would render collected data meaningless. The defects are also observed to play a significant role in hysterisis in spectra. Reversing the applied bias endpoints and step polarity can produce different current spectra

characteristics. Additional transport mechanisms may need to be considered to account for the anomalous charging behavior demonstrated with prolong sample scanning.

Using C-AFM, localized I-V spectra were taken from regions located both on and off the hillocks of sample SVT 889, as seen in Fig. 3.3.1.1. Curve 1 on a hillock shows detectable leakage at a reverse bias of ~ 9 V, whereas region 2 off a hillock shows no measurable leakage. The forward turn-on voltage is also seen to shift down to ~3 V on a hillock. Note that the relatively high turn-on voltages observed for C-AFM indicates a possible significant voltage drop in the tip-semiconductor junction. The observed shifts in forward and reverse bias for current conduction on the hillock indicate the possibility of charge trapping effects. Subsequent I-V spectra at the same location show a significant decrease in current after three to five scans. Curve fitting of current conduction mechanisms indicates that current conduction is consistent with a Frenkel-Poole (FP) conduction mechanism in the defective hillock region, and field emission (FE) away from the defect-containing hillock. I-V data obtained from macroscopic Schottky contacts indicates that thermionic field emission is the primary mechanism at higher applied biases.

BEFORE Spectra

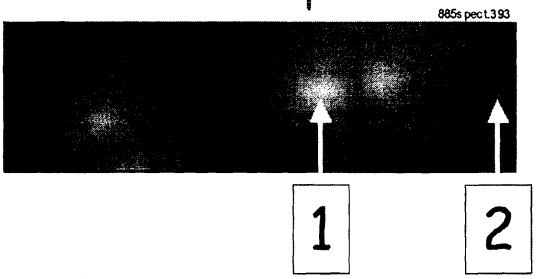

AFTER Spectra Forward Bias (5 V)

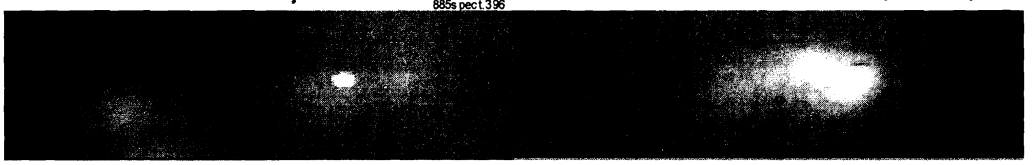

Reverse Bias (12 V)

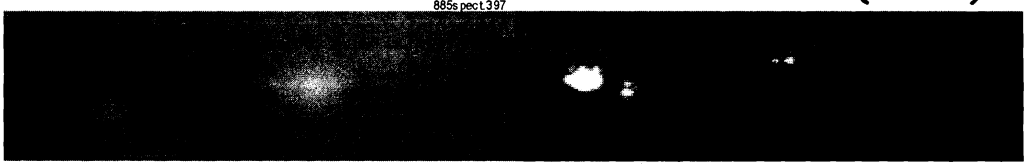

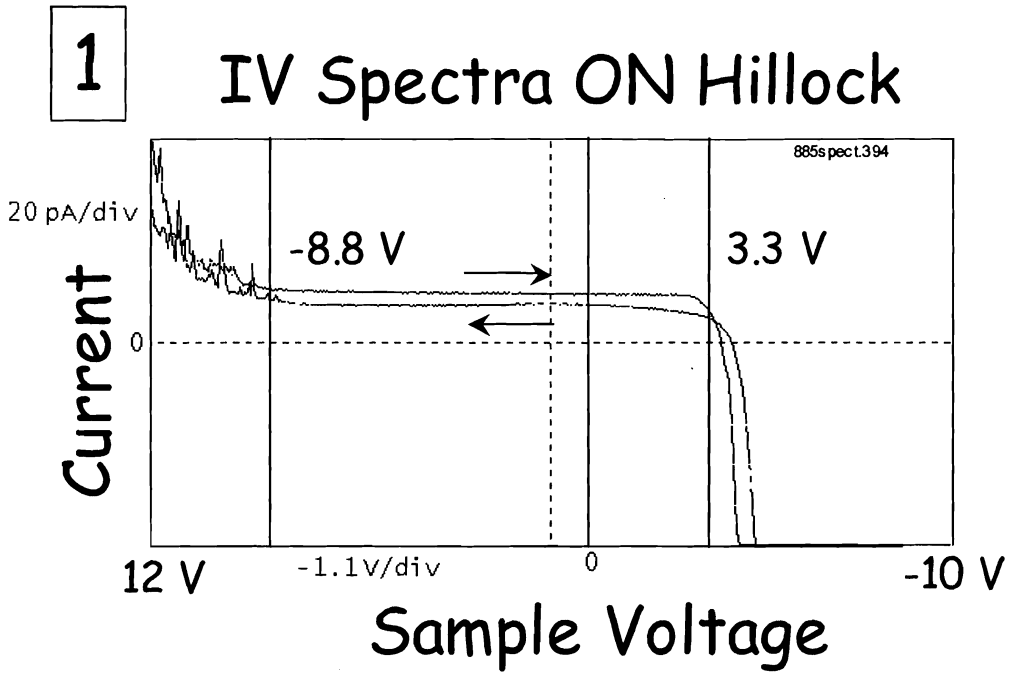
1
IV Spectra ON Hillock
885spect.394
20 pA/div
Current
0
-8.8 V
3.3 V
12 V
-1.1V/div
0
-10 V
Sample Voltage

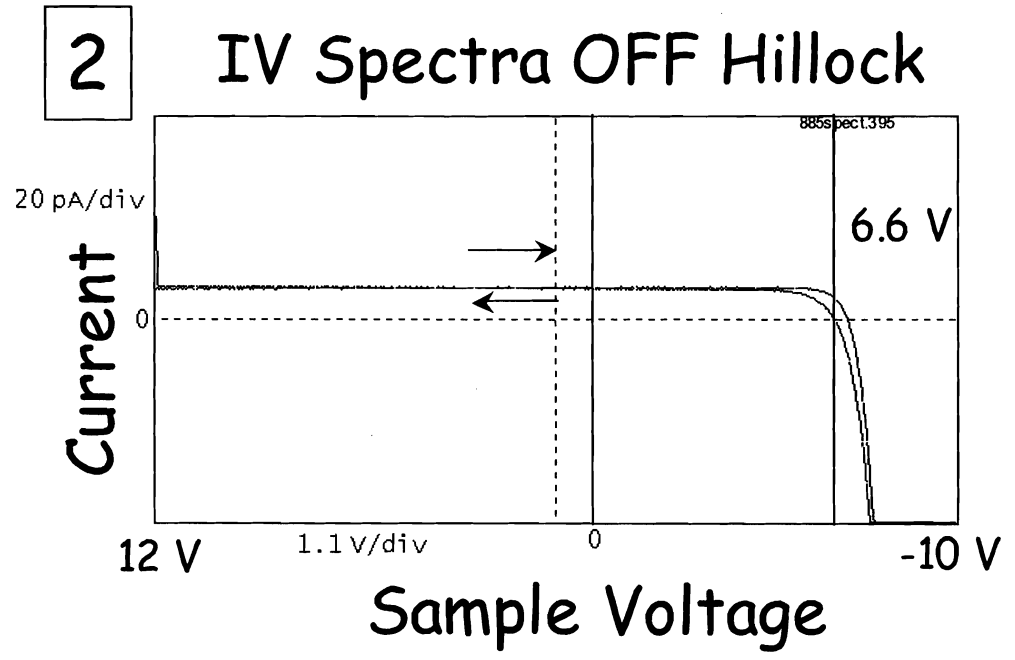
2
IV Spectra OFF Hillock
885spect.395
20 pA/div
Current
0
6.6 V
12 V
1.1V/div
0
-10 V
Sample Voltage

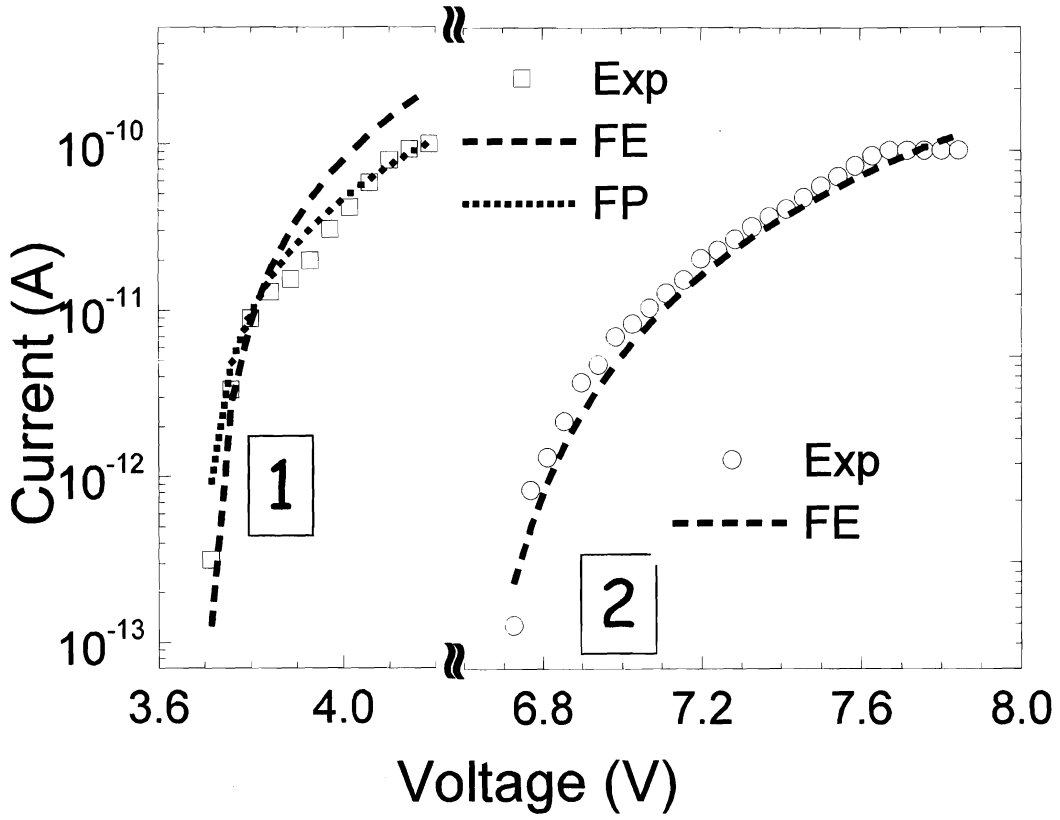

Figure 55 - SVT 885 CAFM Spectra

The conduction exhibited at the hillocks in this MODFET structure, SVT 885, could be from a number of sources. Polarization issues associated with the extended defects and the heterostructure could enhance alloy disorder in the capping layer or point defect distributions, such as vacancies. The non-uniform distribution of point defects could be seen as a form of screening the strain of the extended defect in the hillock center during the deposition. The point defects could just as well be generated from the screw

dislocation and / or an accelerated growth front. The exact mechanism that couples the two defect types is unidentified. Even though it is a nonideal technique for resolving the issue, EDX was performed on the sample but no detectable variance in Al, or any other anomaly, was found in the contacts or semiconductor. The exact nature of the relationship between extended defects and point defects becomes extremely interesting, as it may lend insight into point defect reduction.

Contrasting the conduction of sample SVT 885, spectra data for the Samsung Ga and N faces is presented as Figure 56 - Samsung Ga and N-polar CAFM spectra.

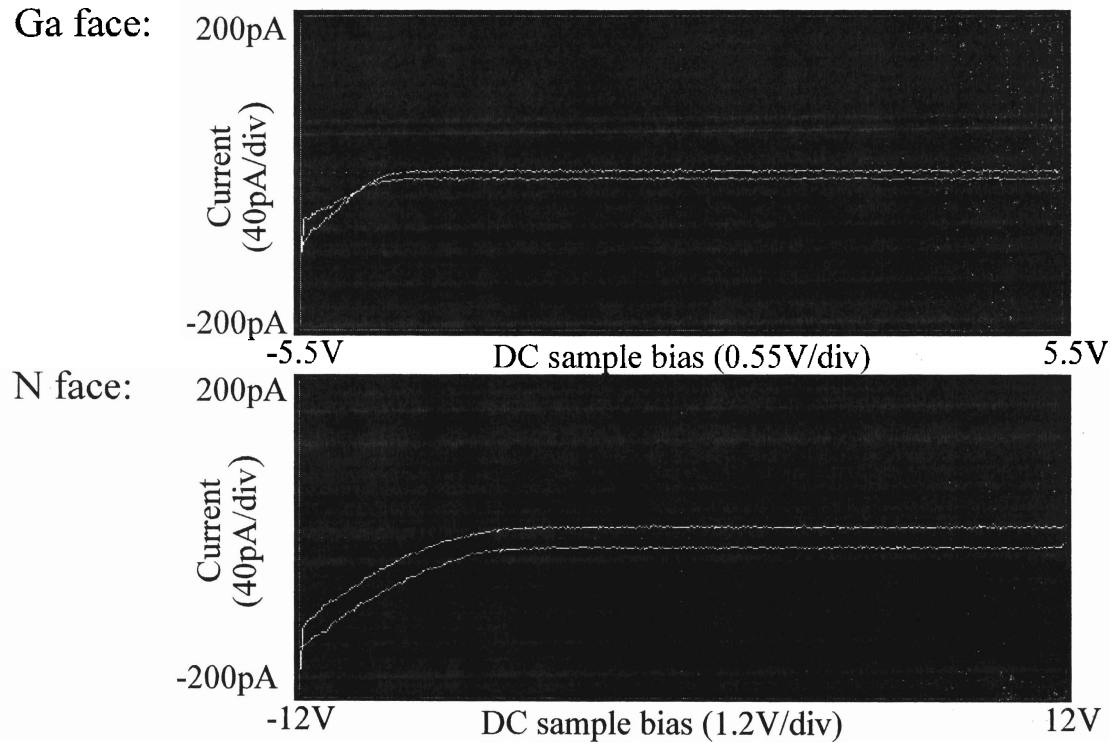

Figure 56 - Samsung Ga and N-polar CAFM spectra

The Ga-face exhibited a turn on response at –5.0V for the CAFM sample-tip bias convention, equivalent to 5.0V forward bias for Schottky contact, with no noticeable breakdown in the reverse bias, contact convention. The nitrogen face began to exhibit conduction at 6.0V without significant breakdown in the reverse bias region. The hysterisis is larger in the N-face sample, and indicates increased activity of point defects.

To further illustrate the technique of CAFM spectra, SVT 1016 was analyzed in the same manner as SVT 885. The Schottky diodes for SVT 1016 had good thermionic responses, n ~ 1, with little leakage current, $J_{R@-5V} \sim 10^{-9}$ A. Typical IV curves for an As-deposited device are displayed in the following figure.

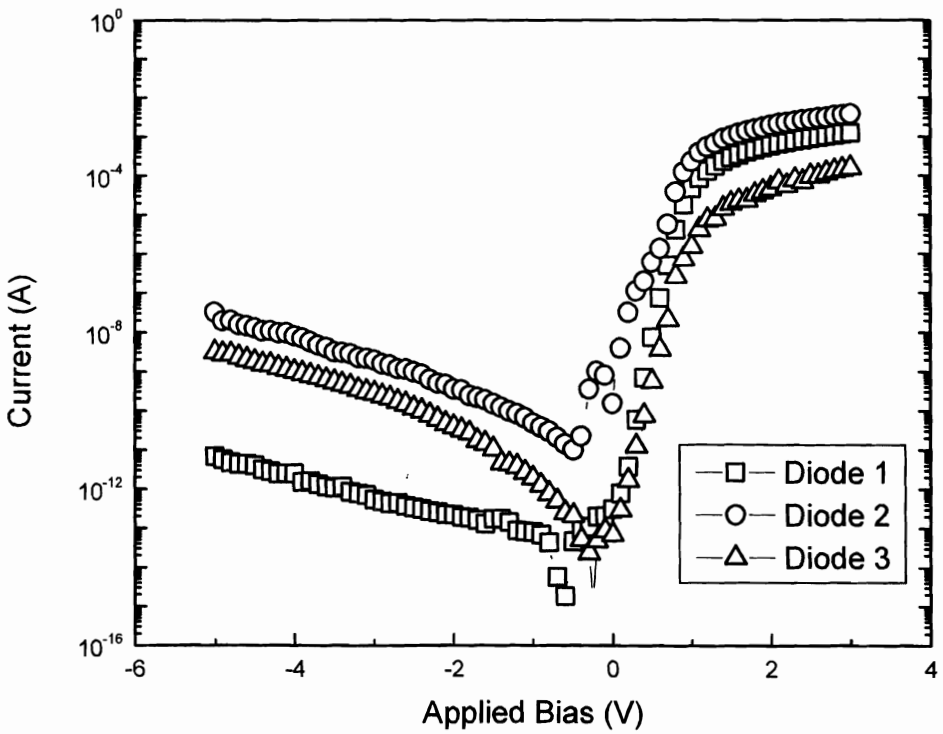

Figure 57 - SVT 1016 75 µm As-Deposited Schottky Current-Voltage Curves

The CAFM spectra results with curve fitting are presented as Figure 58 - SVT 1016 CAFM Spectra Results. The spectra points are separated by 250 nm on the centerline of the images.

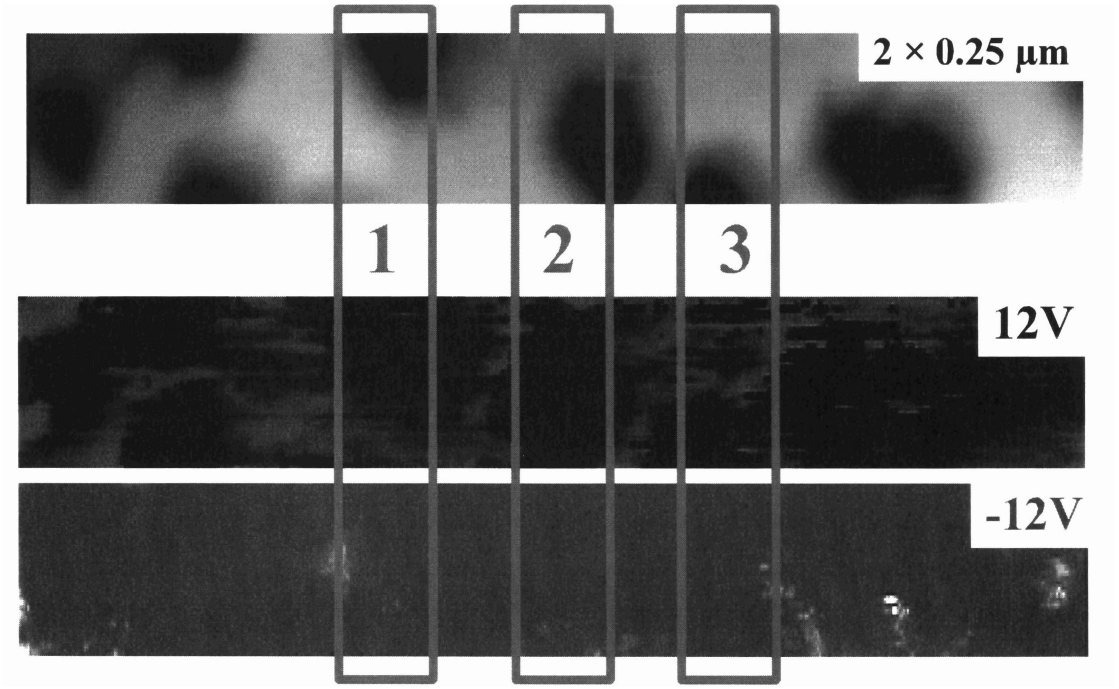

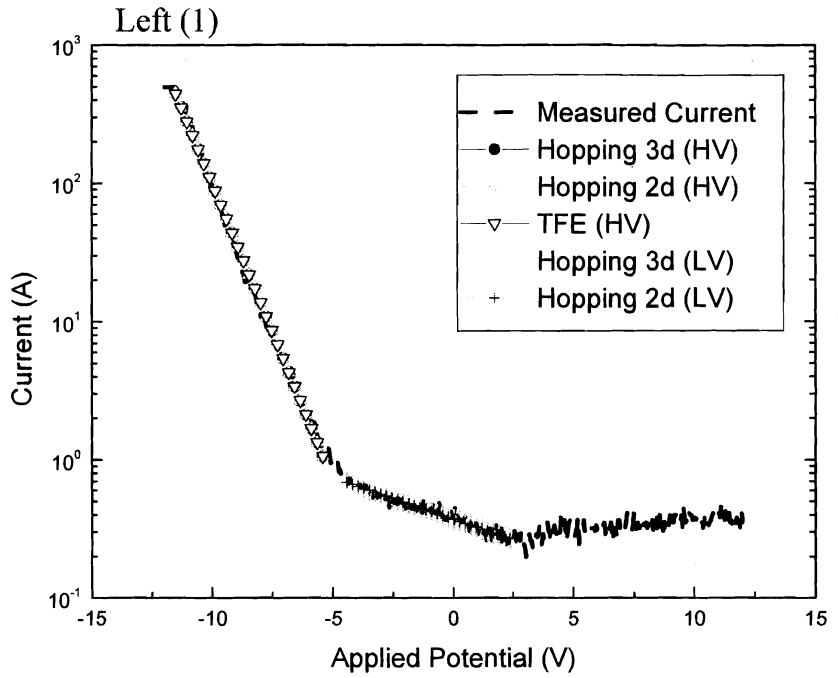
Left (1)
Measured Current
Hopping 3d (HV)
Hopping 2d (HV)
TFE (HV)
Hopping 3d (LV)
Hopping 2d (LV)
Current (A)
Applied Potential (V)

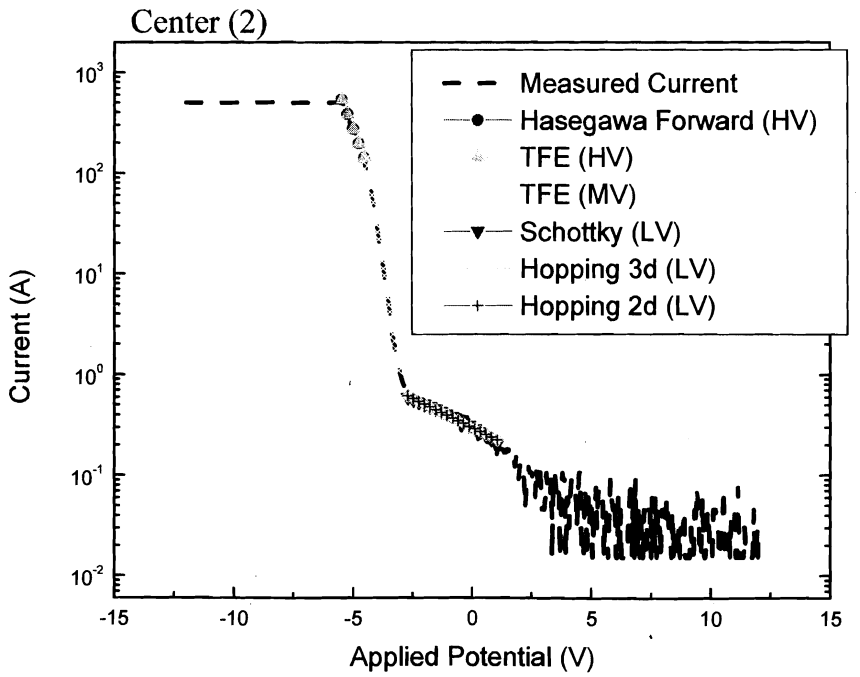
Center (2)
Measured Current
Hasegawa Forward (HV)
TFE (HV)
TFE (MV)
Schottky (LV)
Hopping 3d (LV)
Hopping 2d (LV)
Current (A)
Applied Potential (V)

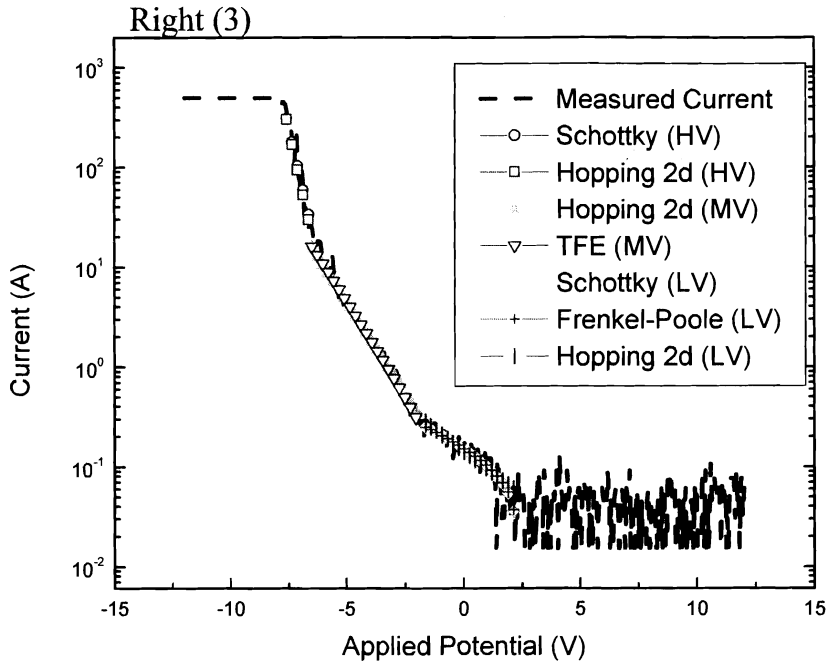

Figure 58 - SVT 1016 CAFM Spectra Results

The curve fitting is inconclusive as to the exact nature of the conduction, though the likely suspect is TFE conduction for higher forward biases and field emission for lower biases. There is compelling data that suggest the Hopping conductivity is playing a role, both in macroscopic contacts (Diode 2 / Figure 57 - SVT 1016 75 μm As-Deposited Schottky Current-Voltage Curves) and on a microscopic level. There are also signs of Schottky, Frenkel-Poole, or FE conduction (Diode 3 / Figure 57 - SVT 1016 75 μm As-Deposited Schottky Current-Voltage Curves). The danger of fitting conduction curves without temperature variance is evidenced in the proceeding set of figures. Without

establishing the conduction mechanisms' behavior as a function of temperature the labeling of a defect mechanism is somewhat speculative (IVT's were conducted on SVT 1016 but are not presented in this work). One could envision an AFM setup with evacuation and temperature control down to near cryogenic temperatures.

Significant limitations exist with the Dimension 3100 software and CAFM setup. The current range is linear, while convention is logarithmic. The Scanning Side Resistance Module (SSRM) was used to investigate some of the samples because it has a logarithmic current response, though the topography was less informative. The bias ranges for the CAFM and TUNA modules are unsuitable for samples with large intrinsic resisitivities. The method of implementing spectra-topology correlations, and exporting data, is unnecessarily tedious. Modifications including atmospheric and temperature control have been previously mentioned.

3.3.2 Simultaneous EFM and CAFM

It was of interest to see if there was a coupling of the surface potential and regions of increased conductivity. The CAFM tip holder had to be adapted to conduct simultaneous measurements. EFM measurements apply a potential to the tip from the pins in the part of the Dimension 3100 that holds the tip holder in the machine, while the CAFM tip holder is grounded and is referenced from an applied chuck voltage. Referring to Figure 59 - Adapted CAFM Holder, the CAFM tip holder must have the signal lead connected from the tip connection to the pin labeled AFM tip. This will allow the voltage applied to the AFM tip pin to be applied to the cantilever, thus enabling EFM measurements in a CAFM tip holder.

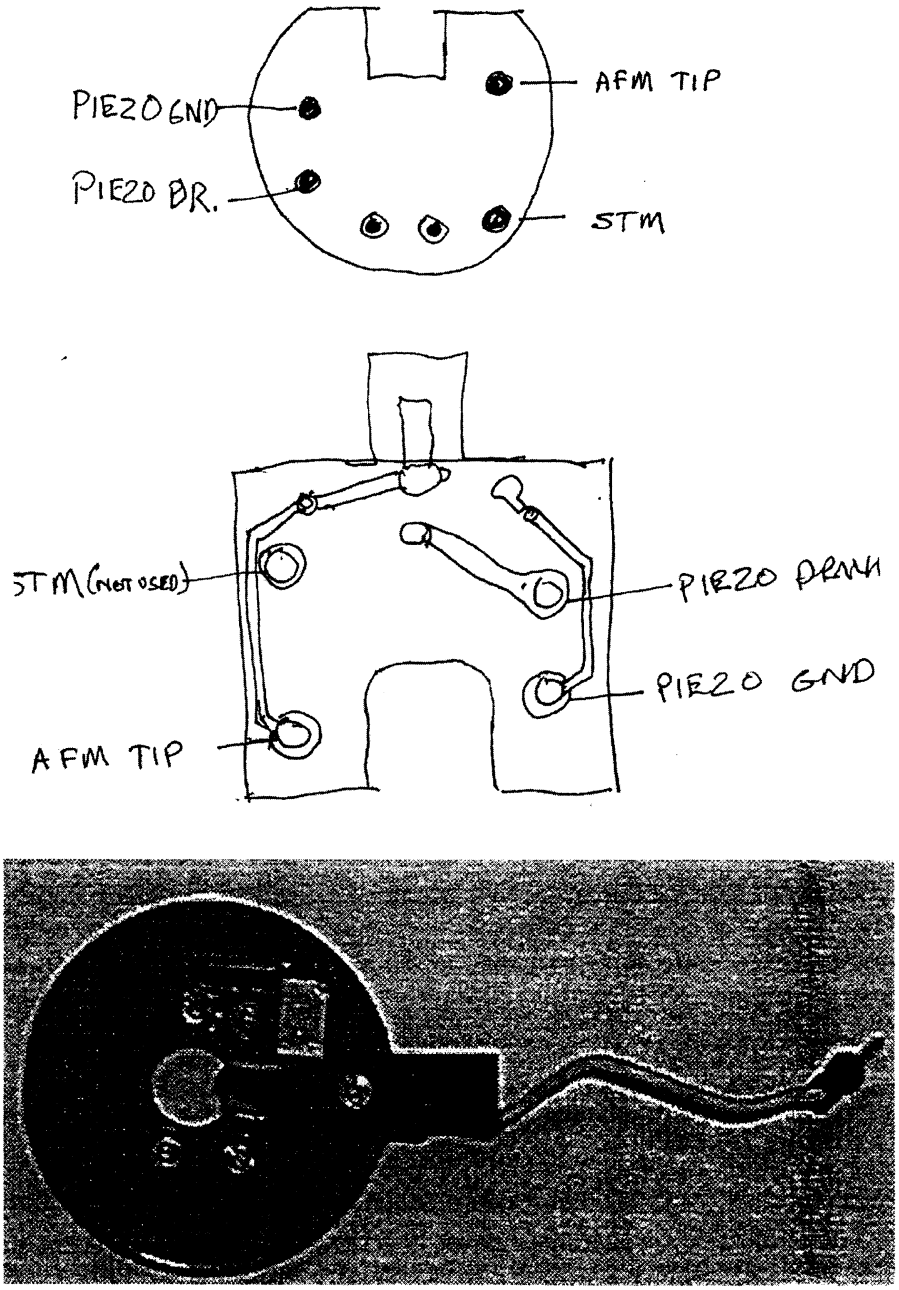

Figure 59 - Adapted CAFM Holder

It was found that the CAFM tip holders are quite fragile and may fall apart even if they are not modified, additionally connections on the tip holders have a high quality finish that complicates bonding. Arc welding, or removing / roughing the finish, may help with the bonding issues at the pin connector. The connection to the tip has a higher propensity for problems; the metallization on the tip holder can be removed causing a critical failure of the part. Wrapping the end of the tip holder and connected wire with a very thin gauge wire (or other suitable brace) removes the stress point from the electrical contact and will significantly prolong the part life.

EFM and CAFM measurements were conducted on an MBE GaN overgrowth, SVT 889, an overgrowth on an HVPE template prepared by Lincoln labs. In Figure 60 - SVT 889 EFM and CAFM, aphoteric defects can be seen in comparing the conduction in circled regions at reverse and forward bias. Some conduction paths are present in only one polarity, while the amphoteric defects are seen conducting at both positive and negative polarities. The reverse bias conduction is uniform and the non-uniform forward bias conduction has no correlation, in magnitude or distribution, with the surface potential image presented.

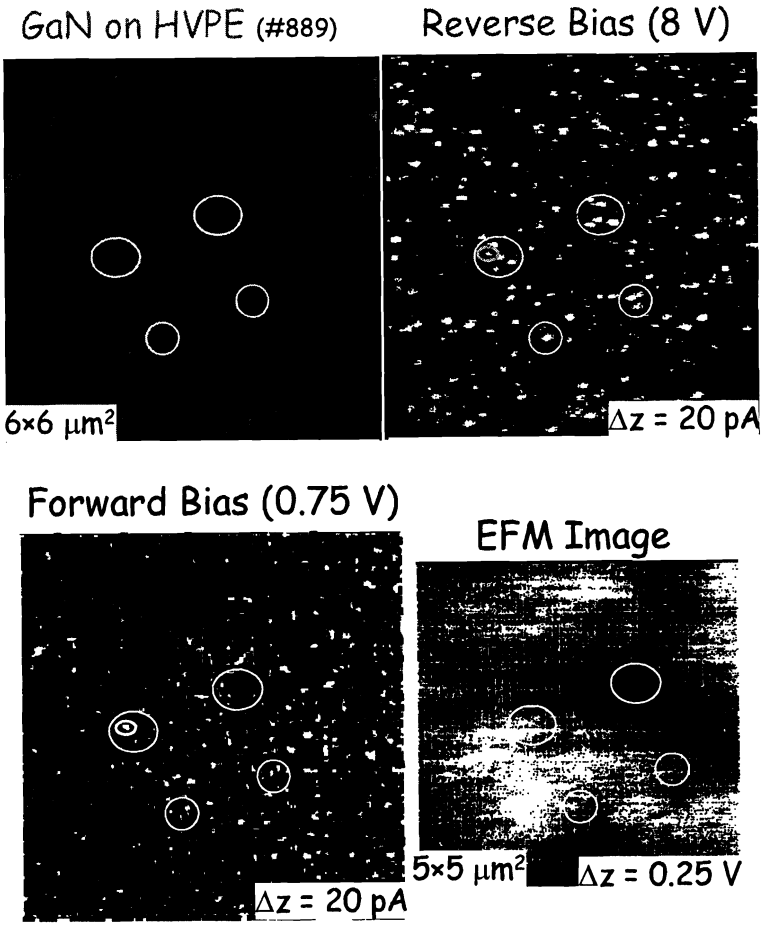

Figure 60 - SVT 889 EFM and CAFM

3.3.3 Proposed Extensions to CAFM Technique

Further extensions rely on the fiber optic input of illumination and the extended signals box (used to directly control the bias applied to the CAFM tip). For topography images extending the bias limitations would allow imaging of highly resistive samples, or samples with extremely small leakage components. Pulsed measurements could allow a form of micro DLTS to identify specific point defects at topographical features. Adopting a method from TEM samples could be prepared for cross-sectional CAFM,

allowing a heterostructure's, or multiple quantum wells', polarization charge and corresponding modulation with gate bias to be thoroughly studied. Defects' roles in channel charge modulation are an imperative topic of interest. As mentioned in section 3.2.3 IV Measurements on Schottky Contacts under Monochromatic Illumination, illumination studies could be applied to the Dimension 3100 and CAFM imaging by utilizing the fiber optic illumination port and a tunable monochromatic illumination source. A final improvement to the AFM tool would require control of the ambient atmosphere. By conducting CAFM in vacuum or inert ambient, atmospheric reactions with water and gases can be safely neglected or thoroughly explored. The extensions presented will greatly extended the capabilities of the tool, increasing the ability of engineers and scientist to resolve complex issues involved in defect conduction.

3.4 Silvaco Simulations

The Silvaco software is composed of specialized modules. By adding modules the abilities of the simulator can be extended, for example a 3-d package is available. Atlas is the module that allows device physics simulations. Athena is another module that allows for device fabrication process simulation, such dopant implantation. Atlas with Blaze will provide the necessary functionality to model wide bandgap hetero junction devices. The Blaze extension will enable quantum statistics necessary for calculation of energy states and population in the 2-DEG. The Fast Blaze extension will enable the simulation of device frequency responses.

3.4.1 Atlas Overview and Statements

An Atlas program is composed of five basic parts: Structure specification, Material models selection, Numerical method selection, Solution specification, and Results analysis. [169, 170] The UNIX based software can be accessed after logging onto a SUN workstation in the VLSI lab by entering the following command at the *Console* prompt: /apps/silvaco/bin/deckbuild –as. The first portion of the command identifies the executable file (deckbuild) and the switch, -as, enables the Atlas package. Figure 61 - Silvaco Atlas Program / Command Structure gives a hierarchical picture of a typical program layout with some representative commands. Each type of material has a specific set of parameters relevant to the carrier dynamics and energetics in that material, many materials are included as part of the Silvaco package in the materials database. If the material is not included, it can be added in the form of a data file. The Blaze extension provides functionality to Silvaco for modeling the family of III-V's, SiC, SiN_X, and a host of other materials. Parameters that are included in the materials database and the simulator will be used, unless the user overrides these values by defining material parameters for semiconductors, metals, or insulators with the *materials* statement. Care should be taken as simulations can produce results with undefined material parameters! Silvaco provides a statement, *models print*, which allows the developer to view a printed list in the execution window of all the material parameters currently initialized and their corresponding values. The material parameters used in this simulation were the defaults for the binary compounds and a linear interpolation between the default values for InGaN.

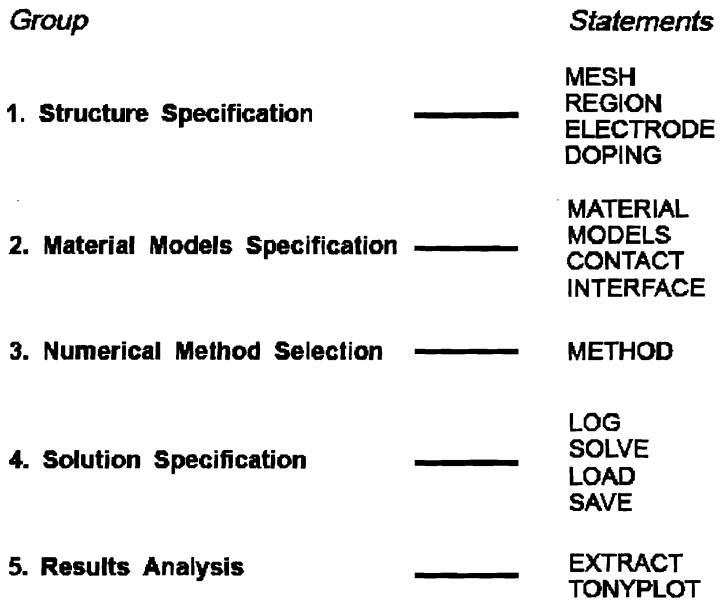

Figure 61 - Silvaco Atlas Program / Command Structure

Atlas command groups with basic functions. (From ref. 169 without permission)

Starting with the structure specification and progressing through the flow of the proceeding figure, the detailed aspects of the simulator and modeling choices will be discussed.

In order for mathematical models of physics to be addressed on a desktop machine, it is necessary for a finite array of elements to represent the system, or solution space. Atlas programs begin with a mesh specification. A mesh defines the elements of the array representing the device. For a first attempt, a regular rectangular mesh is constructed by defining a column and row length and step size. In areas of the device structure that have rapidly changing parameters, the mesh size should be small enough to produce continuous functions of the parameters. Once the mesh is constructed, physical

boundaries must be established for the materials and contacts of the device. Next in the Materials models selection, functions are used to define the internal energy structure of the materials, including point defects and band alignment.

Once the mesh, device regions, contacts, materials, and appropriate physical models are in place, the numerical methods by which the non-linear differential equations will be resolved are defined in the Numerical Methods selection. The convergence criteria are defined for declared solution methods. For example in a Gunn type device, models must account for NDR. In a FET type device, characteristic NDR velocity-field relationships would probably cause instabilities and correspondingly erroneous results. Subsequent to the Numerical methods section, the problem or physical situation in question is simulated with commands in the iterative solution specification of the device. Finally, the Results analysis is performed with commands invoking Tony Plot.

3.4.1.1 Mesh

The mesh is one of the most critical aspects to the simulator environment. The mesh dictates the accuracy and speed of the simulation. Excessively large meshes can slow the solution convergence time to a crawl by expanding the problem's solution space geometrically in computational time. The simulation will halt when the mesh size exceeds a critical value. The most important aspect to the mesh lies in the density of the mesh with respect to the rate of change in the variables of interest. For MODFET's the critical regions are defined in the x-y plane as the area between the gate and the drain and in z-direction the region containing the heterointerface and under the Schottky contact.

Optimizing the mesh will provide reliable results in the minimum time. The eliminate statement is useful in reducing the mesh density in irrelevant places. Extreme caution should be used as holes can develop in the mesh when eliminate statements are improperly used. In order to improve the accuracy of the simulations, a regridding function is included in the Atlas package. A specific variable, or variables, are identified with tolerances. In the event a tolerance is not met during calculation of the sample space, the program will update the mesh in an effort to smooth out the variables' profiles. Attempts at regridding were unsuccessful, causing simulation crashes and unpredictable results. Further assistance from Silvaco or others would be necessary to benefit from this feature but there was not a service contract in place with Silvaco. In summary of the mesh, it must be certain that mesh is continuous in nature and does not change too rapidly, or too slowly, to ensure reliable simulation results.

3.4.1.2 Solution Forms - Extract & Probe Statements

Standard solutions can be obtained with the Silvaco software's *solution* command. As previously mentioned, this command solves the necessary physical equations by resolving the boundary conditions under the given physical constraints for the given device biasing. To calculate the current flowing into or out of a terminal a number of other physical variables come into play. Although these variables, such as carrier velocity, are not displayed in a standard solution display any variable can be added to the .log file with the probe, extract, or output statements in Atlas. The probe command allows for given variables to be measured at a given spatial point in the mesh and added to the .log file. The extract statement is a more powerful version of the probe

statement. The output statement is a broad addition function; appending the earmarked variables in all .log files created. The data can be accessed and cosmetically modified in Tony Plot. Another option is to write a settings file, .set file, for Tony Plot. The data logging functions can greatly enhance the introspective nature of the simulator.

In a DC simulation of device characteristics, the contact potentials are set for a device operation point. The contact potentials are the last set of boundary conditions necessary for the solution of the device characteristics. Each solution could be thought of as a single data point that would be measured in an experimental setup. At each gate-drain biasing point the entire 2 dimensional mesh of the device is begin computed in entirety. As the contact potentials change the carriers' local properties in the device change, therefore it is necessary to solve for each drain bias at a given gate bias in the MODFET problem presented. For lower voltages, single solutions are obtained for the linear response region of the drain current versus voltage curve, while at higher biases in the saturation region a sweep method is utilized. After completing a single drain current voltage curve, the gate bias is set to the next value and the drain sweep process repeated until all of the necessary curves are obtained. Data logging is essential to the MODFET simulation, it is how the data is saved into an external file and is required after each gate curve solution is obtained.

The simulation culminates in a solution. Atlas obtains solutions by solving the specified physical equations using the nonlinear iterative methods chosen by the user. The most robust choice for the nonlinear methods is the *Gummel Block Newton* option in the method statement, as it provides for multiple solution methods tailored to certain

situations. The ways in which Gummel, Block, and Newton solutions are used in large numerical problems can be explored more in the Atlas manuals. Each solution method has advantages in certain situations, by combining them in various manners the best range of solutions can be obtained. The price for exploring many solution spaces is computation time and results are not guaranteed to be valid.

Problems will often occur at the point of the simulation where the data is produced. Solution time is a secondary aspect of the simulation in comparison to validity, being the most important. A solution need not be slow to be accurate, and often a slow solution means incorrect boundary conditions, solution approach, models, or mesh. If problems arise, scrutinize the choice of models, the mesh, and the boundary conditions. Results must be scrutinized and should be assumed erroneous until proven contrary. Checking the entire range of the 2-D parameter maps at several applied biases will validate a given model. Parameters to inspect include the cross-section for band diagram, velocity field characteristics, drain current versus drain voltage, and gate biases versus drain current curves. Results from the simulator must be carefully examined with the device's physical picture and experimental data in mind. Drain currents should be normalized to device dimensions to ensure feasible current densities. Additionally, gate depletion and 2-DEG thickness should also be investigated. After thorough inspection and a model validation, some parameters may still be indeterminate due to the initial solution and material specifications.

Solutions from the Silvaco software are saved in .str files. The data is saved in a text format and the standard viewer for the Silvaco software is Tonyplot. Tonyplot can

be invoked from the Atlas command window through code or through the UNIX prompt. When invoking Tonyplot form the Atlas command window, it is convenient to associate a .set file that instantiates a given plot and labels associated axis. The *save* command is used to begin the logging of data into a specified .str file with the *outf* option, logging will continue until either a *log off* command or another *save* command. The *save out=xxx.str.* statement logs a set of standard variables that can then be modified with the *output* command. Numerous variables can be added to the log file and the Atlas manual should be referenced for a more complete listing of default and additional variables, as the application would dictate the output of interest.

3.4.2 Modeling GaN/InN MODFET's

With the understanding of key issues to achieving a high performance MODFET's, simulation of MODFET's will become the focus. Silvaco software is a Computer Aided Design (CAD) package for electronic device applications. In addition to basic structural design elements present in any CAD package the added benefit of simulating device fabrication, operation, and energy structure has been incorporated into the software. The software allows users to create simple models that combine non-linear differential equations for carrier generation, recombination, diffusion, and drift, as a function of the lattice and carrier temperature. Computational Fluid Dynamics (CFD) based CAD packages apply the same principles for fluid flow and aqueous chemical reactions. Software similar to Atlas could be coined as Computational Quantum Dynamics (CQD) packages.

3.4.2.1 MODFET Geometry

MODFET's come in many layouts depending on the application. A standard transistor layout for MODFET's is the t-gate pattern. The channel separates the source and drain, with the gate place slightly to the source side in the channel. The distance from the gate to the channel, in the z-direction, dictates the gate depletion region field interaction with the channel current. Placing the gate closer to the channel without changing the barrier thickness would cause greater depletion of the 2-DEG. Devices can be made normally on or off depending on the gate placement. Another transistor layout associated with power amplifiers is generally reserved for compact transistors that require large gate lengths. These transistors have the source, drain, and gate arranged as intertwined fingers. This decreases the space requirements of the device and allows for large drain current volumes. The design chosen for this simulation was a simple t-gate cross section.

3.4.2.2 MODFET Characteristics

The device in the simulation was designed as follows. The 100 nm gate is situated 225 nm from the source in a 700 nm channel. The Pt gate metallization was assumed to be 5 nm thick with a workfunction of 5.63 eV. The source and drain were assumed to be thermally diffused Ohmic contacts, penetrating the MODFET structure to a depth of 20 nm. The InGaN barrier was assumed to be 5% In, with uniform doping at $5X10^{17}$ cm^{-3} and a thickness of 10 nm with a 1 nm undoped setback layer. The buffer is InN assumed to be uniformly doped at $1X10^{16}$ cm^{-3}. As for thermal considerations, the source and 100 nm below the surface of the device were assumed to be at 300 K.

3.4.2.3 Mobility Considerations

In FET devices, the mobility field and velocity field relationships are integral to device operation as they factor into the drain current response. As mentioned previously the mobility will initially limit the current response up to a certain voltage where the velocity saturation limits the current flow. Additionally, the source-gate side of the FET's current is limited by the mobility, while the gate-drain side is limited by the velocity saturation. A saturating velocity field relationship was used for the simulation; the corresponding Atlas command is fldmob, enabling a parallel field dependent mobility, with the evsatmod parameter set to 0 (represents a standard velocity field saturation curve with no peak). By setting evsatmod to 1, the saturation has an overshoot peak that allots for negative differential velocity (NDV), and setting evsatmod to 2 would enable a simple velocity field curve. Extreme care must be taken with NDV as it can lead to instabilities in device simulation and should be reserved for Gunn type devices. The material parameters used in calculation of the simulated device are presented as Table 5 – Silvaco Material Parameters.

Table 5 – Silvaco Material Parameters

III-N *(Units)*	χ *(eV)*	μ_n *(cm^2/Vs)*	μ_p *(cm^2/Vs)*	N_C *(cm^{-3})*	m_e	τ_n *(s)*	τ_p *(s)*	v_{SAT} *(cm/s)*
GaN	4.1	1000	100	$8.3X10^{18}$	0.22	$1X10^{-9}$	$1X10^{-9}$	$2X10^{7}$
InN	5.75	3200	250	$8X10^{17}$	0.1	$1X10^{-9}$	$1X10^{-9}$	$3.5X10^{7}$

Other available velocity-field options are the Caughey-Thomas Model (Atlas command: analytic), accounting for concentration and temperature dependency, the Dorkel-Leturq Model (Atlas command: ccsmob), accounting for concentration, doping, and temperature dependency appropriate for power devices, and the Lombardi (Atlas command: CVT) and Yamaguchi, accounting for perpendicular and parallel electric field, carrier dependency, and in the case of CVT the additional effect of temperature dependency. MODFET's often have a recessed or mesa gate, both of which would require not only the parallel electric field dependency for the channel current, but also the perpendicular electric field due to the displacement of the gate in these structures. The CVT model was chosen for the simulation for its diversity in carrier effects, it takes into account temperature, field, and concentrations on carrier dynamics.

The MODFET model was built in Atlas according to the material and physical parameters presented above. Three output files were generated to ensure the validity of the MODFET model, a 2-d representation of the intrinsic device parameters, with cross sections, a drain current versus drain voltage curve, and a gate bias versus drain current curve. The 2-d representation of the $In_{0.05}Ga_{0.95}N$/InN MODFET is presented as Figure 62 - MODFET Energy Band Diagram, in which panel (a) depicts the material and contact boundaries, panel (b) represents the conduction band edge from the gate through the buffer, and panel (c) represents the valence band edge through the barrier and into the buffer. As can be seen by comparing panels (b) and (c), the conduction band follows the valence band closely, with approximately a 3.2 eV bandgap in the $In_{0.05}Ga_{0.95}N$ barrier and approximately 1.8 eV bandgap in the InN.

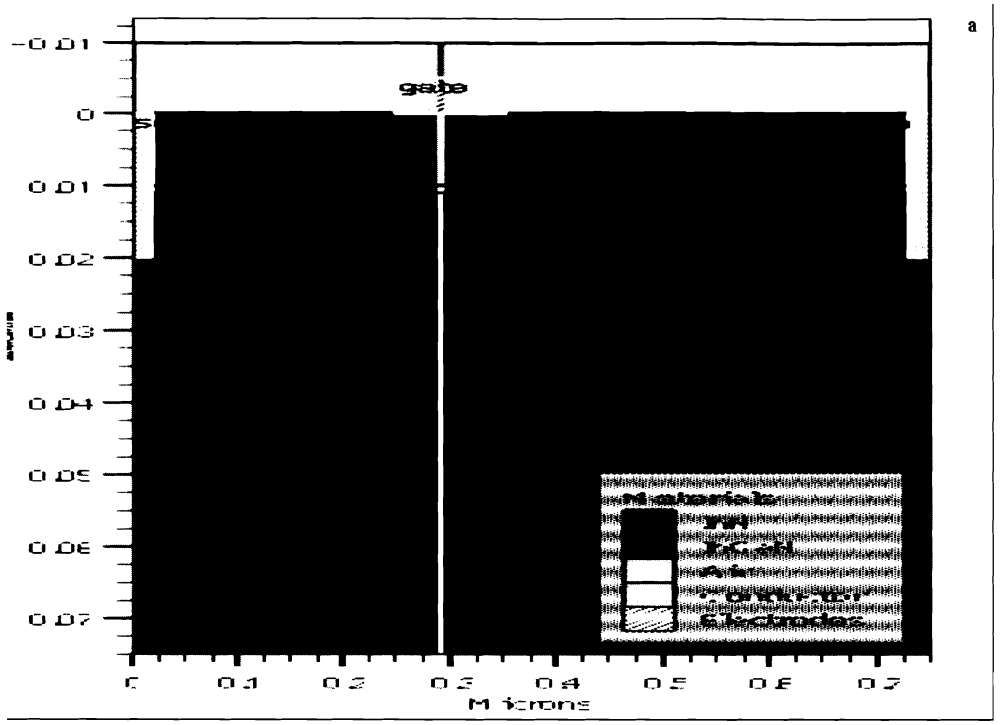
a
gate
Microns

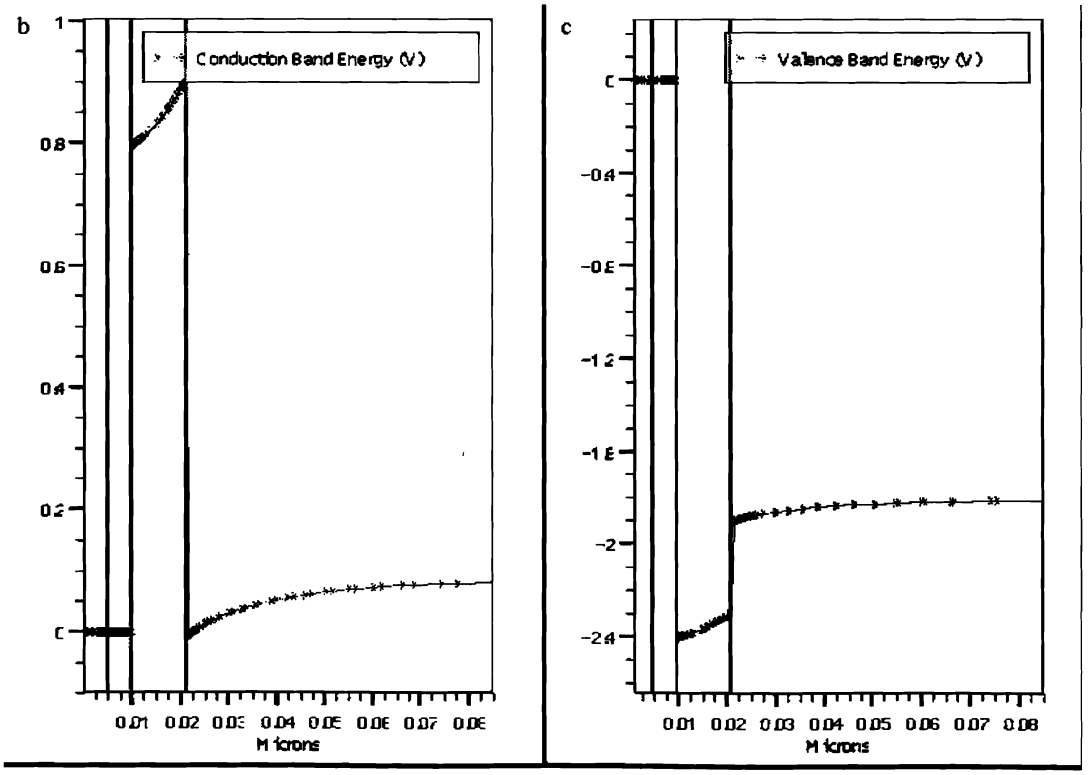
b
Conduction Band Energy (V)
Microns
c
Valence Band Energy (V)
Microns

Figure 62 - MODFET Energy Band Diagram

Silvaco 2 dimensional device profile from $In_{0.05}Ga_{0.95}N$/InN MODFET in equilibrium steady state condition (V_g=0, V_{ds}=0), (a) material and contact boundaries, (b) Conduction band edge from the surface to the buffer, (c) Valence band edge from the surface to the buffer.

It can also been seen from Figure 62 - MODFET Energy Band Diagram that there is an abrupt discontinuity in the conduction band edge at the heterointerface, and a quantum well has formed in the InN buffer. In Figure 63 - MODFET Electron Concentrations under biasing, the device is seen with a bias of -1 volt applied to the gate and a grounded drain. Panel (a) shows the electron concentration in the MODFET, while panel (b) and (c) show the corresponding conduction and valence bands under the gate (follows vertical black line).

a

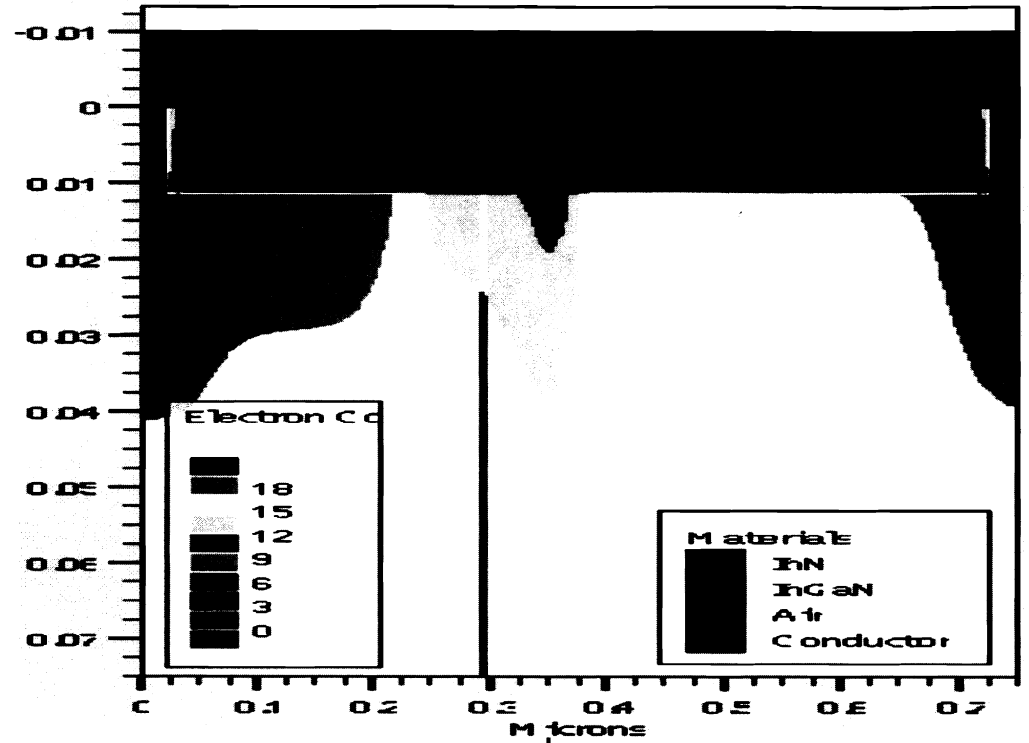
-0.01
0
0.01
0.02
0.03
0.04
0.05
0.06
0.07
Electron C
18
15
12
9
6
3
0
Material
InN
InGaN
Air
Conductor
0
0.1
0.2
0.3
0.4
0.5
0.6
0.7
Microns

b.

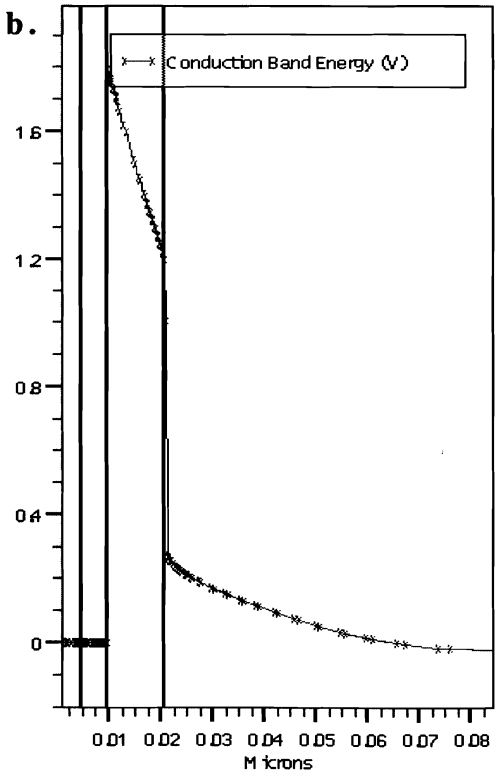
Conduction Band Energy (V)
1.6
1.2
0.8
0.4
0
0.01
0.02
0.03
0.04
0.05
0.06
0.07
0.08
Microns

c.

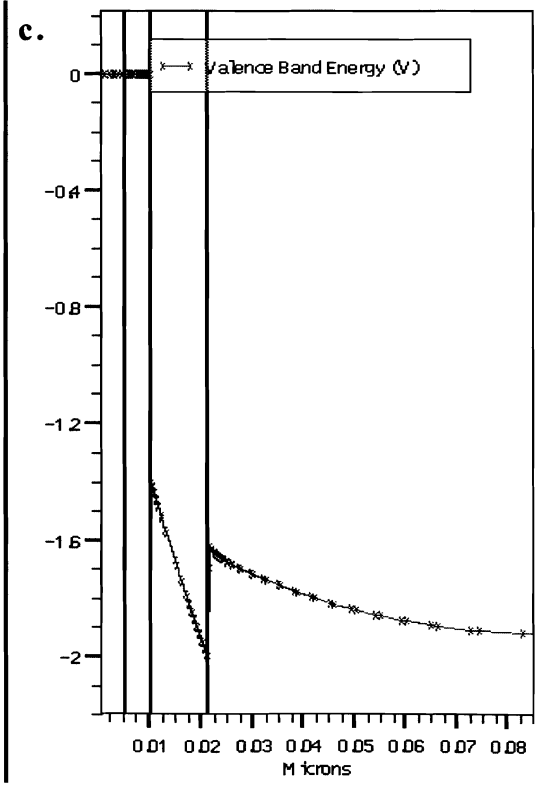
Valence Band Energy (V)
0
-0.4
-0.8
-1.2
-1.6
-2
0.01
0.02
0.03
0.04
0.05
0.06
0.07
0.08
Microns

Figure 63 - MODFET Electron Concentrations under biasing

Silvaco 2 dimensional device profile from $In_{0.05}Ga_{0.95}N/InN$ MODFET in active operation (V_g=-1V, V_{ds}=0V), (a) material and contact boundaries, (b) Conduction band edge from the surface to the buffer, (c) Valence band edge from the surface to the buffer.

The electron concentration under the barrier is depleted and the band profiles are less flattened, consistent with an unpopulated 2-DEG. After verifying the band profiles in the MODFET structure, the drain current versus drain voltage curves were produced as Figure 64 - Drain current curves for an $In_{0.05}Ga_{0.95}N/InN$ MODFET.

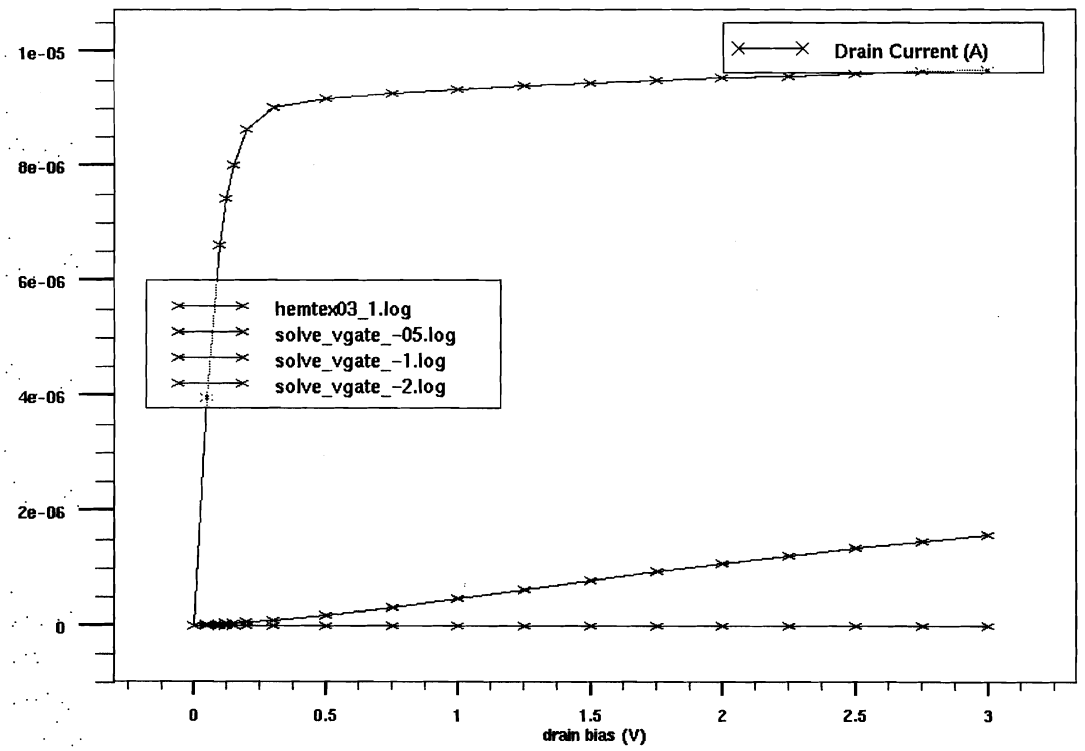

Figure 64 - Drain current curves for an $In_{0.05}Ga_{0.95}N/InN$ MODFET

The lines represented are, from top to bottom, Vg = 0V, Vg = -0.5V, Vg = -1V, and Vg = -1.5V. Curves were constructed in parallel from multiple decks.

The drain current curves, in Figure 64 - Drain current curves for an $In_{0.05}Ga_{0.95}N/InN$ MODFET were produced from multiple deck files. Each deck file simulated one gate bias. Processing the gate bias points in separate deck files on separate processors versus serial computing each gate bias in a single deck file on one processor was found to be consistent. Both methods show a quick collapse of the drain current response and a linear response at higher voltages, though the parallel deck file seems to be cleaner than the sequential file.

Figure 65 - Drain Current Curves Constructed from a Single Deck is presented as an ideal set of drain current voltage curves that were produced from a 15 nm GaN/InN MODFET doped at 10^{19} cm^{-3} in the barrier and $5X10^{16}$ cm^{-3} in the buffer,

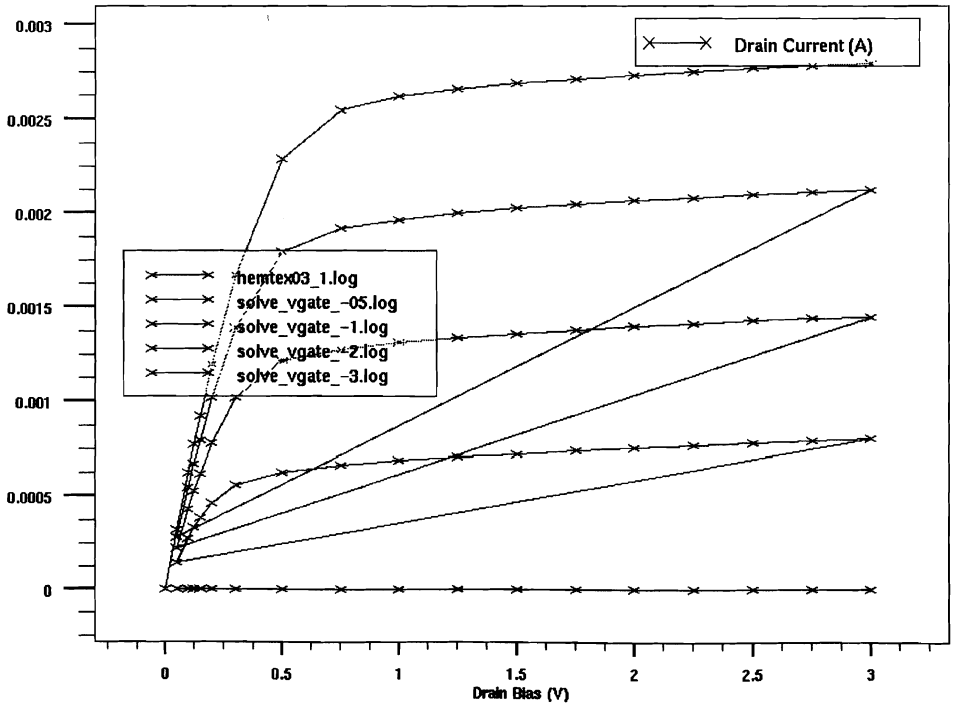

Figure 65 - Drain Current Curves Constructed from a Single Deck

Drain current curves for a 15 nm 10^{19} cm^{-3} GaN barrier on $5X10^{16}$ cm^{-3} InN buffer MODFET. Gate biases are as posted on the chart, starting from the top, $V_g = 0V$, $V_g = -0.5V$, $V_g = -1V$, $V_g = -2V$, and $V_g = -3V$.

but otherwise identical to the $In_{0.05}Ga_{0.95}N$/InN MODFET. Extraneous lines are evident at the end of the drain current profiles that are typical artifacts associated with computing MODFET characteristics in a single deck file. Figure 66 - Drain Current versus Gate Bias for an $In_{0.05}Ga_{0.95}N$/InN MODFET presents the drain current with a constant drain bias of 0.5 V as a function of the applied gate bias.

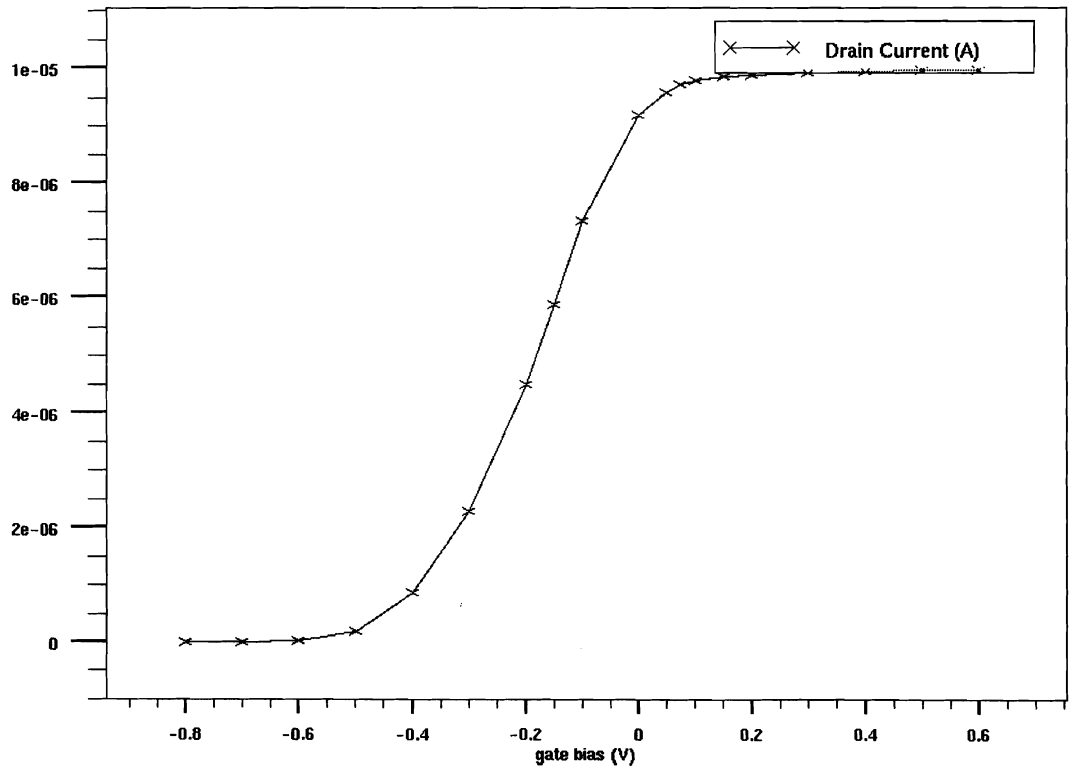

Figure 66 - Drain Current versus Gate Bias for an $In_{0.05}Ga_{0.95}N$/InN MODFET

No differences were seen in serial or parallel processing of the drain current versus the gate voltage curves. At negative gate biases greater than 0.4V, there is essentially no current, and positive gate biases demonstrate large current flow. This is congruent with the notion that a reverse biased Schottky junction should not conduct at reverse biases and the drain current should be ever diminishing for increasing negative gate biases when neglecting leakage current. The binary GaN/InN MODFET demonstrates a different drain current behavior with applied bias, Figure 67 - Drain current curves for a GaN/InN MODFET.

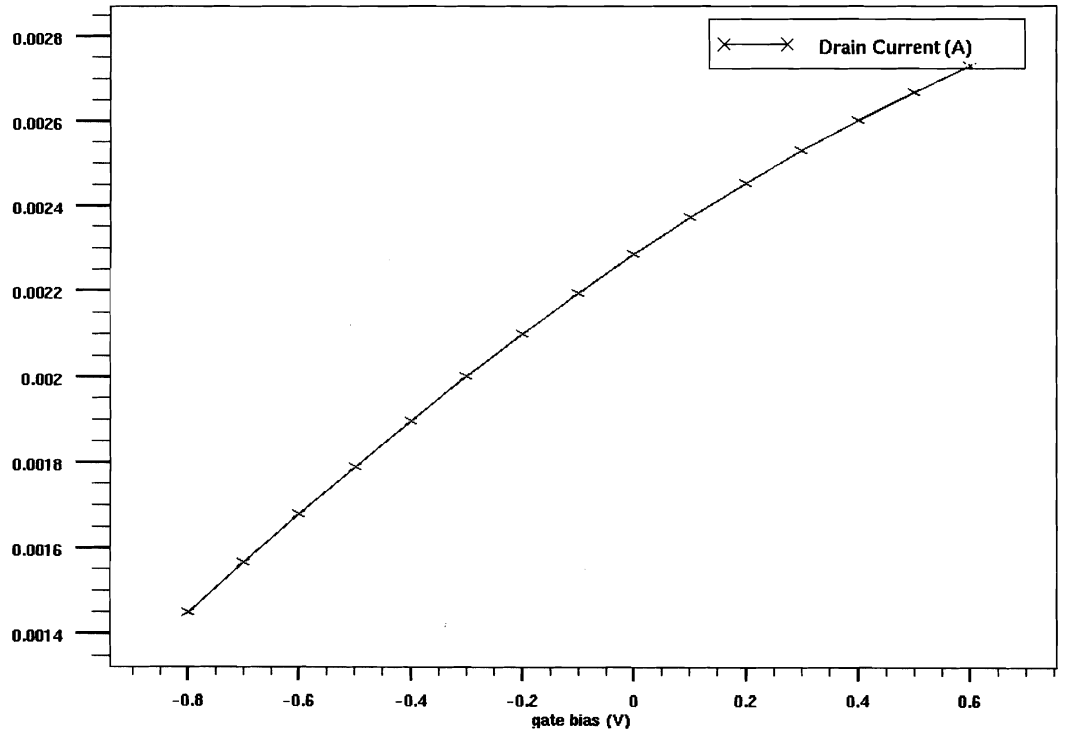

Figure 67 - Drain current curves for a GaN/InN MODFET

In creating a device model for a GaN-InGaN MODFET, certain aspects of the model became more important. The mesh is the essential backbone of the device structure; without a properly designed mesh proceeding to materials definitions is pointless. Regridding is difficult to perform and requires a sparse matrix in the beginning. Attempts to regrid the mesh when the mesh is near the node ceiling is not advisable, as introducing triangles that are more obtuse will result in a breaching of the node ceiling and halt the simulation. Caution should also be used with the eliminate statements, as portions of the mesh can vary too quickly and lead too poor simulation results. Material definitions are somewhat straight foreword when dealing with binary compounds and any device should be implemented in binary compounds first. After acceptable results are achieved then proceed to migrating into the tertiary or higher compounds by changing appropriate material parameters. If problems occur, utilize the *models print* statement to identify the parameters that may be amiss. Comparing the tertiary *models print* results to the *models print* results of the binary compound can be extremely effective debugging tool. The materials statement should be used to assign values to any bad variables. A c-file can be constructed for new materials to assign all parameters and even account for the alloy composition set in the *region ... x.comp* statement. Contact assignment and doping profiles are adequately addressed in the Silvaco manual. Solutions must be scrutinized thoroughly in order to ensure valid results, if the proceeding elements are definitely correct then investigate either velocity-field models or solution approaches.

Silvaco can be used to compliment standard experimental data in many ways. Not only does the simulator allow for device performance evaluation a prior to any experimental work, but it can be used in post-analysis work to gain understanding into non-traditional materials, such as the III-Nitrides. The physics of defects could be implemented using the Silvaco package to model devices with defect trapping characteristics located in the bulk, at the interface, or distribution of traps in the bulk and at the interface. Silvaco allows the user to define a unique defect structure by assigning a position in the bandgap, a spatial distribution in the device, a capture cross-section, and capture delay time. Silvaco can also be used to simulate the thermal, optical, and limited mechanical aspects of any device structure.

4 Conclusions

4.1 Schottky

It is very difficult to achieve high quality contacts on GaN. Numerous effects obscuring device properties, there is definitively bulk and surface contribution to leakage current and conduction anomalies. Field emission, Frenkel-Poole conduction, among other conduction mechanisms, were observed in the devices studied by current-voltage measurements. Combination of CV and IV measurements confirmed reported ranges of N_D for TE, TFE, and FE conduction as a function of temperature. Room temperature conduction is mainly TFE for all but the best devices, in which TE dominates. Medium quality devices generally demonstrate FE at reverse biases and low forward biases, with TFE conduction for forward biases. Cooling devices to LN_2 temperatures improves thermionic character, introduces a low forward bias FE component (when not present in room temperature devices), and reduces the observed leakage. Any temperature variant measurements are best performed in a cryostat with a bonded device.

In special samples, the observed conduction is attributable to other defect related conduction mechanisms. Poor quality devices produce FE, among other anomalous conduction mechanisms, at room temperature for forward and reverse biases in near

symmetry. Etching devices in molten KOH can improve device properties up to a point, beyond which there is no proposed post-process for reliable contact formation. With potassium hydroxide etching, forward conduction mechanisms became more TE in character and leakage current was diminished. Device improvement is proposed to be due to creating a purer c-plane, passivating the surface with an oxide, or isolating the highly conductive semiconductor regions from the contact. Leakage current and forward transport are not coupled in their improvement (See Figure 43 - Saturation Current vs. Diode for SVT 1460 1 min etch and Figure 44 - Series Resistance vs. Diode for SVT 1460 1 min etch). There was no correlation between material properties identified by other non-electrical techniques, such as X-ray, TEM, or PL. Consideration must be given to the electrical test fixture's vibrational / electrical isolation and device influences from illumination, thermal gradients, acoustic, and Rf energy. Growth related approaches are the best course of action for improving the properties of Schottky contacts and resultant devices.

4.2 CAFM

Conductive atomic force microscopy (CAFM) is a robust technique capable of providing a wealth of information for electronic device materials. The Dimension 3100 enabled the study of GaN anomalous current conduction. Improvements that would extend the utility of the Dimension 3100 include: extended applied bias range, pulse IV, automated topography spectra, extended bias, photoluminescence current spectroscopy,

and transient capacitance techniques. A categorical list of conclusions is presented for ease.

4.2.1 Topography

1) CAFM is a good predictor for device quality
    a. Tip metallization and cantilever style affects measured current.
    b. Scan rates can affect measured current.
    c. Samples that have low leakage and strong thermionic emission in Schottky devices, display no conduction at high reverse biases and high (generally uniform) conduction at small forward biases.
    d. TUNA module and CAFM module provide consistent data.
    e. High quality samples have extremely high threshold voltages for the CAFM measurements; voltage extension must be enabled to investigate high quality III-N's and other wide bandgap semiconductors, specifically investigated SiC and ZnO (See 3.1.1 SVT 429).
        i. MOCVD and HVPE samples rarely showed as-deposited conduction at forward or reverse biases, though etching would produce the expected conduction responses with a high degree of memory (See Figure 54 - SVT 1460 Memory and Degrading Conduction).
        ii. ZnO and GaN annealed in various atmospheres showed a change in conduction behavior in CAFM and macroscopic contacts.

2) Leakage is highly localized and can be uniform or nonuniform (See Figure 50 - Ga-polar Comparison of SVT 381 and SVT 666 and Figure 52 - N-polar Comparison of SVT 618 & SVT 680).
    a. In as-grown surfaces: leakage manifests in small areas and increases the conductivity of surrounding surface features, the extent of leakage increasing with applied bias.
    b. Surface features with off c-plane orientations are highly susceptible to increased conduction.
    c. Etched surfaces primarily conduct through pits (side walls and plateaus) and surrounding structures.
3) Scanning surfaces changes the nature of conduction through the film.
    a. Recently Etched samples have strong mixed conductivity at zero tip-sample biases.
    b. Current conduction rapidly degrades with multiple scans.
    c. Forward biases are more affective at reducing the conductivity; reverse biases seem to be more effective at restoring conduction.
    d. Current conduction becomes highly localized after multiple scans and the onset of reduced conductivity.
    e. Reduced Conductivity was seen to be reversible and irreversible on c-plane surfaces – indicating possibly more than one mechanism at work.

f. Some samples seemed to become unstable after CAFM imaging (SVT 889 appeared to have accumulated a white dendritic structure and conductivity was highly irregular).

4) Hexagonal features in Ga-rich Ga-polar films, previously identified as IDB's using EFM, show forward and reverse biased conductivity.

5) EFM measurements do not correlate surface potential differences to the presence of leakage, though potential differences may locally enhance the leakage conduction.

4.2.1.1 Uniformity versus Nonuniformity

1) Samples of similar growth conditions were found to have dissimilar conduction microstructures as compared by CAFM.

   a. Some samples have patchy conduction, SVT 381 and SVT 429, while others have uniform conduction, SVT 750 and SVT 1026.

   b. Uniform samples generally have poor as-deposited electrical characteristics, leaky gates, low barrier heights, and or elevated carrier concentrations.

   c. Leakage is uniformly distributed in some samples while other samples show non- uniform leakage and forward conduction breakdown.

2) The sample investigated with a surface fix (SVT 429) had a low density of non-uniform leakage, good TE forward conduction breakdown, a low mobility, and high series resistance.

4.2.1.2 No correlation between DD and LFD

1) Ga and N polar samples were investigated with CAFM, in an effort to correlate TEM dislocation density information to leakage centers.
    a. TEM identification of extended defects has no direct correlation with magnitude or extent of leakage observed by CAFM or in macroscopic Schottky contacts.
    b. The most plausible situation is extended defects are "activated" by electrically active point defects.

4.2.2 CAFM Spectra

1) SVT 889 and SVT 885 – MBE overgrowth on HVPE template shows a correlation between forward and reverse bias conduction at some hillock centers.
    a. Hillocks are known to have a screw component.
    b. Hillocks have individual activation energies, as results show more hillock features conducting at higher biases.
    c. Amphoteric defects are observed, i.e. conduct at forward and reverse biases.
2) SVT 885, the AlGaN MODFET sample exhibited larger regions of conduction than SVT 889.
    a. Forward bias leakage would consume the hillocks and span into the adjacent c-plane surface.

b. Increased conduction could be the result of a higher concentration of point defects; strain enhanced conductivity, and / or compositional Al variance in the film.

3) SVT 1016 demonstrated nearly ideal Schottky's for As-Deposited and KOH etched samples.

a. CAFM spectra had multiple slopes for the different spatial locations and the trace – retrace.

b. Very little leakage current; possibly the instrument's noise floor.

c. Mainly TFE and FE conduction.

d. Possibly Hopping Conductivity or Schottky / Frenkel-Poole (depending on location). Demonstrates the importance of T measurements.

With the above results reiterated, extended defects and IDB's alone cannot account for the leakage current observed in GaN diodes. Defect complexes may be responsible for observed conduction anomalies, and the elusive culprit of yellow-band luminescence in GaN thin films. Oxygen defect complexes have been identified in literature that couple with Ga-vacancies to create acceptor pairs. Conglomerates of these defects in correct distributions could lead to p-n rods, directional strain enhanced conduction, near band edge centers, or hopping conductivity pathways. Appling fields to these structures would result in mobile charge in the diffusion limited space charge region around the electrically active defect complexes, whether they are activated edge or open core screw, full core screw, mixed dislocations, or Holtz IDB's. For the true nature

of defects to be identified by name and energetic position, DLTS reference samples would have to be established, or DLTS type techniques would have to implemented on the CAFM module.

Vita

Joshua Spradlin was born in Lynchburg, Virginia on November 13th 1978. In 1997, he graduated from Gloucester High School, in Gloucester, Virginia. He obtained a Bachelors of Science in Electrical Engineering and Physics and a minor in Mathematics from Virginia Commonwealth University 2001. He was a teacher's and research assistant while undertaking graduate studies in Dr. Morkoç's laboratory. He began working for Setagon Inc. as a thin film process engineer designing porous drug eluting devices in the spring of 2004. His first patent was filed in August 2004 with Setagon Inc.

References

[1] H. Morkoç, *Nitride Semiconductors and Devices* (Springer-Verlag Berlin Heidelberg, Germany, 1999).
[2] S. Yoshida and J. Suzuki, J. Cryst. Growth **191**, 279-81 (1998).
[3] T. Egawa, H. Ishikawa, K. Yamamoto, T. Jimbo, and M. Umeno, Nitride Semicond. Symp. Mater. Res. Soc., 1101-6 (1998).
[4] B. Deb, A. Ganguly, S. Chaudhuri, B. R. Chakraborti, and A. K. Pal, Mat. Chem. Phys. **74**, 282-8 (2002).
[5] B.R. Nag, *Electron Transport in Compound Semiconductors* (Springer-Verlag Berlin Heidelberg, Germany, 1980).
[6] Boer, *Survey of Semiconductor Physics- Electrons and Other Particles in Bulk Semiconductors* (Van Nostran Reinhold, USA, 1990).
[7] Seeger, *Semiconductor Physics – An Introduction* (Springer-Verlag Berlin Heidelberg, New York, USA, 1989).
[8] S. M. Sze, *Physics of Semiconductor Devices, 2nd Ed.* (John Wiley & Sons New York, USA, 1981).
[9] Runyan, *Semiconductor Measurements & Instrumentation* (McGraw Hill, USA 1975).
[10] B. S. Shelton, M. M. Wong, T. G. Zhu, C. J. Eiting, D. J. H. Lambert, D. E. Lin, H. K. Kwon, and R. D. Dupuis, Phys. Stat. Sol. (a) **176**, 213 (1999).
[11] S. Keller and S. P. DenBaars, J. Cryst. Growth **248**, 479–486 (2003).
[12] M. J. Manfra, N. G. Weimann, J. W. P. Hsu, L. N. Pfieffer, K. W. West, S. Syed, H. L. Stormer, W. Pan, D. V. Lang, S. N. G. Chu, G. Kowach, A. M. Sergent, J. Caissie, K. M. Molvar, L. J. Mahoney, R. J. Molnar, J. Appl. Phys. **92**(1), 338 (2002).
[13] L. Liu and J.H. Edgar, Mat. Sci. Eng. **R 37**, 61–127 (2002).
[14] N. W. Ashcroft and N. D. Mermin, *Solid State Physics* (Saunders College Publishing, Orlando Florida 1976).
[15] O. Ambacher, J. Majewski, C. Miskys, A. Link, M. Hermann, M. Eickhoff, M. Stutzmann, F. Bernardini, V. Fiorentini, V. Tilak, B. Schaff, and L. F. Eastman, J. Phys.: Cond. Mat. **14**, 3399–3434 (2002).
[16] M. Garter, J. Scofield, R. Birkhahn, A. J. Steckl, Appl. Phys. Lett. **74**(2), 182-4 (1999).
[17] K-H. Shim, M. C. Paek, B. T. Lee, C. Kim, and J. Y. Kang, Appl. Phys. A **A72**(4), 471-4 (2001).
[18] J. Schalwig, G. Muller, U. Karrer, M. Eickhoff, O. Ambacher, M. Stutzmann, L. Gorgens, and G. Dollinger, Appl. Phys. Lett. **80**(7), 1222-4 (2002).

[19] A. Denisenko, A. Aleksov, I. Daumiller, and E. Kohn, 58th DRC. Device Research Conference. Conference Digest (Cat. No.00TH8526). IEEE., 75-6 (2000).
[20] R. Gaska, M. S. Shur, A. D. Bykhovski, J. W. Yang, M. A. Khan, V. V. Kaminski, and S. M. Soloviov, Appl. Phys. Lett. **76**(26), 3956-8 (2000).
[21] P. Boguslawski, E. L. Briggs, and J. Bernholc, Phys. Rev. B **51**(23), 255-8 (1995).
[22] J. W. P. Hsu, M. J. Manfra, D. V. Lang, S. Richter, S. N. G. Chu, A. M. Sergent, R. N. Kleiman, L. N. Pfeiffer, and R. J. Molnar, Appl. Phys. Lett. **78**(12) 1685-7 (2001).
[23] K. Shiojima, J. M. Woodall, C. J. Eiting, P. A. Grudowski, and R. D. Dupuis, J. Vac. Sci. Technol. B **17**(5), 2030-3 (1999).
[24] A. T. Blumenau, J. Elsner, R. Jones, M. I. Heggie, and S. Oberg, J. Phys.: Condens. Matter 12 (2000) 10223-33.
[25] J. Elsner, Th. Frauenheim, M. Haugk, R. Gutierrez, R. Jones, and M. I. Heggie, MRS Internet J. Nitride Semicond. Res. **4S1**, G3.29 (1999).
[26] G. P. Dimitrakopulos, Ph. Komninou, J. Kioseoglou, Th. Kehagias, E. Sarigiannidou, A. Georgakilas, G. Nouet, and Th. Karakostas, Phys. Rev. B **64**, 245325-12 (2001).
[27] D. Doppalapudi, E. Iliopoulos, S. N. Basu, and T. D. Moustakas, J. Appl. Phys. **85**(7), 3582-3589 (1999).
[28] M. E. Cage, J. Phys.: Condens. Matter **1**, 5531-5534 (1989).
[29] D. Huang, F. Yun, M. A. Reshchikov, D. Wang, H. Morkoç, D. L. Rode, L. A. Farina, Ç. Kurdak, K. T. Tsen, S. S. Park, and K. Y. Lee, Solid-State Electron **45**, 711-715 (2001).
[30] Yu and Cardona, *Fundamentals of Semiconductors Physics and Materials Properties* (Springer-Verlag Berlin Heidelberg, Germany, 1996).
[31] M. Misra, A. V. Sampath, and T. D. Moustakas, Appl. Phys. Lett. **76**(8), 1045-7 (2000).
[32] S. K. Noh and P. Bhattacharya, Appl. Phys. Lett. **78**(23), 3642-4 (2001).
[33] Devreese and van Doren, *Linear and nonlinear Electron Transport in Solids* (Plenum Press, New York, 1976).
[34] N. Markovi, C. Christiansen, D. E. Grupp, A. M. Mack, G. Martinez-Arizala, and A. M. Goldman, J. Phys.: Condens. Matter **1**, 1162 (2000).
[35] Z-Q. Fang, J. W. Hemsky, D. C. Look, M. P. Mack, R. J. Molnar, and G. D. Via, "Electron irradiation induced trap in n-type GaN", Nitride Semicond. Symp. Mater. Res. Soc., 881-6 (1998).
[36] S. A. Goodman, F. D. Auret, F. K. Koschnick, J-M. Spaeth, B. Beaumont, and P. Gibart, Mat. Sci. Eng. B **B71**(1-3), 100-3 (2000).
[37] A. Y. Polyakov, N. B. Smirnov, A. V. Govorkov, A. A. Shlensky, M. G. Mil'vidskii, S. J. Pearton, N. N. Faleev, V. T. Bublik, K. D. Chsherbatchev, A. Osinsky, P. E. Norris, V. A. Dravin, and R. G. Wilson, IEEE. J. Elec. Mat. **31**(5), 384-90 (2002).
[38] Ching-Wu Wang, J. Vac. Sci. Technol. B **20**(5), 1821-6 (2002).
[39] A. Hierro, D. Kwon, S.A. Ringel, M. Hansen, J.S. Speck, U.K. Mishra, and S.P. DenBarrs, Appl. Phys. Lett. **76**(21), 3064-6 (2000).
[40] C. B. Soh, D. Z. Chi, A. Ramam, H. F. Lim, and S. J. Chua, Mat. Sci. Semicond. Proc. **4**(6), 595-600 (2001).

[41] P. Muret, A. Philippe, E. Monroy, E. Munoz, B. Beaumont, F. Omnes, and P. Gibart, Mat. Sci. Eng. B **B82**(1-3), 91-4 (2001).
[42] P. Muret, A. Philippe, E. Monroy, E. Munoz, B. Beaumont, F. Omnes, and P. Gibart, J. Appl. Phys. **91**(5), 2998-3001 (2002).
[43] N. D. Nguyen, M. Germain, M. Schmeits, B. Schineller, and M. Heuken, J. Appl. Phys. **90**(2), 985-93 (2001).
[44] Y. Nakano, and T. Kachi, Appl. Phys. Lett. **79**(11), 1631-3 (2001).
[45] K. Shiojima and S. Sakai, *Proc. International Workshop on Nitride Semicond. Inst. Pure & Appl. Phys.*, 829-32 (2000).
[46] M. Schmeits, N. D. Nguyen, and M. Germain, J. Appl. Phys. **89**(3), 1890-7 (2001).
[47] C. B. Soh, D. Z. Chi, H. F. Lim, and S. J. Chua, *SPIE-Int. Soc. Opt. Eng. Int. Proc.* **4594**, 211-20 (2001).
[48] J. A. Venables, *Introduction to Surface and Thin Film Processes* (Cambridge University Press, Cambridge, UK, 2000).
[49] B. S. Simpkins, E. T. Yu, P. Waltereit, and J. S. Speck, J. Appl. Phys. **94**(3), 1448-53 (2003).
[50] K. Suzue, S. N. Mohammad, Z. F. Fan, W. Kim, O. Aktas, A. E. Botchkarev, and H. Morkoç, J. Appl. Phys. **80**(8), 4467-78 (1996).
[51] D. F. Storm, D. S. Katzer, S. C. Binari, E. R. Glaser, B. V. Shanabrook, and J. A. Roussos, Appl. Phys. Lett. **81**(20), 3819-21 (2002).
[52] L. S. Yu, Q. Z. Liu, Q. J. Xing, D. J. Qiao, S. S. Lau, and J. Redwing, J. Appl. Phys. **84**(4), 2099-104 (1998).
[53] S. Oyama, T. Hashizume, and H. Hasegawa, Appl. Surf. Sci. **190**(1-4), 322-5 (2002).
[54] V. M. Bermudez, J. Appl. Phys. **86**(2), 1170-1 (1999).
[55] W. Monch, J. Vac. Sci. Technol. B **17**(4), 1867-76 (1999).
[56] S. Picozzi, A. Continenza, G. Satta, S. Massidda, and A. J. Freeman, Phys. Rev. B **61**(24), 16736-42 (2000).
[57] I. Shalish, L. Kronik, G. Segal, Y. Shapira, M. Eizenberg, and J. Salzman, Appl. Phys. Lett. 77(7), 987-9 (2000).
[58] T. Sawada, Y. Ito, N. Kimura, K. Imai, K. Suzuki, and S. Sakai, Appl. Surf. Sci. **190**(1-4), 326-9 (2002).
[59] A. Barinov, L. Gregoratti, and M. Kiskinova, Phys. Rev. B **64**(20), 201312/1-4 (2001).
[60] S. Picozzi, G. Profeta, A. Continenza, S. Massidda, and A. J. Freeman, Phys. Rev. B **65**(16), 165316/1-7 (2002).
[61] A. Rizzi, Appl. Surf. Sci. **190**(1-4), 311-17 (2002).
[62] W. Liu, M. F. Li, S. J. Chua, N. Akutsu, and K. Matsumoto, Semicond. Sci. Technol.**14**(5), 399-402 (1999).
[63] D. C. Look and Z-Q. Fang, Appl. Phys. Lett. **79**(1), 84-6 (2001).
[64] E. G. Brazel, M. A. Chin, and V. Narayanamurti, Appl. Phys. Lett. **74**(16), 2367-9 (1999).
[65] C. I. Wu and A. Kahn, J. Vac. Sci. Technol. B **16**(4), 2218-23 (1998).
[66] J. Rennie, M. Onomura, S-Y. Nunoue, G-I. Hatakoshi, H. Sugawara, and M. Ishikawa, J. Cryst. Growth **189-190**, 711-15 (1998).

[67] T. G. G. Maffeis, M. C. Simmonds, S. A. Clark, F. Peiro, P. Haines, and P. J. Parbrook, J. Phys. D **33**(20), L115-18 (2000).
[68] T. G. G. Maffeis, S. A. Clark, P. R. Dunstan, S. P. Wilks, D. A. Evans, F. Peiro, H. Riechert, and P. J. Parbrook, Phys. Stat. Sol. A **176**(1), 751-4 (1999).
[69] Z. M. Zhao, R. L. Jiang, P. Chen, W. P. Li, D. J. Xi, S. Y. Xie, B. Shen, R. Zhang, Y. D. Zheng, Appl. Phys. Lett. **77**(20), 3140-2 (2000).
[70] A. Georgakilas, K. Tsagaraki, E. Makarona, G. Constantinidis, M. Adroulidaki, M. Kayambaki, E. Aperathitis, and N. T. Pelekanos, Mat. Sci. Semicond. Processing **3**(5-6), 511-15 (2000).
[71] C. I. Wu, A. Kahn, A. E. Wickenden, D. Koleske, R. L. Henry, J. Appl. Phys. **89**(1), 425-9 (2001).
[72] H. S. Venugopalan and S. E. Mohney, Appl. Phys. Lett. **73**(9), (1998).
[73] P. W. Deelman, R. N. Bicknell-Tassius, S. Nikishin, V. Kuryatkov, H. Temkin, Appl. Phys. Lett. **78**(15), 2172-4 (2001).
[74] K. Shiojima, D. T. McInturff, J. M. Woodall, P. A. Grudowski , C. J. Eiting, R. D. Dupuis, J. Elec. Mat. **28**(3), 228-33 (1999).
[75] H. S. Venugopalan, S. E. Mohney, J. M. DeLucca, and R. J. Molnar, Semicond. Sci. Technol.**14**(9), 757-61 (1999).
[76] Hui-Ching Hsin, Wen-Tai Lin, J. R. Gong, and Y. K. Fang, J. Mat. Sci.- Mat. Electron. **13**(4), 203-6 (2002).
[77] Yuanping Sun, X. M. Shen, J. Wang, D. G. Zhao, G. Feng, Y. Fu, S. M. Zhang, Z. H. Zhang, Z. H. Feng, Y. X. Bai, and Hui Yang, J. Phys. D – Appl. Phys. **35**(20), 2648-51 (2002).
[78] A. Motayed, A. V. Davydov, L. A. Bendersky, M. C. Wood, M. A. Derenge, Dong Feng Wang, K. A. Jones, and S. N. Mohammad, J. Appl. Phys. **92**(9), 5218-27 (2002).
[79] G. L . Chen, F. C. Chang, K. C. Shen, J. Ou, W. H. Chen, M. C. Lee, W. K. Chen, M. J. Jou, and C. N. Huang, Appl. Phys. Lett. **80**(4), 595-7 (2002).
[80] G. T. Dang, A. P. Zhang, M. M. Mshewa, F. Ren, J-I. Chyi, C-M. Lee, C. C. Chuo, G. C. Chi, J. Han, S. N. G. Chu, R. G. Wilson, X. A. Cao, and S. J. Pearrton, J. Vac. Sci. Technol. A **18**(4), 1135-8 (2000).
[81] B. Boratynski and B. Jankowski, *3rd International Conference `Novel Applications of Wide Bandgap Layers' IEEE.*, 185 (2001).
[82] M. Michalka, J. Skriniarova, F. Uherek, P. Gurnik, D. Donoval, and P. Kordos, *2001 International Symposium on Electron Devices for Microwave and Optoelectronic Application IEEE.*, 15-20 (2001).
[83] S-H. Lee, J-K. Chun, J-J. Hur, J-S. Lee, G-H. Rue, Y-H. Bae, S-H. Hahm, Y-H. Lee, and J-H. Lee, IEEE Elect. Dev. Lett. **21**(6), 261-3 (2000).
[84] J. K. Sheu, Y. K. Su, G. C. Chi, M. J. Jou, C. C. Liu, and C. M. Chang, Solid-State Electronics **43**(11), 2081-4 (1999).
[85] A. Sampath, H. M. Ng, D. Korakakis, and T. D. Moustakas, *Nitride Semicond. Symp. Mater. Res. Soc.*, 1095-9 (1998).

[86] E. Monroy, F. Calle, R. Ranchal, T. Palacios, M. Verdu, F. J. Sanchez, M. T. Montojo, M. Eickhoff, F .Omnes, Z. Bougrioua, and I. Moerman, Semicond. Sci. Technol. **17**(9), L47-54 (2002).
[87] J. Hilsenbeck, E. Nebauer, J. Wurfl, G. Trankle, and H. Obloh, Electron. Lett., **36**(11), 980-1 (2000).
[88] F. Omnes, N. Marenco, S. Haffouz, H. Lahreche, P. H. de Mierry, B. Beaumont, P. Hageman, E. Monroy, F. Calle, and E. Munoz, Mat. Sci. Eng. B **B59**(1-3), 401-6 (1999).
[89] J-S. Lee, J-W. Kim, J-H. Shin, S-B. Bae, Y-H. Lee, J-H. Lee, C-S. Kim, and J-E. Oh, J. Korean Phys. Soc. **39**(1), S181-4 (2001).
[90] L. Zhou, F. A. Khan, G. Cueva, V. Kuma, I. Adesida, M. R. Sardela, F. D. Auret , Appl. Phys. Lett. **81**(9), 1624-6 (2002).
[91] J. Wurfl, J. Hilsenbeck, E. Nebauer, G. Trankle, H. Obloh, and W. Osterle, Microelectron. Reliab. **40**, 1689-93 (2000).
[92] K. Shiojima, T. Sugahara, and S. Sakai, Appl. Phys. Lett. **74**(14), 1936-8 (1999).
[93] K. Shiojima, T. Sugahara, and S. Sakai, Appl. Phys. Lett. **77**(26), 4353-5 (2000).
[94] L. S. Yu, D. Qiao, L. Jia, S. S. Lau, Y. Qi, and K. M. Lau, Appl. Phys. Lett. **79**(27), 4536-8 (2001).
[95] H-K. Kim, T-Y. Seong, and C-R. Lee, J. Elec. Mat. **30**(3), 266-70 (2001).
[96] J-S. Jang, D-J. Kim, S-J. Park, and T-Y. Seong, J. Elec. Mat. **30**(2), 94-8 (2001).
[97] H. W. Jang, W. Urbanek, M. C. Yoo, and J-L. Lee, Appl. Phys. Lett. **80**(16), 2937-9 (2002).
[98] D. B. Ingerly, Y. A. Chang, and Y. Chen, *GaN and Related Alloys Symp. Mater. Res. Soc.* G6.49.1/6 (1999).
[99] J. K. Kim, J.-L. Lee, J. W. Lee, Y. J. Park, and T. Kim, J. Vac. Sci. Technol. B **17**(6), 2675-8 (1999).
[100] D. L. Hibbard, R. W. Chuang, Y. S. Zhao, C. L. Jensen, H. P. Lee, Z. J. Dong, R. Shih, and M. Bremser, J. Elec. Mat. **29**(3), 291-6 (2000).
[101] Z. Z. Bandic, P. M. Bridger, E. C. Piquette, and T. C. McGill, Appl. Phys. Lett. **73**(22), 3276-8 (1998).
[102] D-W. Kim, J. C. Bae, W. J. Kim, H. K. Baik, C. C. Kim, J. H. Je, and C. H. Hong, *Wide-Bandgap Electronic Devices Symp. Mat. Res. Soc. Proc.* **622**, T6.31.1-6 (2001).
[103] D-W. Kim, J. C. Bae, W. J. Kim, H. K. Baik, S-M. Lee, J. Vac. Sci. Technol. B **19**(3), 609-14 (2001).
[104] C. A. Dimitriadis, T. Karakostas, S. Logothetidis, G. Kamarinos, J. Brini, G. Nouet, Solid-State Electronics **43**(10), 1969-72 (1999).
[105] J. Kim, F. Ren, G. T. Thaler, M. E. Overberg, C. R. Abernathy, S. J. Pearton, and R. G. Wilson, Appl. Phys. Lett. **81**(4), 658-60 (2002).
[106] F. H. Pollak, Surf. Interface Anal. **31**(10), 938-53 (2001).
[107] H. Witte, A. Krtschil, M. Lisker, D. Rudloff, J. Christen, A. Krost, M. Stutzmann, and F. Schoz, *GaN and Related Alloys - 1999 Symp. Mat. Res. Soc. Symp. Proc.* **595,** W11.82.1-6 (2000).
[108] K. A. Rickert, A. B. Ellis, J. K. Kim, J-L. Lee, F. J. Himpsel, F. Dwikusuma, and T. F. Kuech , J. Appl. Phys. **92**(11), 6671-8 (2002).

[109] E. Danielsson, C-M. Zetterling, M. Ostling, K. Linthicum, D. B. Thomson, O-H. Nam, and R. F. Davis, Solid-State Electronics **46**(6), 827-35 (2002).
[110] P. J. Hartlieb, A. Roskowski, R. F. Davis, W. Platow, and R. J. Nemanich, J. Appl. Phys. **91**(2), 732-8 (2002).
[111] J. P. Long and V. M. Bermudez, Phys. Rev. B **66**(12), 121308-1-4 (2002).
[112] M. Misra, A. V. Sampath, and T. D. Moustakas, *GaN and Related Alloys - 1999 Symp. Mat. Res. Soc. Symp. Proc.* **595**, W11.2.1-6 (2000).
[113] A. P. Zhang, J. W. Johnson, B. Luo, F. Ren, S. J. Pearton, S. S. Park, Y. J. Park, and J-I. Chyi, Appl. Phys. Lett. **79**(10), 1555-7 (2001).
[114] J-R. Kim, H. Oh, H. M. So, J-J. Kim, J. Kim, C. J. Lee, and S. C. Lyu, Nanotechnol., **13**(5), 701-4 (2002).
[115] M. Stutzmann, O. Ambacher, M. Eickhoff, U. Karrer, A. Lima Pimenta, R. Neuberger, J. Schalwig, R. Dimitrov, P. J. Schuck, and R. D. Grober, Phys. Stat. Sol. B **228**(2), 505-12 (2001).
[116] Z-Q. Fang, D. C. Look, P. Visconti, D-F. Wang, C-Z. Lu, F. Yun, H. Morkoç, S. S. Park, and K. Y. Lee, Appl. Phys. Lett. **78**(15), 2178-80 (2001).
[117] U. Karrer, O. Ambacher, and M. Stutzmann, Appl. Phys. Lett. **77**(13), 2012-14 (2000).
[118] H. W. Jang, J.-H. Lee, and J.-L. Lee, Appl. Phys. Lett. **80**(21), 3955-7 (2002).
[119] J. S. Kwak, K. Y. Lee, J. Y. Han, J. Cho, S. Chae, O. H. Nam, and Y. Park, Appl. Phys. Lett. **79**(20), 3254-6 (2001).
[120] S. Picozzi, A. Continenza, and A. J. Freeman, Phys. Rev. B **59**(3), 1609-12 (1999).
[121] E. Monroy, F. Calle, T. Palacios, J. Sanchez-Osorio, M. Verdu, F. J. Sanchez, M. T. Montojo, F. Omnes, Z. Bougrioua, I. Moerman, and P. Ruterana, Phys. Stat. Sol. A **188**(1), 367-70 (2001).
[122] K. N. Lee, X. A. Cao, C. R. Abernathy, S. J. Pearton, A. P. Zhang, F. Ren, R. Hickman, and J. M. van Hove, Solid-State Electronics **44**(7), 1203-8 (2000).
[123] J. B. Webb, H. Tang, J. A. Bardwell, and P. Coleridge, Appl. Phys. Lett. **78**(24), 3845-3847 (2001).
[124] M. Suzuki, T. Kawakami, T. Arai, S. Kobayashi, Y. Koide, T. Uemura, N. Shibata, and M. Murakami, Appl. Phys. Lett. **74**(2), 275 (1999).
[125] N. Maeda, K. Tsubaki, T. Saitoh, T. Tawara, and N. Kobayashi, *Mat. Res. Soc. Symp. Proc.* **743**, 537 (2003).
[126] A. Demchuk, D. Olson, M. Shin, D. Olson, P Nussbaum, and A. Strom, Mat. Res. Soc. Symp. Proc. Vol. 743, pg. 543, 2003.
[127] Y-G. Zhou, B. Shen, J. Liu, H-M. Zhou, H-Q. Yu, R. Zhang, Y. Shi, Y-D Zheng, Acta Physica Sinica **50**, 1774-8 (2001).
[128] H. Kawai, M. Hara, F. Nakamura, T. Asatsuma, T. Kobayashi, and S. Imanaga, J. Cryst. Growth **189-190**, 738-41 (1998).
[129] D-W. Kim, D. H. Kim, T. W. Noh, E. Oh, H. C. Kim, and H-C. Lee, Sol. State Comm. **121**(11), 631-4 (2002).
[130] T. G. Zhu, D. J. H. Lambert, B. S. Shelton, M. M. Wong, U. Chowdhury, and R. D. Dupuis, Appl. Phys. Lett. 77(18), 2918-20 (2000).

[131] D. Mistele, J. Aderhold, H. Klausing, R. Rotter, O. Semchinova, J. Stemmer, D. Uffman, J. Graul, F. Eberhard, M. Mayer, M. Schauler, M. Kamp, and C. Ahrens, Semicond. Sci. Technol. **14**(7), 637-41 (1999).
[132] A.P. Zhang, G. Dang, F. Ren, X. A. Cao, H. Cho, E. S. Lambers, S. J. Pearton, R. J. Shul, L. Zhang, A. G. Baca, R. Hickman, and J. M. Van Hove, J. Electrochem. Soc. **147**(2), 719-22 (2000).
[133] X. A. Cao, S. J. Pearton, G. T. Dang, A. P. Zhang, F. Ren, and J. M. Van Hove, IEEE Trans. Electron Devices **47**(7), 1320-4 (2000).
[134] B. Rong, R. Cheung, W. Gao, M. M. Alkaisi, and R. J. Reeves, J. Vac. Sci. Technol. B **18**(6), 3467-70 (2000).
[135] H. W. Jang, J. K. Kim, C. M. Jeon, and J-L. Lee, MRS Internet J. of Nitride Semicond. Res. **7S1** (2002).
[136] H. W. Jang, C. M. Jeon, J. K. Kim, and J-L. Lee, Appl. Phys. Lett. **78**(14), 2015-17 (2001).
[137] L. D. Bell, R. P. Smith, B. T. McDermott, E. R. Gertner, R. Pittman, R. L. Pierson, and G. J. Sullivan, Appl. Phys. Lett. **76**(13), 1725-7 (2000).
[138] T. G. G. Maffeis, M. C. Simmonds, S. A. Clark, F. Peiro, P. Haines, and P. J. Parbrook, J. Appl. Phys. **92**(6), 3179-86 (2002).
[139] X. A. Cao, A. P. Zhang, G. T. Dang, F. Ren, S. J. Pearton, R. J. Shul, and L. Zhang, J. Vac. Sci. Technol. A **18**(4), 1144-8 (2000).
[140] J-S. Jang and T-Y. Seong, J. Appl. Phys. **88**(5), 3064-6 (2000).
[141] J. A. Bardwell, Y. Liu, S. Rauhala, P. Bouwhuis, P. Marshall, H. Tang, and J. B. Webb, Phys. Stat. Sol. **188** (1), 389-92 (2001).
[142] D. Mistele, T. Rotter, K. S. Rover, S. Paprotta, M. Seyboth, V. Schwegler, F. Fedler, H. Klausing, O. K. Semchinova , J. Stemmer, J. Aderhold , and J. Graul, Mat. Sci. Eng. B **B93**, 107-11 (2002).
[143] T. Rotter, D. Mistele, J. Stemmer, F. Fedler, J. Aderhold, J. Graul, V. Schwegler, C. Kirchner, M. Kamp, and M. Heuken, Appl. Phys. Lett. **76**(26), 3623-5 (2000).
[144] F. D. Auret, S. A. Goodman, F. K. Koschnick, J-M. Spaeth, B. Beaumont, and P. Gibart, *GaN and Related Alloys. Symposium. Mater. Res. Soc.*, G6.13/6 (1999).
[145] X. A. Cao, S. J. Pearton, G. Dang, A. P. Zhang, F. Ren, and J. M. Van Hove, Appl. Phys. Lett. **75**(26), 4130-2 (1999).
[146] Y. Koyama, T. Hashizume, and H. Hasegawa, Solid-State Electronics **43**(8), 1483-8 (1999).
[147] Ja-Soon Jang, Seong-Ju Park, and Tae-Yeon Seong, J. Vac. Sci. Technol. B **17**(6), 2667-70 (1999).
[148] Ching-Ting Lee, Y-J Lin, and Day-Shan Liu, Appl. Phys. Lett. **79**(16), 2573-5 (2001).
[149] M. Sawada, T. Sawada, Y. Yamagata, K. Imai, H. Kimura, M. Yoshino, K. Iizuka, and H. Tomozawa, J. of Cryst. Growth **189-190**, 706-10 (1998).
[150] T. Sawada, Y. Ito, K. Imai, K. Suzuki, H. Tomozawa, and S. Sakai, Appl. Surf. Sci. **159-160**, 449-55 (2000).
[151] T. Maeda, Y. Koide, and M. Murakami, Appl. Phys. Lett. **75**(26), 4145-7 (1999).
[152] S. Ootomo, T. Hashizume, and H. Hasegawa, Phys. Stat. Sol. A **188**(1), 371-4 (2001).

[153] K. H. Baik, B. Luo, J. Kim, S. J. Pearton, and F. Ren, Solid-State Electronics **46**(9), 1459-62 (2002).
[154] B. Luo, J. W. Johnson, F. Ren, K. W. Baik, S. J. Pearton, Solid-State Electronics **46**(5), 705-10 (2002).
[155] K. H. Baik, B. Luo, S. J. Pearton, and F. Ren, Solid-State Electronics **46**(6), 803-6 (2002).
[156] T. Hashizume, S. Ootomo, S. Oyama, M. Konishi, and H. Hasegawa, J. Vac. Sci. Technol. B **19**(4), 1675-81 (2001).
[157] G. L. Martinez, M. R. Curiel, B. J. Skromme, R. J. Molnar, J. Elec. Mat. **29**(3), 325-31 (2000).
[158] E. J. Miller, D. M. Schaadt, E. T. Yu, C. Poblenz, C. Elsass, and J. S. Speck, J. Appl. Phys. **91**(12), 9821-6 (2002).
[159] E. D. Readinger, B. P. Luther, S. E. Mohney, and E. L. Piner, J. Appl. Phys. **89**(12), 7983-7 (2001).
[160] M. J. Manfra, N. G. Weimann, J. W. P. Hsu, L. N. Pfeiffer, K. W. West, and S. N. G. Chu, Appl. Phys. Lett. **81**(8), 1456-8 (2002).
[161] J. W. P. Hsu, M. J. Manfra, R. J. Molnar, B. Heying, and J. S. Speck, Appl. Phys. Lett. **81**(1), 79-81 (2002).
[162] J. Spradlin, S. Dogan, M. Mikkelson, D. Huang, L. He, D. Johnstone, H. Morkoç, and R. J. Molnar, Appl. Phys. Lett. **82**(20), 3556-8 (2003).
[163] D. A. Stocker and E. F. Schubert, and J. M. Redwing, Appl. Phys. Lett. **73**(18), 2654-6 (1998).
[164] Dongsheng Li, M. Sumiya, S. Fuke, Deren Yang, Duanlin Que, Y. Suzuki and Y. Fukuda, J. Appl. Phys. **90**(8), 4219-23 (2001)
[165] G. Nowak, X. H. Xia, J. J. Kelly, J. L. Weyher, and S. Porowski, J. Cryst. Growth **222**(4), 735-40 (2001).
[166] K. A. Rickert, A. B. Ellis, F. J. Himpsel, J. Sun, and T. F. Kuech, Appl. Phys. Lett. **80**(2), 204-206 (2002).
[167] Reif, *Fundamentals of Statistical and Thermal Physics* (Mc Graw Hill, USA 1965).
[168] S. Elhamri, A. Saxler, W. C. Mitchel, R. Berney, C. Elsass, Y. Smorchkova, U. K. Mishra, J. S. Speck, U. Chowdhury, and R. D. Dupuis, J. Appl. Phys. **93**(2), 1079-1082 (2003).
[169] *Atlas User's Manual Vol. 1* SILVACO International (Santa Clara, CA, USA 2000).
[170] *Atlas User's Manual Vol. 2* SILVACO International (Santa Clara, CA, USA 2000).